Searches for Resonant and Non-resonant Higgs Boson Pair-production in the $b\bar{b}\tau^+\tau^-$ Decay Channel with 36.1 fb^{-1} PP Collision Data at $\sqrt{s} = 13$ TeV with the ATLAS Detector

by

Hao Liu

A dissertation submitted in partial fulfillment
of the requirements for the degree of
Doctor of Philosophy
(Physics)
in The University of Michigan
2019

Doctoral Committee:

Assistant Professor Thomas Schwarz, Chair
Associate Professor Christine Aidala
Assistant Professor Yang Chen
Professor James Liu
Professor Bing Zhou

Hao Liu

lhao@umich.edu

ORCID ID: 0000-0002-1456-8751

For all the days and nights in Ann Arbor and CERN

For my family, all my friends and people who helped me in my life

ACKNOWLEDGEMENTS

At the very beginning, I want to say that I feel really lucky to be in the ATLAS research group, in University of Michigan, Ann Arbor and to be a member of CERN, where I have met great people and made awesome friends. I am so honored to be a member of the ATLAS experiment, which is one of the greatest experiments humans have conducted in history. As a man who loves traveling, I am also very grateful for the opportunity to be able to go and stay at CERN, which is located in both France and Switzerland, thus I was able to see the natural beauty and various of cultures in Europe. Furthermore, I really appreciate all the years that I spent in Ann Arbor too. Ann Arbor is a small city with its unique beauty and quiet, where I met fabulous faculties as Professor Luming Duan, Professor Jianming Qian, Professor Gordon Kane and Professor Leonard Sander. They gave nice and useful lectures in class without which I would not be able to build the solid knowledge basis for my research.

I want to thank my advisor Thomas Schwarz firstly, who has always been supporting me all these years, both financially and mentally. Tom is the person who really opened the door of my research and guided me to the ATLAS experiment. His advice for research in academia, as well as for life can not be more useful for me. My future career will definitely benefit from the advice too. Thank you very much for always standing on my back fighting together with me whenever I have encountered obstacles on my research,as well as, the free academic ambience you have built all these years in our research group. Our research group is always full of joy because of your humor. Furthermore, I really appreciate the advice, support and confidence

you gave me when I was struggling on the job hunting, without which I might not be able to make the smooth transfer from academia to industry.

Secondly, I would like to thank Allison Deiana specially, who worked as a post-doc in Tom's research group, and now is a faculty member in Southern Methodist University. Allison was the one who gave me detailed guidance and hands on research experience with extraordinary patience when I first started doing research. I will never forget Allison's support at the beginning of my PhD journey.

Many thanks to my committee members as well, Bing Zhou, James Liu, Christine Aidala and Yang Chen. They have provided valuable advice, comments and suggestions which really helped to improve this work.

It's a great fortune to work within the awesome Michigan ATLAS research group. I have received numerous help and trainings from people in Michigan ATLAS group, Bing Zhou, Jianming Qian, Dante Amidei, Junjie Zhu, Homer Neal, Dan Levin, Tiesheng Dai and others. I want to give special thanks to Edward Diehl here, without whose help, I would not be able to accomplish the ATLAS qualification work. At the same time, my thanks go to all my colleagues and friends in the Michigan ATLAS group for the great collaborations and their help, Lulu Liu, Haolv Feng, Jiaming Yu, Tom Cheng, Nan Lu, Karishma Sekhon, Dan Marley, Zhaoxu Xi, Ismet Siral, Wen Guo, Wenhao Xu, Rongkun Wang, Zirui Wang, Yicheng Guo, Yanlin Liu, Yusheng Wu, Bing Li, Lailin Xu, Liang Guan, Cong Geng, Dongliang Zhang,Zhi Zheng, Aaron White, Rachel Hyneman, Garrett Merz, Xueye Hu, Jinhong Wang, Noah Zipper, etc. At the same time, I want to thank all the collaborators whom I have been working with happily and achieved excellent physics results together, Lei Zhang, Guillermo Hamity, Nicholas Rompotis, Pedro de Bruin, Lorenz Hauswald, Masahiro Morinaga, Carl Gwilliam, Katharine Leney, Thomas Stevenson, Agni Bet and Alessandra Betti.

For all these years in Ann Arbor, I have also met nice people and became best friends with them, I want to thank all my best fiends in Ann Arbor, Gong Cheng

and his wife Shuai Zhang, Wen Yu, Yike Liu, Leyou Zhang and Yina Geng. We have had countless delicious meals and numerous fun together, which really helps a lot to relieve the stress and anxiety on the journey towards PhD.

Finally, and perhaps most importantly, I want to thank my parents. They have given me selfless support all the time with love. It is impossible for me to come to a foreign country and pursue my PhD degree without their sacrifice and support.

This dissertation is dedicated to everyone who have helped me on this fantastic, exciting, beautiful journey towards the PhD degree. Now this journey has reached its end, a new great voyage is about to begin. Good luck and Forever Go Blue!

TABLE OF CONTENTS

LIST OF FIGURES

Figure

LIST OF TABLES

Table

ABSTRACT

A search for resonant and non-resonant Higgs boson pair-production decaying to a $bb\tau\tau$ final state is presented. The search uses 36.1 fb^{-1} of pp-collision data with $\sqrt{s} = 13\ TeV$ recorded by the ATLAS [1] experiment at the LHC [2] in 2015 and 2016. The semi-leptonic and fully hadronic di-tau final states are considered. No deviation from the Standard Model prediction is observed. Upper limits are placed on the resonant di-Higgs production cross-section times branching ratio for $bb\tau\tau$ final states. The results are interpreted in terms of constraints on a Randall-Sundrum Kaluza-Klein graviton model[3, 4, 5], and a 2HDM[6, 7] model in an extended Higgs sector. The $bb\tau\tau$ final state channel gives the best upper limit result among all ATLAS[1] and CMS[8] di-Higgs data analysis channels with it's fantastic machine learning techniques and newly added channels,as well as,extra triggers. The cross-section times branching ratio for non-resonant Higgs pair-production is constrained to be ~ 12.7 times of the Standard Model prediction, which is also the best sensitivity physicists have obtained among all experiment analysis channels.

CHAPTER I

Introduction

The discovery of the Standard Model Higgs on the ATLAS and CMS detector in the year of 2012 started new era for experimental particle physicists to explore the mechanism of electroweak symmetry breaking [9, 10]. Different experiments have studied the physical properties of the Standard Model Higgs and demonstrated that the observed boson is consistent with the theoretically predicted Higgs particle with a mass[11, 12, 13, 14, 15] around 125.09 GeV [16].

The Standard Model Higgs boson could be pair-produced by gluon fusion via the top quark loops on LHC, as well as, via the Higgs self-interaction, which is predicted in the Standard Model. Thus, studying of the Higgs trilinear self-interaction(λ_{hhh}) will be the final examination of the Higgs mechanisms corresponding to the electroweak symmetry breaking. In fact, the future particle accelerator High Luminosity LHC aims this as one of the primary goals too.

However, the top quark loop di-Higgs production mode and the self-interaction di-Higgs production mode have a negative interference between each other which leads to an extremely small total cross section, which is $\sim 33.41\ fb$ at 13 TeV center-of-mass energy [17, 18]. It is impossible for the LHC to produce enough luminosity for detecting the pair-production of Standard Model Higgs now, not to say to reach the sensitivity to be able to see the Higgs self-interaction which has an even smaller

cross section. However, it's still very meaningful to conduct a study on the pair-production(Non-Resonant) of the Standard Model Higgs using the recorded data on ATLAS now, as this study will give us a hint about the sensitivity we could reach right now and how much data we will need in the future on the High Luminosity LHC. More importantly, through the decomposition of the experimental errors, we will be able to know what we should do to improve the sensitivity in the future. The sensitivity we get in this experiment is the best sensitivity physicists have got now on the Standard Model Di-Higgs production. It shines great hope for the discovery of the Higgs pair-production and Higgs self-coupling on the next generation particle accelerator and detectors.

The Standard Model theory has achieved great success from the discovery of the Standard Model Higgs in year 2012 [9, 10]. However, nothing is perfect, so is the Standard Model theory. There are things that the Standard Model theory is unable to explain nowadays, among which, Gravity could be one of the biggest obstacle lying on the road. The Standard Model theory gives no single hint on the gravity force or graviton particles. Thus, physicists worked out different models beyond the Standard Model to include the graviton into the current theoretical framework. The Randall-Sundrum(RS) model [3, 4] is one of these models which introduces an extra dimension to include the gravitons. The model predicts the process that the RS graviton decays to two Standard Model Higgs. At the same time, there are also other models physicists proposed beyond the Standard Model to cover the shortages of the Standard Model. The Two Higgs Doublet Model(2HDM) [6, 7] is one of these by extending the Higgs field to two doublets fields. The 2HDM model predicts extra heavy CP even Higgs which could decay to two Standard Model Higgs too. The cross sections of the RS graviton decaying to Standard Model Higgs and heavy Higgs decaying to Standard Model Higgs could be significantly enhanced in their corresponding theories.

As trying to probe the Standard Model Higgs pair production is the primary goal

of this data analysis, using the same final states, we could easily accommodate the search for the 2HDM heavy Higgs and RS graviton into this analysis at the same time by simply modification of the signal Monte Carlo samples used in this analysis. Thus, we will conduct a search for the 2HDM heavy Higgs and RS gravitons using the same final state.

We choose the final state with one of the Standard Model Higgs decaying to two b quarks and one Higgs decaying to two τ leptons. The $bb\tau^+\tau^-$ channel has the third largest branching fraction(7.4%) among all the Di-Higgs decay channels with a relatively clean signature compared with the channels with larger branching fractions($bbbb$ and $bbWW$) [19]. This is the reason why we choose the $bb\tau\tau$ channel to do our study. We further split our study into two different sub-channels by the different decay modes of the two τs. If both of the τs decay to hadrons, we categorize the event into the $\tau_{\text{had}}\tau_{\text{had}}$ sub-channel. If one of the τ decays to leptons and the other one decays to hadrons, we categorize the event into the $\tau_\ell\tau_{\text{had}}$ sub-channel. The channel with both of the τs decaying into leptons are not considered due to its relatively small branching fraction. This channel might be considered in the next round of analysis to further improve the sensitivity tough. An extra trigger(lepton-τ trigger) is also added into the $\tau_\ell\tau_{\text{had}}$ channel to improve the statistics in low mass region.

The $\tau_\ell\tau_{\text{had}}$ channel alone was studied in 2012 using the $\sqrt{s} = 8TeV$ data from ATLAS detector on LHC, which is a cut-based data analysis(No machine learning techniques were applied) [20]. $\tau_{\text{had}}\tau_{\text{had}}$ channel and lepton-τ trigger are added this round with higher center-of-mass energy and more recorded particle collision data. The boosted decision tree(BDT)[21, 21] machine learning algorithm is also applied to replace the cut-based analysis strategy which improves our final result by about 50%. This is also the main reason that both our Resonant and Non-Resonant results beat all other di-Higgs final states analysis on ATLAS and CMS detectors.

CHAPTER II

The Standard Model and Beyond

2.1 The Standard Model of Particle Physics

The Standard Model of particle physics is the theory to describe three of the four known fundamental forces(the electromagnetic, weak, and strong forces, except gravitational force.) in the universe which was developed in stages throughout the later half of the 20th century. It also gives perfect explanation on how mass of matter generates via the Higgs Mechanism [11, 12, 13, 14, 15, 22]. The Standard Model contains 12 elementary spin half particles which are known as fermions, 4 gauge bosons and a Higgs boson. Each of the fermions has corresponding anti-particles. Based on different electric charge the fermions carry, the Standard Model clarifies them as six quarks and six leptons. Pairs from each classification are grouped together to form a generation with corresponding particles exhibiting similar physical behavior. Fig 2.1 gives a schematic drawing of the particles in Standard Model. Basic quantum numbers and categorizations of the particles are also showed in Fig 2.1.

The quarks carry color charge, thus they could interact through strong interaction and bound to form mesons(two quarks) and baryons(three quarks). Quarks also carry electric charge and weak iso-spin. Hence quarks could also interact with other fermions via electromagnetic and weak forces. The leptons carry no color charge and 3 of them carry no electric charge, which are called neutrinos. However, all of them carry

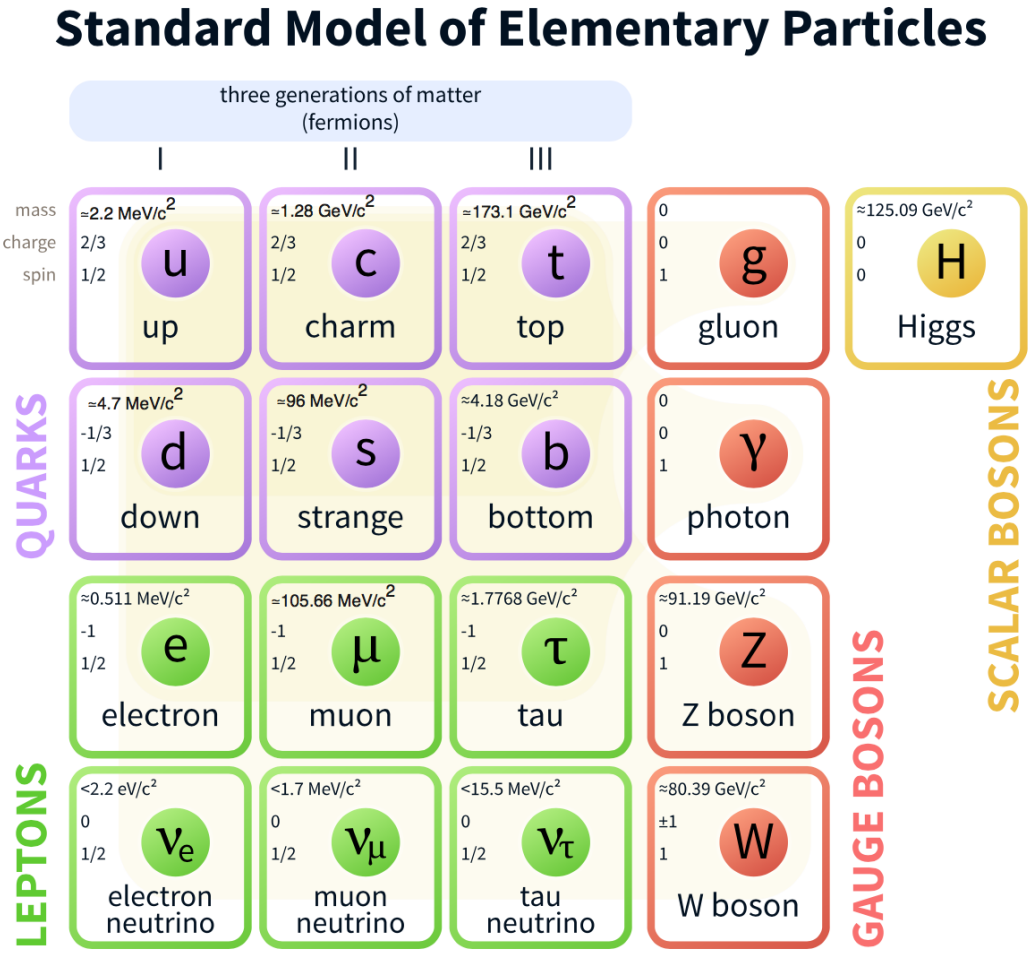

Figure 2.1: Standard Model Physics particle composition: 3 generations of fermions(quarks, leptons and neutrinos), gauge bosons and the Higgs boson

weak iso-spin. Thus, the 3 charged leptons could interact via both electromagnetic and weak interactions; neutrinos could only interact through weak interactions, which made them hard to detect. Particles in higher generations have higher mass and could generally decay to lower generation particles except for neutrinos.

Gauge bosons in Standard Model are the force carriers which mediate the strong, weak, and electromagnetic fundamental interactions. All of the gauge bosons have spin 1 which make them bosons. There are three electric charge neutral gauge bosons: gluons, photons, and Z bosons and 2 gauge bosons which carry electric charges: W^+ and W^-. Gluons have no masses. Eight gluons mediate the strong interactions between color charged particles. The eight gluons are labeled with combination of color and anti-color charge. Gluons could interact among themselves with the effective color charge they carry. The gluons and their interactions are described using the quantum chromodynamics(QCD). Photons are the electromagnetic force mediators. They are massless and carry no electric charges. The interactions between charged particles and photons are described in the theory of quantum electrodynamics(QED). Since photons carry no electric charge, they can't interact with themselves. The Z, W^+ and W^- are the gauge bosons mediating the weak interactions between particles with different flavors. The Z, W^+ and W^- are massive with Z boson having more mass than the W bosons. The Z bosons carry no electric charges and interacts with both left-handed particles and anti-particles. The $W^\pm$ bosons carry electric charge of +1 or -1 and interact with left-handed particles and right-handed antiparticles. The Z, $W^\pm$ bosons and photons are grouped together in the electroweak unification theory to mediate the electroweak interactions.

The Higgs boson was first proposed by Peter Higgs in 1964 [12]. It has no intrinsic spin and electric charge. The Higgs boson is very important to the Standard Model because all the elementary particles except photons and gluons get mass from interactions with Higgs bosons. The existence of Higgs boson also explains the difference

between electromagnetism and weak force. The Higgs boson is massive, so it must interact with itself. This is one very important property of the Higgs bosons. As Higgs boson was discovered at LHC in 2012,[9, 10] observing its self-coupling will be a very critical bench mark to justify its property. Fig 2.2 describes the categorization of the Standard Model elementary particles and the interactions between them, including self interaction between some particle themselves.

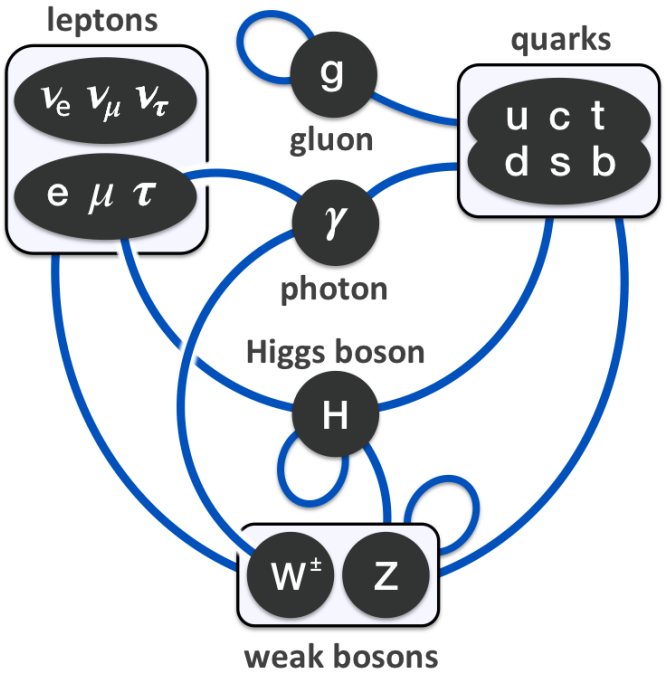

Figure 2.2: Standard Model Physics particle Interactions, blue lines link the particles which could couple

2.2 Higgs Mechanisms in Standard Model

The form of Lagrangian of a certain system determines the physics discipline and law it follows. The Standard Model Lagrangian of particle physics contains terms accounting for the different particle fields and their interactions, which is defined below in the equation (Neutrino mass terms are included. We assume the existence of the right handed neutrinos thus neutrinos are able to gain masses. Results from recent

neutrino oscillation experiments showed that the neutrinos have non-zero masses. Thus we use this assumption here) [23]:

$$\mathcal{L} = -\frac{1}{4}B_{\mu\nu}B^{\mu\nu} - \frac{1}{8}tr(\mathbf{W}_{\mu\nu}\mathbf{W}^{\mu\nu}) - \frac{1}{2}tr(\mathbf{G}_{\mu\nu}\mathbf{G}^{\mu\nu}) \quad \textbf{(U(1),SU(2) and SU(3) gauge terms)}$$

$$+ (\bar{\nu}_L, \bar{e}_L)\bar{\sigma}^\mu iD_\mu \begin{pmatrix}\nu_L \\ e_L\end{pmatrix} + \bar{e}_R\sigma^\mu iD_\mu e_R + \bar{\nu}_R\sigma^\mu iD_\mu \nu_R + (h.c.) \quad \textbf{(lepton dynamical terms)}$$

$$- \frac{\sqrt{2}}{v}\left[(\bar{\nu}_L, \bar{e}_L)\phi M^e e_R + \bar{e}_R\bar{M}^e\bar{\phi}\begin{pmatrix}\nu_L \\ e_L\end{pmatrix}\right] \quad \textbf{(electron, muon,tau mass terms)}$$

$$- \frac{\sqrt{2}}{v}\left[(-\bar{e}_L, \bar{\nu}_L)\phi^* M^\nu \nu_R + \bar{\nu}_R\bar{M}^\nu\phi^T\begin{pmatrix}-e_L \\ \nu_L\end{pmatrix}\right] \quad \textbf{(neutrino mass terms)}$$

$$+ (\bar{u}_L, \bar{d}_L)\bar{\sigma}^\mu iD_\mu \begin{pmatrix}u_L \\ d_L\end{pmatrix} + \bar{u}_R\sigma^\mu iD_\mu u_R + \bar{d}_R\sigma^\mu iD_\mu d_R + (h.c.) \quad \textbf{(quark dynamical terms)}$$

$$- \frac{\sqrt{2}}{v}\left[(\bar{u}_L, \bar{d}_L)\phi M^d d_R + \bar{d}_R\bar{M}^d\bar{\phi}\begin{pmatrix}u_L \\ d_L\end{pmatrix}\right] \quad \textbf{(down, strange, bottom mass terms)}$$

$$- \frac{\sqrt{2}}{v}\left[(-\bar{d}_L, \bar{u}_L)\phi^* M^u u_R + \bar{u}_R\bar{M}^u\phi^T\begin{pmatrix}-d_L \\ u_L\end{pmatrix}\right] \quad \textbf{(up,charmed, top mass terms)}$$

$$+ \overline{(D_\mu\phi)}D^\mu\phi - m_h^2\left[\bar{\phi}\phi - v^2/2\right]^2/2v^2 \quad \textbf{(Higgs dynamical and mass terms)}$$

The mathematics of the Standard Model is described by a gauge quantum field theory containing the internal symmetries of the unitary product group $SU(3)_C \times SU(2)_L \times U(1)_Y$. Left-handed fermions are known to be doublets under $SU(2)_L$:

$$leptons : \begin{pmatrix}\nu_L \\ e_L\end{pmatrix}; \qquad quarks : \begin{pmatrix}u_L \\ d_L\end{pmatrix} \tag{2.1}$$

The right-handed fermions are all singlets under $SU(2)_L$:

$$leptons : e_R, \nu_R; \qquad quarks : u_R, d_R \tag{2.2}$$

All these fermions have implicit 3-component generation indices:

$$e_i = (e, \mu, \tau), \nu_i = (\nu_e, \nu_\mu, \nu_\tau), u_i = (u, c, t), d_i = (d, s, b) \tag{2.3}$$

ϕ is a 2-component complex Higgs field. B_μ, $\mathbf{W}_\mu$ and $\mathbf{G}_\mu$ are the gauge boson vector potentials. $\mathbf{W}_\mu$ are made of 2×2 traceless Hermitian matrices and $\mathbf{G}_\mu$ are composed of 3×3 traceless Hermitian matrices. Associated field tensors are defined as below:

$$B_{\mu\nu} = \partial_\mu B_\nu - \partial_\nu B_\mu \tag{2.4}$$

$$\mathbf{W}_{\mu\nu} = \partial_\mu \mathbf{W}_\nu - \partial_\nu \mathbf{W}_\mu + ig_2(\mathbf{W}_\mu \mathbf{W}_\nu - \mathbf{W}_\nu \mathbf{W}_\mu)/2 \tag{2.5}$$

$$\mathbf{G}_{\mu\nu} = \partial_\mu \mathbf{G}_\nu - \partial_\nu \mathbf{G}_\mu + ig(\mathbf{G}_\mu \mathbf{G}_\nu - \mathbf{G}_\nu \mathbf{G}_\mu) \tag{2.6}$$

The covariant derivatives acting on these fermion fields and the complex Higgs field are then defined as below:

$$D_\mu \begin{pmatrix} \nu_L \\ e_L \end{pmatrix} = [\partial_\mu - \frac{ig_1}{2} + \frac{ig_2}{2}\mathbf{W}_\mu] \begin{pmatrix} \nu_L \\ e_L \end{pmatrix} \tag{2.7}$$

$$D_\mu \begin{pmatrix} u_L \\ d_L \end{pmatrix} = [\partial_\mu + \frac{ig_1}{6}B_\mu + \frac{ig_2}{2}\mathbf{W}_\mu + ig\mathbf{G}_\mu] \begin{pmatrix} u_L \\ d_L \end{pmatrix} \tag{2.8}$$

$$D_\mu e_R = [\partial_\mu - ig_1 B_\mu] e_R \tag{2.9}$$

$$D_\mu \nu_R = \partial_\mu \nu_R \tag{2.10}$$

$$D_\mu u_R = [\partial_\mu + \frac{i2g_1}{3}B_\mu + ig\mathbf{G}_\mu] u_R \tag{2.11}$$

$$D_\mu d_R = [\partial_\mu - \frac{ig_1}{3}B_\mu + ig\mathbf{G}_\mu] d_R \tag{2.12}$$

$$D_\mu \phi = [\partial_\mu + \frac{ig_1}{2}B_\mu + \frac{ig_2}{2}\mathbf{W}_\mu]\phi \tag{2.13}$$

The $W^{\pm}$ bosons are combinations of the $\mathbf{W}_{\mu}$ vector potential:

$$W_{\mu}^{+} = W_{\mu}^{-*} = W_{12\mu}/\sqrt{2} \tag{2.14}$$

The vector bosons B_{μ} and $W_{11\mu}$ are both electrically neutral. The spontaneous symmetry breaking makes them mix. The mass eigenstates are instead of a orthogonal linear combinations of these two gauge eigenstate fields, which are the well known photon field A^{μ} and the massive Z boson vector field Z_{μ}.

$$\begin{pmatrix} Z_{\mu} \\ A_{\mu} \end{pmatrix} = \begin{pmatrix} cos\theta_W & -sin\theta_W \\ sin\theta_W & cos\theta_W \end{pmatrix} \begin{pmatrix} W_{11\mu} \\ B_{\mu} \end{pmatrix} \tag{2.15}$$

By comparing with the QED, we could know that:

$$g_1 \cos\theta_W = e \tag{2.16}$$

$$\tan\theta_W = \frac{g_1}{g_2} \tag{2.17}$$

The result from experiment gives the value of $sin\theta_W$ as:

$$\sin^2\theta_W = 0.2315 \tag{2.18}$$

Since $\mathcal{L}$ is a $SU(2)_L$ gauge invariant, a gauge can be chosen to make the ϕ having form in terms of its deviation from the vacuum expectation value:

$$\phi^T = (0, v + h)/\sqrt{2} \tag{2.19}$$

with the expectation value of ϕ to be equal to:

$$\langle\phi\rangle_0^T = (0, v)/\sqrt{2}; \tag{2.20}$$

where v is vacuum expectation value(VEV) of the Higgs field which minimized the Lagrangian of the Higgs field:

$$\mathcal{L} = \overline{(D_\mu \phi)} D^\mu \phi - m_h^2 [\bar{\phi}\phi - v^2/2]^2 / 2v^2 \tag{2.21}$$

where h is a residual Higgs field. If we plug in B_μ and $\mathbf{W}_\mu$ into the Higgs Kinetic term in terms of A_μ, Z_μ and $\mathbf{W}_\mu$, with Higgs field written in form of Eq. 2.19, we could get the result:

$$\mathcal{L}_{\phi\, kinetic} = \overline{(D_\mu \phi)} D^\mu \phi = \frac{1}{2}\partial_\mu h \partial^\mu h + \frac{(v+h)^2}{4}[g_2 \mathbf{W}_\mu^+ \mathbf{W}^{-\mu} + \frac{1}{2}(g_1^2 + g_2^2) Z_\mu Z^\mu] \tag{2.22}$$

Evidently, there is no A_μ term explicitly in the equation. So photons A_μ have zero mass, in agreement with the fact that $U(1)_{EM}$ gauge invariance remains unbroken. The prediction of the masses of the gauge bosons comes from the mass terms in the kinetic term in Eq. 2.22. It's straight forward to get the $W^\pm$ and Z boson masses as shown in Eq. 2.23 and Eq. 2.24. There are other terms involved $\mathbf{W}_\mu^\pm$, Z_μ and h in Eq. 2.22. They are considered as the coupling between the gauge boson field and Higgs field:

$$m_W^2 = \frac{g_2^2 v^2}{4} \tag{2.23}$$

$$m_Z^2 = \frac{(g_1^2 + g_2^2) v^2}{4} \tag{2.24}$$

Combining Eq. 2.23, Eq. 2.24 and the weak mixing angel Eq. 2.17, we could get the relation between the $W^\pm$ and Z boson masses:

$$\frac{m_W}{m_Z} = \cos\theta_W \tag{2.25}$$

By now, the masses of the gauge bosons(photons, Z and $W^\pm$ bosons) have all been generated by their interactions with the complex doublet Higgs field. Looking at the

Higgs dynamics and mass term in the Standard Model Lagrangian, similarly if we do the expansion around the VEV using Eq. 2.19 for the Higgs potential part. We could easily get the potential of Higgs boson $V(h)$:

$$V(h) = \frac{m_h^2}{2}h^2 + \frac{m_h^2}{2v}h^3 + \frac{m_h^2}{8v^2}h^4 \tag{2.26}$$

The first term in Eq. 2.26 apparently gives the rise of the Standard Model Higgs with mass m_h. The second and third terms are about h^3 and h^4 which means Standard Model Higgs boson should be able to couple with itself with a vertex of 3 or 4 tracks as shown in Fig. 2.3:

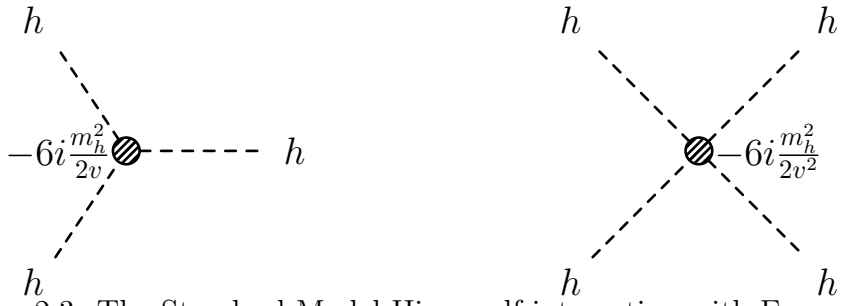

Figure 2.3: The Standard Model Higgs self-interaction with Feynman rules

This implies the very important and critical property of the Standard Model Higgs about self-coupling. It is also this property that inspires the idea to search for the Non-resonant Standard Model Higgs self-coupling in this data analysis to fully test Higgs Mechanism. Looking at the coefficients before these two Higgs self coupling terms, they are very small , meaning that the Standard Model Higgs self-interactions are really weak, which makes them extremely hard to detect.

The Non-resonant Standard Model Di-Higgs production not only contains the Higgs self-coupling contribution, as shown in the Fig. 2.4, but also has the contribution from the gluon fusion quark loop processes with the Standard Model Higgs coupling to quarks as shown in Fig. 2.5:

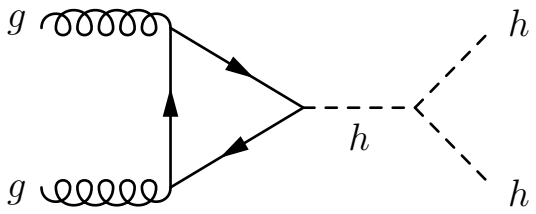

Figure 2.4: gluon fusion Non-Resonant Standard Model Di-Higgs production through off-shell Higgs self-coupling

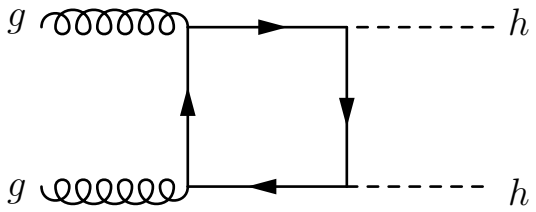

Figure 2.5: gluon fusion Non-Resonant Standard Model Di-Higgs production with quark loop

Theoretical prediction gives the cross section of these two processes combined to be $\sim 33 fb$ at 13 TeV center of mass energy [17, 18], with strongly negative interference between the two diagrams [24] shown in Fig. 2.4 and 2.5. Pursuing the measurement of the pure Standard Model Higgs self-coupling cross section is not the goal of this analysis as it's been shown that it is too small for the LHC to measure. Instead, we will only try to probe the total cross section of Standard Model Higgs self-coupling process combined with the quark loop Di-Higgs processes in the gluon fusion production mode.

The masses of the fermions are from the fermion mass terms in the Standard Model Lagrangian. The fermion masses are the singular values of the 3×3 fermion mass matrices M^{ν}, M^{e}, M^{u}, M^{d}:

$$M^{e} = \mathbf{U}_{L}^{e\dagger} \begin{pmatrix} m_e & 0 & 0 \\ 0 & m_\mu & 0 \\ 0 & 0 & m_\tau \end{pmatrix} \mathbf{U}_{R}^{e} \tag{2.27}$$

$$M^{\nu} = \mathbf{U}_L^{\nu\dagger} \begin{pmatrix} m_{\nu_e} & 0 & 0 \\ 0 & m_{\nu_\mu} & 0 \\ 0 & 0 & m_{\nu_\tau} \end{pmatrix} \mathbf{U}_R^{\nu} \tag{2.28}$$

$$M^{u} = \mathbf{U}_L^{u\dagger} \begin{pmatrix} m_{u} & 0 & 0 \\ 0 & m_{c} & 0 \\ 0 & 0 & m_{t} \end{pmatrix} \mathbf{U}_R^{u} \tag{2.29}$$

$$M^{d} = \mathbf{U}_L^{d\dagger} \begin{pmatrix} m_{d} & 0 & 0 \\ 0 & m_{s} & 0 \\ 0 & 0 & m_{b} \end{pmatrix} \mathbf{U}_R^{d} \tag{2.30}$$

All the **U**s are 3×3 unitary matrices($\mathbf{U}^{-1} = \mathbf{U}^{\dagger}$). The **Mass Diagonalization Theorem** tells us that the mass eigenstates with definite mass are actually the linear combinations of the gauge eigenstates in $\mathcal{L}$. The mass eigenstates and the gauge eigenstates covert between each others with the unitary matrices as in Eq. 2.31 and Eq. 2.32 , the particles with prime are the mass eigenstates particles.

$$e'_L = \mathbf{U}_L^e e_L, \quad e'_R = \mathbf{U}_R^e e_R, \quad \nu'_L = \mathbf{U}_L^{\nu} \nu_L, \quad \nu'_R = \mathbf{U}_R^{\nu} \nu_R \tag{2.31}$$

$$u'_L = \mathbf{U}_L^u u_L, \quad u'_R = \mathbf{U}_R^u u_R, \quad d'_L = \mathbf{U}_L^d d_L, \quad d'_R = \mathbf{U}_R^d d_R \tag{2.32}$$

If we reform the $\mathcal{L}$ with redefinition of the mass eigenstates of the particles, the unitary matrices **U**s fall out for all fermion mass terms in the Lagrangian. The form of the $\mathcal{L}$ is identical as in the gauge eigenstates basis. However, in the lepton and quark dynamics terms, there will be **U**s left in $\bar{u}'_L \mathbf{U}_L^u \widetilde{\sigma}^u W_\mu^{\pm} \mathbf{U}_L^{d\dagger} d'_L$ and $\bar{\nu}'_L \mathbf{U}_L^{\nu} \widetilde{\sigma}^{\nu} W_\mu^{\pm} \mathbf{U}_L^{e\dagger} e'_L$. Here we encountered a consequence of going to the mass eigenstate basis from the gauge eigenstate basis. The charged-current weak interactions contains non-trivial

matrices when acting on the quark and lepton families. For quarks, we define:

$$\mathbf{V}^q = \mathbf{U}_L^u \mathbf{U}_L^{d\dagger} \tag{2.33}$$

which is called the Cabibbo-Kabayashi-Maskawa(CKM) matrix [25, 26]. and for leptons, we define:

$$\mathbf{V}^l = \mathbf{U}_L^\nu \mathbf{U}_L^{e\dagger} \tag{2.34}$$

which is called the Pontecorvo-Maki-Nakagawa-Sakata matrix [27]. These two matrices count for important physical effect in particle physics. The phase included in the CKM matrix is the only reason accounting for the CP violation in the Standard Model and the neutrino oscillations are due to the fact that Pontecorvo-Maki-Nakagawa-Sakata matrix is not an identity matrix.

2.3 Beyond The Standard Model

The Standard Model of particle physics has demonstrated huge success for explaining experimental result. Also, the theory is believed to be theoretically self-consistent. Furthermore, the discovery of the Higgs boson in 2012 [9, 10] has added further credence to the Standard Model theory. The Standard Model itself seems to have the simplicity, clearness and natural beauty that a physics theory should have. However, the Standard Model contains at least 19 arbitrary parameters, which, is a little bit too much if we still believe that a perfect physics theory needs to be as simple as possible. A hundred years ago, Lord Kelvin, who thought that the physics theory at that time was well established and almost completed, said: **The beauty and clearness of the dynamical theory, which asserts heat and light to be modes of motion, is at present obscured by two clouds.** [28] Ironically, it turned out later on that the modern physics theories are built right on these two clouds as the fundamental basis. Although the Standard Model has been examined and proved to be right by

numerous physics experiments, there are still "clouds obscuring at present". The Standard Model is not perfect and fails to give explanations to some of the physics phenomena nowadays. Understanding these phenomena could possibly open a door to new physics or even set new foundation for the fundamental physics theory just like people did after understanding the "two clouds" in the 20th century. Unlike Lord Kelvin's "two clouds", the physics phenomena which Standard Model fails to explain are considered to be very critical and fundamental for modern physics, such as:

- **Gravity**: The Standard Model is unable to explain the gravity. The graviton can not be simply added to the Standard Model Lagrangian and works without modifications. On the other hand, the Standard Model is incompatible with general relativity, which has been examined by numerous experiments to be the most successful theory for describing the gravity so far.

- **Hierarchy problem**: The Standard Model Higgs mass is around the GeV scale and quadratically sensitive to any mass scale of new physics. If new physics appears at large mass scale, the Higgs mass will have non-physical correction beyond tree level. Another way to say this problem in a plain and easy way is that the gravity is too small compared with the weak interaction in Standard Model.

- **Dark Matter and Dark Energy**: It's been proved by several astronomy observations that the dark matter and energy exist and account for about 95% of the total energy in the universe, whereas the Standard Model is only able to explain the rest 5% and unable to supply any fundamental dark matter or dark energy candidates.

- **Matter-antimatter asymmetry**: The Standard Model predicts almost equal amounts of matter and antimatter under the condition that the initial condition

of the universe does not involve any imbalance. However, in the observable universe, significantly more matter is observed than the antimatter. The Standard Model fails to explain this asymmetry.

All these failures of the Standard Model, plus the desire of physicists to find the grand unified theory which forms a group theory for unifying all elementary interactions, drive physicists explore theories beyond the Standard Model. There are quite many candidate theories. Among which ,the Two-Higgs-Doublets Model and the Bulk Randall-Sundrum Graviton theory will be briefly described as they are the ones being explored and searched in this data analysis.

2.3.1 Two-Higgs-Doublets Model

In the Standard Model, physicists assume a single SU(2) doublet as the Higgs field, which is the simplest possible scalar structure. It's natural to come up with the extension of the Standard Model by adding an extra doublet, which is one of the simplest possible extensions of the Standard Model. It's called the two-Higgs-doublet-model(2HDM) [6, 7]. There are multiple motivations driving physicists to come up with the idea of the 2HDM. The best known one is super-symmetry theory [29]. The Minimal Supersymmetric Standard Model(MSSM)[30, 31] requires two Higgs doublets to be presented in order to give masses to all the particles in such theory. Trying to explain the baryon asymmetry in the universe, which the Standard Model is unable to explain, is another important motivation of 2HDM. The flexibility of the scalar mass spectrum and additional sources of CP violation in the 2HDM could help explain the baryon asymmetry in the universe.

The most general scalar potential for two doublets Φ_1 and Φ_2 is shown in Eq. 2.35

where all the parameters are real:

$$\begin{aligned} V = & m_{11}^2 \Phi_1^\dagger \Phi_1 + m_{22}^2 \Phi_2^\dagger \Phi_2 - m_{12}^2 (\Phi_1^\dagger \Phi_2 + \Phi_2^\dagger \Phi_1) + \frac{\lambda_1}{2} (\Phi_1^\dagger \Phi_1)^2 + \frac{\lambda_2}{2} (\Phi_2^\dagger \Phi_2)^2 \\ & + \lambda_3 \Phi_1^\dagger \Phi_1 \Phi_2^\dagger \Phi_2 + \lambda_4 \Phi_1^\dagger \Phi_2 \Phi_2^\dagger \Phi_1 + \frac{\lambda_5}{2} [(\Phi_1^\dagger \Phi_2)^2 + (\Phi_2^\dagger \Phi_1)^2] \end{aligned} \tag{2.35}$$

Similar to the Standard Model Higgs doublet, the minimal potential of the two Higgs doublets are in the form of Eq. 2.36 :

$$\langle \Phi_1 \rangle_0 = \begin{pmatrix} 0 \\ v_1/\sqrt{2} \end{pmatrix}, \qquad \langle \Phi_2 \rangle_0 = \begin{pmatrix} 0 \\ v_2/\sqrt{2} \end{pmatrix} \tag{2.36}$$

with vacuum expectation values(VEV) of the two neutral scalar fields equal to:

$$\langle \Phi_1^0 \rangle = v_1/\sqrt{2}, \qquad \langle \Phi_2^0 \rangle = v_2/\sqrt{2} \tag{2.37}$$

To be consistent with the Standard Model VEV, v_1 and v_2 must have the relation:

$$v \equiv \sqrt{(v_1^2 + v_2^2)} \equiv 246 GeV \tag{2.38}$$

The number of degrees of freedom associated with the two complex complex scalar SU(2) doublets is 8. Three of them are used to generate the mass of $W^\pm$ and Z^0 gauge bosons. The remaining five degrees of freedom become five scalar particles: two neutral scalars(h and H), a pseudo-scalar(A) and two charged scalars($H^\pm$).

If we expand the 2HDM potential Eq. 2.35 around the minimal potential of the two Higgs doublets just like what is done in the Standard Model situation, as shown in Eq. 2.39.

$$\Phi_a = \begin{pmatrix} \phi_a^+ \\ (v_a + \rho_a + i\eta_a)/\sqrt{2} \end{pmatrix}, \qquad a = 1, 2 \tag{2.39}$$

With the two minimum conditions in Eq. 2.40:

$$\left.\frac{\partial V}{\partial \Phi_1^\dagger}\right|_{\langle\Phi_1\rangle,\langle\Phi_2\rangle} = 0, \qquad \left.\frac{\partial V}{\partial \Phi_2^\dagger}\right|_{\langle\Phi_1\rangle,\langle\Phi_2\rangle} = 0 \tag{2.40}$$

the original parameter m_{11} and m_{22} could be replaced with the other six free parameters in the 2HDM potential in Eq. 2.35. Similar to how it's done in the Standard Model to get the Higgs mass. With the diagonalization of the mass-squared matrices in order to get the mass eigenstate physical particles, the mass of the four physical Higgs masses(m_h, m_H, m_A, $m_{H^\pm}$) are achieved, as well as the two angles α and β in the unitary matrices for diagonalization. $\tan\beta$, the ratio between the VEVs of the two Higgs doublets is the most important parameters in studies of 2HDM:

$$\tan\beta \equiv \frac{v_2}{v_1} \tag{2.41}$$

while α is the neutral CP-even Higgs mixing angle. α and β together are very crucial to 2HDM because they determine the interactions between the 2HDM Higgs and other particles. In this data analysis, we will try to search the CP-even Heavy Higgs H in the 2HDM through the di-Higgs final state channels. Only the gluon fusion production mode of the 2HDM H is considered as shown in Fig. 2.6:

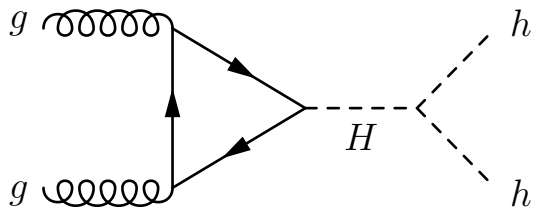

Figure 2.6: gluon gluon fusion production of the CP-Even Heavy Higgs in 2HDM

2.3.2 Bulk Randall-Sundrum Graviton

As it is pointed out in previous section, the Standard Model has the Planck-Weak Hierarchy problem, e.g. the weak scale is significantly smaller than the Planck scale which lead to the consequence that the Higgs mass is quadratically sensitive to any mass scale of new physics. The Randall Sundrum (RS) model [3, 4, 5] gives a way to solve the hierarchy problem in the Standard Model by imposing an extra warped dimension. The Randall-Sundrum theory proposed a non-factorizable metric as in Eq. 2.42 [5], which is able to explain the hierarchy problem in Standard Model. The $e^{-2kr_c\phi}$ is the warp factor which will transfer the five-dimension mass parameters into the four dimensional mass scales. It's worth noticing that this exponential factor changes rapidly in terms of r_c, which represents the radius of the curvature of the extra warped dimension. In other plain words, r_c defined the proper size of this extra warped dimension. Thus, a large hierarchy does not require extremely large r_c. ϕ could be regarded as the coordinate on this extra dimension. k is an energy scale constant in the order of the Planck brane energy.

$$ds^2 = e^{-2kr_c\phi}\eta_{\mu\nu}dx^\mu dx^\nu + r_c^2 d\phi^2 \tag{2.42}$$

Fig. 2.7 is a illustration of the universe in the Randall-Sundrum model. In Fig. 2.7, two planes are presented which are called branes. The brane on the left in orange color is called the "Planck brane", whereas the one on the right is called the TeV brane or weak brane. The universe we live in is on the weak brane while on the Planck brane, all the forces get unified. The two 3+1 dimensional branes get separated by the extra warped bulk. The bulk Randall-Sundrum model is an extension of the original Randall-Sundrum model by allowing the Standard Model fields to propagate not only on the TeV brane but also on the extra warped bulk, with only the Higgs fields restricted on the TeV brane. In the simplest of principles, we would expect

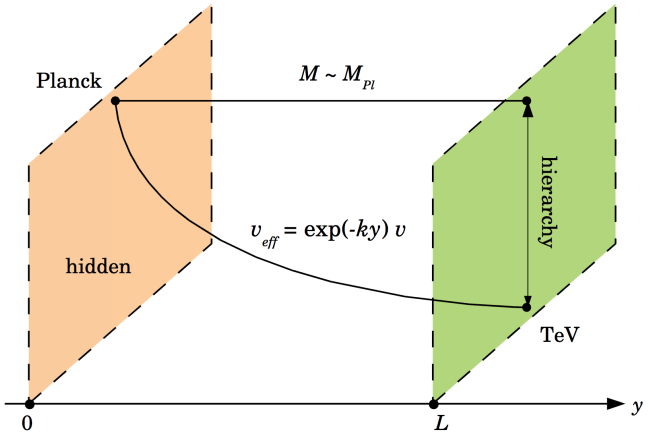

Figure 2.7: The Planck brane and weak brane are separated by a warped extra dimension in the bulk Randall-Sundrum model, the exponential factor causes great hierarchy as shown.

the excited states(Kaluza-Klein modes [32, 33]) of the Standard Model particles to exist in form of standing wave in the extra warped dimension with the invariant mass of the standing waves to be as in Eq. 2.43, with n being an integer, h being the Planck constant and c being the speed of light. We call this set of mass values the Kaluza-Klein tower:

$$M_n = \frac{nh}{r_c} \tag{2.43}$$

In principle, if the Standard Model survives in the bulk, the possible excited states of the gauge bosons in Standard Model would be discovered most likely. However, even with discovering these gauge bosons in the bulk is not sufficient to determine the underlying nature of the bulk Randall Sundrum framework. While, A good candidate to demonstrate the Randall-Sundrum model is the Kaluza-Klein Graviton(G_{KK}) with spin value 2 which is the gravitational field excitation states in the bulk.

In the original paper of Randall-Sundrum theory [5], it already gave the conclusion that the Kaluza-Klein modes of particles will be accessible at the LHC. The Kaluza-Klein Gravitons are localized near the TeV brane with coupling most strongly to Standard Model Higgs boson, top quarks and other Kaluza-Klein modes. This property of the G_{KK} determined that the di-Higgs final state channels will be prospecting

for its possible discovery. This is also the reason why, On the LHC, the dominant producing channel of G_{KK} would be the gluon fusion process with top quark loop. Thus, we would only consider the gluon-fusion production process in this data analysis a shown in Fig. 2.8.

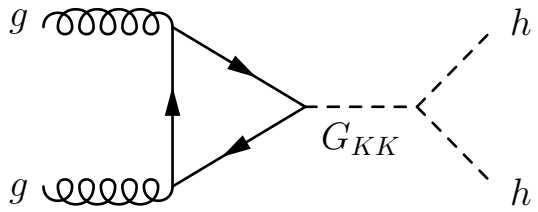

Figure 2.8: gluon gluon fusion production of the Kaluza Klein G_{KK}

CHAPTER III

ATLAS Detector at LHC

3.1 Overview of Large Hadron Collider(LHC)

The Large Hadron Collider(LHC) [2, 34, 35, 36] is the world's largest and most powerful particle accelerator. The aim of the LHC is to become a tool for physicists to test the predictions of different particle physics theories and hunt for a lot of new particles predicted by super-symmetric theories. The discovery of Higgs boson is considered as one of the biggest achievement on the LHC.

The LHC is underground inside a 27 km tunnel which is located at the border between France and Switzerland around Geneva area. Inside the tunnel, it's a ring consisting about 10000 superconducting magnets with accelerating structure to boost the energy of the particles. The superconducting magnets ring guides two different high-energy beams which travel in the opposite direction in the ring with its strong magnetic field. In order to get magnetic field strong enough, most parts of the accelerator is connected to the distribution system of liquid helium, especially the superconducting magnets, to cool down. The temperature in the ring could be as low as -271.3 °C, which is very close to absolute zero degree.

The LHC had its first run started on 10th, Sept, 2008. While the first operational run started from year 2009 to 2013 with beams' center of mass energy around 7 TeV. After this first operational run, which is called Run I, the LHC was shut down from

year 2013 to 2015 for system upgrades aiming collisions at 14 TeV. On 5th, April 2015, the LHC restarted after the 2 years long break. The center of mass collision energy had reached 13 TeV after the upgrades, which is called Run II. During Run II, not only the combined energy increased, the luminosity of the proton-proton collisions has been increased to 40% above the design value.

The LHC primarily collides proton beams, while it also collides beams of lead nuclei. There are four crossing points on the LHC ring where the two opposite beams get collided. Seven different detectors designed for different research purposes are placed around these crossing points. The four major ones are ATLAS [1], CMS [8], ALICE [37] and LHCb [38]. Among them, ATLAS [1] and CMS [8] are the two general purpose detectors. ALICE [37] is for the purpose of studying quark-gluon plasma which existed shortly after the Big Bang. LHCb [38] has another different purpose of research which is to mainly investigate anti-matter. The data analysis described in this article uses the data recorded by the ATLAS detector.

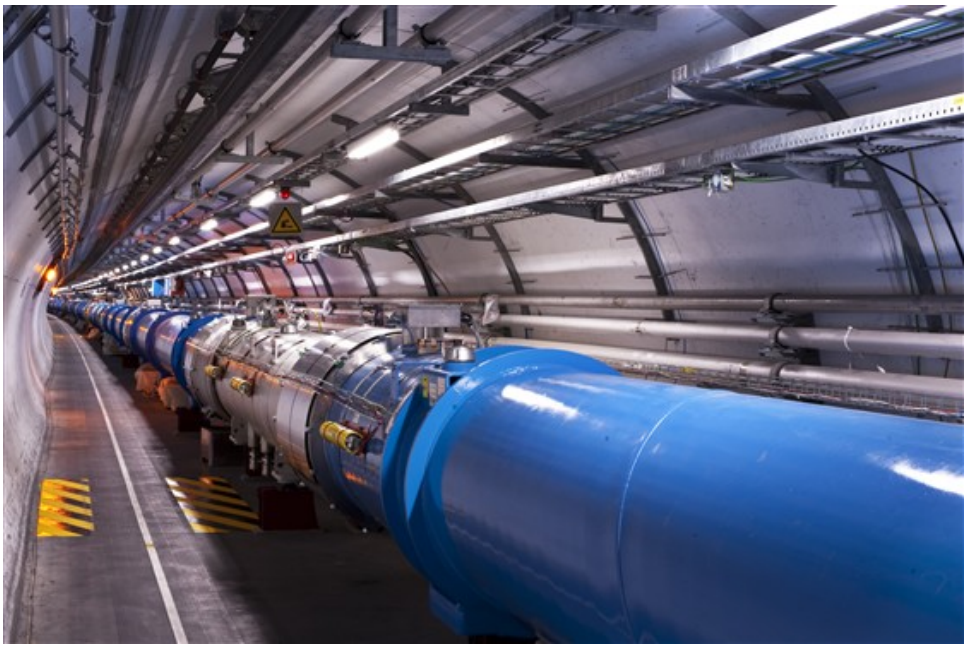

Figure 3.1: Under the tunnel, A section of the LHC, blue ring is the superconducting magnet ring

3.2 Overview of ATLAS Detector

There are two general purpose detectors on LHC: ATLAS(A Toroidal LHC ApparatuS) [1] and CMS(Compact Muon Solenoid) [8]. The very high energy and luminosity have set very strict standards for the design of these two particle detectors. ATLAS detector consists several different sub-detector with different functions.

The ATLAS detector is about 25 meters in height and 44 meters in length which is symmetric on beam direction with respect to the interaction point [1]. The choice of placement of the superconducting magnets has determined the designs of other ATLAS sub-systems. The superconducting magnets are placed in two ways on ATLAS [39]:

- A thin superconducting solenoid surrounding the inner-detector cavity.
- Three large superconducting toroids(1 barrel and 2 end-caps) positioned with an eight-fold azimuthal symmetry around the calorimeters.

The magnetic field produced by the superconducting magnets is able to immerse the inner detector [40] of ATLAS(2 T solenoidal field). The responsibility of the inner detector is recognizing pattern, measuring momentum and vertex and identifying electrons with the discrete high-resolution semiconductor pixel [41] and the strip detector in the inner part of the tracking volume. The straw-tube tracking detector of the inner detector is designed to be able to generate and detect transition radiation [42].

Outside the inner detector is the high granularity liquid-argon(LAr) electromagnetic sampling calorimeters [43] which cover the pseudorapidity range $|\eta| < 3.2$ with good energy and position resolution. The hadronic calorimetry [44, 45, 43] in the range $|\eta| < 1.7$ is separated into a large barrel and two smaller extended barrel cylinders, which are on both sides of the central barrel. This calorimetry is provided by a scintillator-tile calorimeter. LAr is also used for the hadronic calorimeters in the end-

caps covering range $|\eta| > 1.5$. The hadronic calorimeters also use LAr technology to cover outer $|\eta|$ limits of end-cap electromagnetic calorimeters. Both electromagnetic and hadronic calorimeters use LAr and could cover the pseudorapidity up to range $|\eta| > 4.9$.

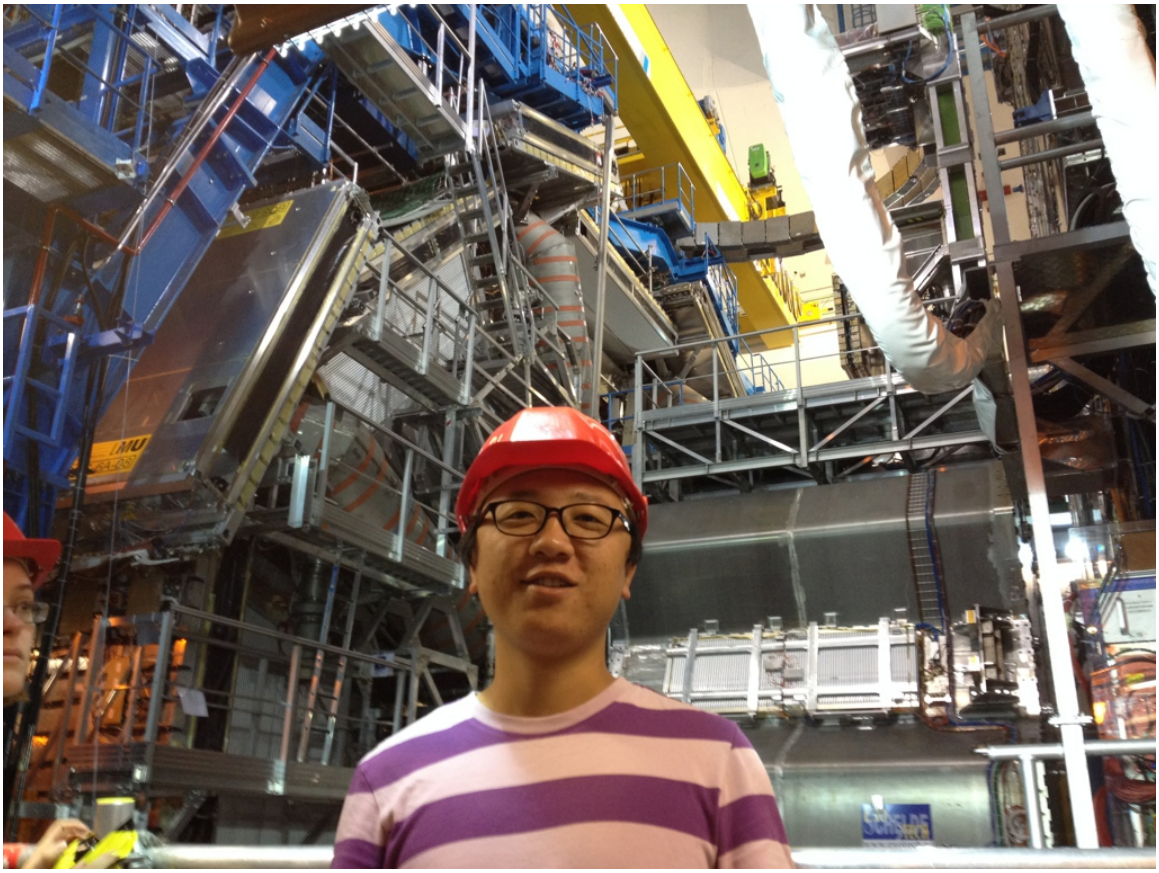

Figure 3.2: Photo of myself standing in front of the toroid magnets of ATLAS, year 2014 during the ATLAS upgrade

The muon spectrometer [46] is located outside the calorimeter. The air-core toroid system provides very strong magnetic field which has strong bending power in a large volume in a light and open structure. This toroid system contains a long barrel and two end-cap magnets. Thus excellent muon momentum resolution is achieved by three layers of high precision tracking chambers with multiple-scattering effects suppressed. The trigger chambers with timing resolution of order 1.5-4 ns play a key component

in the muon spectrometers. Since the muon spectrometer is at the very outside of the ATLAS detector, it defines the overall dimensions of the ATLAS detector.

The trigger system [47, 48] of ATLAS detector plays crucial role in the process of detecting particles. The ATLAS trigger system is like the brain of the detector. It is smart and quick enough to decide which events will be discarded and which events will be recorded. The designed luminosity of LHC is of the order $10^{34} cm^{-2} s^{-1}$ which is equal approximately 40 MHz[1] frequency. However, due to restriction from technical and resource limitations, we could only record about 1 kHz which is far lower than 40 MHz. The Level-1(L1) trigger system uses a subset of the detector information to make a decision to only process the events we are interested. This reduces the data rate to about 100 kHz[1]. The high-level trigger which contains the Level-2(L2) trigger and event filter. These subsequent two levels of trigger system finally reduce the data-taking rate to around 1 kHz[1].

Searching for Higgs boson was one of the main goal of ATLAS detector, thus searching for Standard Model Higgs was used as a benchmark to establish the performance of the whole ATLAS detector and its sub-systems. All the benchmark physics goals have set a series of general requirements for ATLAS detectors:

- LHC has very high luminosity of collision beam which results in high event rates. So ATLAS has fast, radiation-hard electronics and sensor elements.
- ATLAS covers almost full azimuthal angle to get large acceptance in pseudorapidity.
- The momentum resolution and reconstruction efficiency of the inner tracker has to be very good.
- ATLAS has to have very good electromagnetic(EM) calorimetry for electron and photon, as well as good full-coverage hadronic calorimetry for jet and missing transverse energy(MET) measurement.

- Good muon identification and momentum resolution with wide coverage as well as ability to determine charge of high p_T muons are essential.

- Due to very high events rates, ATLAS has to be able to trigger low p_T objects with high efficiency and background rejection.

A cut away view of the ATLAS detector and sub systems are showed in Fig. 3.3, with comparison of the tiny size of human beings illustrated on the left of it.

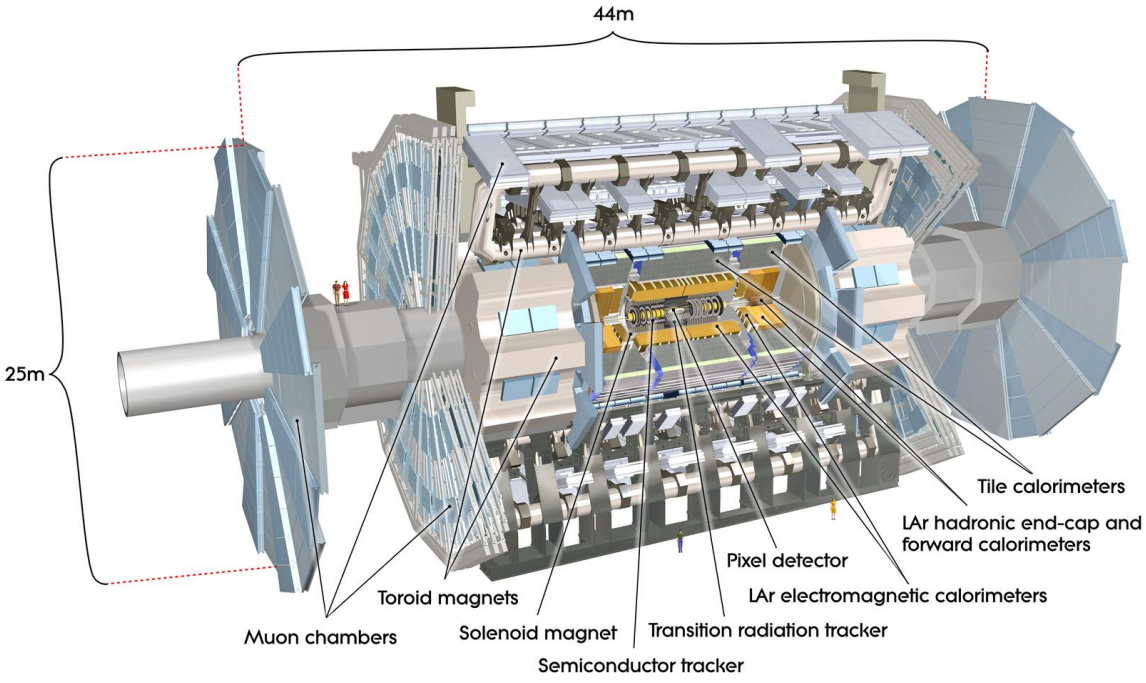

Figure 3.3: Cut-away view of the ATLAS detector and sub systems

3.2.1 Coordinate System

As the coordinate system [1] and nomenclature which is used to describe the ATLAS detector and the particles emerging from p-p collisions will be used many times, introducing the coordinate system of ATLAS first is needed. The coordinate system of ATLAS detector is a cylindrical coordinate system. The nominal interaction

point is defined as the origin of the coordinate system. The z-axis is defined to be along the beam direction. The x-y plane is defined as the plane which is transverse to the beam direction. The positive direction of x-axis is defined to be from the interaction point to the center of the LHC acceleration ring. The positive direction of the y-axis is defined to be from the interaction point upwards to the sky. The positive direction of z-axis is defined so that the x-axis, y-axis and z-axis will form a right-handed Cartesian coordinate system. The ATLAS detector's two end caps are located at side-A and side-C of the detector. Side-A of the detector is defined to be at the positive z direction and side-C is at the negative z direction. The azimuthal angle ϕ is defined as usual to be around the z-axis. The polar angle θ is the angle from the beam axis. Thus ϕ, θ are defined the same as in the usual cylindrical coordinate system. Instead of using the polar angle θ, we usually use the pseudorapidity defined as $\eta = -\ln\tan(\frac{\theta}{2})$ (for the very massive objects such as jets, we usually use rapidity $y = \frac{1}{2}\ln[\frac{(E+p_z)}{E-p_z}]$). Another variable we always use is called pseudorapidity-azimuthal distance ΔR in the angle space which is defined as $\Delta R = \sqrt{\Delta\eta^2 + \Delta\phi^2}$. Fig. 3.4 shows the ATLAS coordinate system.

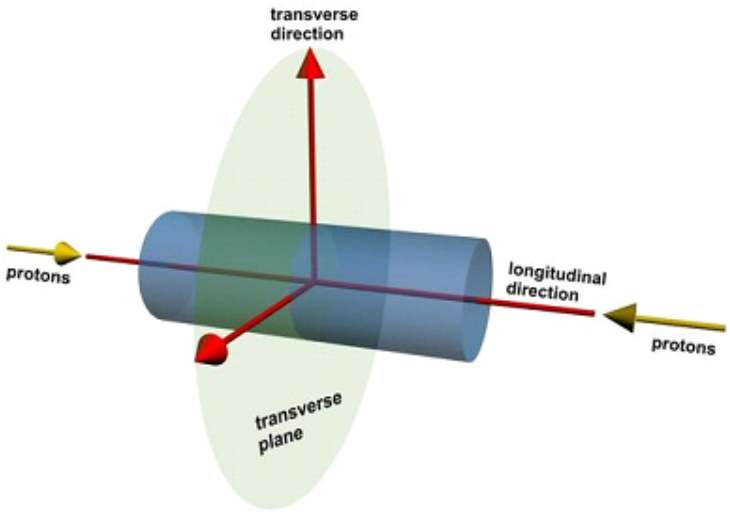

Figure 3.4: ATLAS coordinate system and the directions of the x, y, z axis directions

3.2.2 Tracking

The luminosity of LHC is at extremely high stage, which means there will be a very large track density in the detector. High precision measurements are made with fine detector to meet the requirements imposed by the bench mark physics processes on particle momentum and vertex resolution. These features are provided by the Pixel and silicon micro strip (SCT) trackers [49], as well as straw tubes of the Transition Radiation Tracker(TRT) [42].

Figure 3.5 shows a cut-away view of the ATLAS inner detector [40]. The size of the Inner Detector is 5.3 meters long and with a diameter of 2.5 meters. It's immersed in a 2T magnetic field which is used to bend the motion of the particles. The precision tracking detectors(pixels and SCT) cover a region with $|\eta| < 2.5$ [1]. The precision tracking detectors contains two parts: the barrel region, which are formed by concentric cylinders around the beam axis and the end-cap regions, which are located on disks perpendicular to the beam axis. The highest granularity is achieved around the vertex region using silicon pixel detectors. As shown in the figure, the pixel layers are segmented in R-ϕ and z with typically three pixel layers crossed by each track. The intrinsic resolution of the barrel regions are 10 μm (R-ϕ) and 115 μm (z). The resolution in the disks are 10 μm (R-ϕ) and 115 μm (z). There are about 80.4 million readout channels in the pixel detectors. There are eight strip layers to be crossed by each track for the SCT.

The TRT will provide a very large number of hits with the 4 mm diameter straw tubes, which enables track-following up to $|\eta| = 2.0$ [42]. The TRT only provides R-ϕ information with an intrinsic accuracy of 130 μm per straw. In the barrel region, the straws of the TRT are parallel to the beam axis with length equal to 144 cm. The barrel straws are divided into two halves at around $|\eta| = 0$. In the end-cap region, the straws are arranged radially in wheels with length of approximately 37 cm long. The total number of TRT readout channels is approximately 351000.

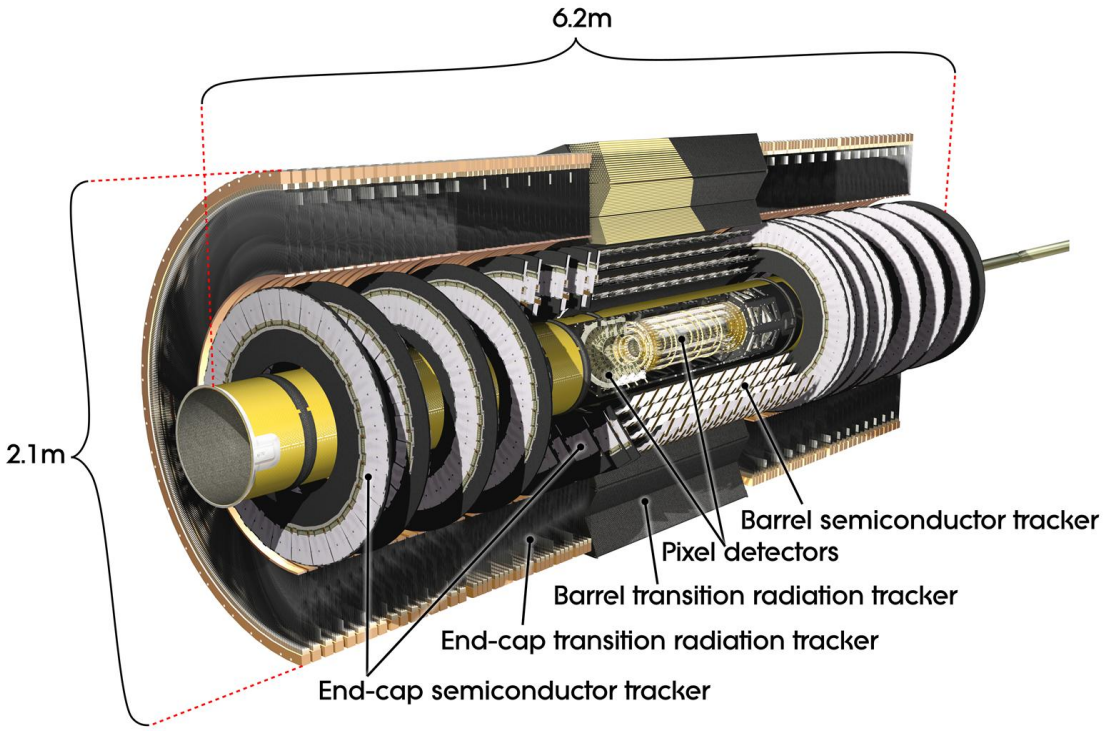

Figure 3.5: A cut-away view of the ATLAS inner detector

The combination of precision trackers at small radius together with the TRT at a larger radius gives very robust pattern recognition and high precision in R-ϕ and z coordinates. Hits at large radius contribute significantly to the momentum measurement.

The inner detector system provides tracking measurements in range matched by the precision measurements of the electromagnetic calorimeter. Besides these features, the electron identification capabilities are enhanced by the detection of transition-radiation photons in the xenon-based gas mixture of the straw tubes. Impact parameter measurements and vertex measuring for heavy-flavor and τ-lepton tagging could also be done by the semi-conductor trackers. The innermost layer of pixels are able to enhance the measurement of the secondary vertex too.

3.2.3 Calorimetry

Figure 3.6 gives a cut-away view of the ATLAS calorimeter system. These calorimeters cover the range of $|\eta| < 4.9$ [50], which is a very large range. The ATLAS calorimetry system[44, 45] uses different techniques to satisfy the widely varying requirements of the physics system and cover the very large η-range. The EM calorimeter has fine granularity to measure the electrons and photons precisely over the η region matched to the inner detector. The rest of the calorimeter system has coarser granularity which is sufficient to satisfy the physics requirements for jet reconstruction and E_T^{miss} measurements. The calorimetry system of ATLAS provides good containment for both electromagnetic and hadronic showers. Since the muon detectors are outside the calorimeters, calorimeters have to also keep particles from penetrating into the muon detectors. Because of this, the total thickness of the EM calorimeter is a very important consideration when designing. The total thickness of the EM calorimeter is over 22 radiation lengths(X_0) in the barrel region and over 24 X_0 in the end-cap region. In order to get good resolution for high energy jets, the hadronic calorimeter in the barrel regions have about 9.7 interaction lengths(λ) and end-cap regions has about 10 λ. The total thickness of 11 λ at $\eta = 0$ which is the shortest distance to the muon detectors is sufficient to stop particles from entering into the muon detectors. This thickness can also ensure a good E_T^{miss} measurement for many physics signatures, particularly for SUSY searches with the help of large η-coverage. Both the electromagnetic calorimeter and the hadronic calorimeter will be briefly introduced.

The EM calorimeter is divided into two parts: barrel part and two end-cap parts. The barrel part covers region with $|\eta| < 1.475$ and the end-cap parts cover the region with $1.375 < |\eta| < 3.2$. The EM calorimeter is a lead-LAr detector with kapton electrodes and lead absorber plates covering its full coverage. The accordion shaped absorber provides complete ϕ symmetry with no crack region in the azimuthal direc-

tion. Different position with different η has different lead thickness in the absorber plates. The thickness is optimized for different η as a function of EM calorimeter performance. The barrel calorimeter consists two identical half-barrels with a 4 mm gap at $z = 0$. Each of the two end-cap calorimeters has two coaxial wheels. The outer wheel covers the η region $1.375 < |\eta| < 2.5$ and the inner wheel covers $2.5 < |\eta| < 3.2$.

The hadronic calorimeters have three parts: the tile calorimeter, the LAr hadronic end-cap calorimeter and the LAr forward calorimeter. The tile calorimeter is positioned right outside the barrel EM calorimeter envelope. The barrel part covers region $|\eta| < 1.0$. The two extended barrel parts as shown in figure 3.6 cover the region $0.8 < |\eta| < 1.7$. The tile calorimeter is a sampling calorimeter with steel as absorber and scintillating tiles as the active material. The barrel and extended parts are divided into 64 modules in azimuthal direction and 3 layers in the radial direction. The total thickness of the tile calorimeter at the outer edge is around 9.7 λ at $\eta = 0$. The LAr Hadronic End-cap Calorimeter(HEC) has two independent coaxial wheels per end-cap. Both of the wheels are located behind the end-cap electromagnetic calorimeter. Each of the wheels is made of 32 identical wedge-shaped modules. Each end-cap has totally four layers in depth dividing each wheel into two segments. The wheels are made of copper plates with increasing thickness from the interaction point to further distance away. The outer radius of the copper plates is 2.03 m and the inner radius is 0.475 m. These copper leaves have LAr in between with thickness of 8.5 mm as the active medium for the sampling calorimeter. The Forward Calorimeter(FCal) is integrated into the end-cap cryostats in the forward direction to give uniformity of the calorimetric coverage as well as reduce the radiation background levels in the muon spectrometer. The FCal uses a really high-density design as the front face of the FCal is recessed by about 1.2 meters with respect to the EM calorimeter front face. The FCal is about 10 interaction lengths deep and each end-cap consists three modules. The inner module is made of copper for electromagnetic measurements.

The other two modules are made of tungsten for hadronic interaction measurement. Each module consists of a metal matrix, with regularly spaced longitudinal channels filled with the electrode structure consisting of concentric rods and tubes parallel to the beam axis. The LAr in the gap between the rod and the tube is the sensitive medium. This geometry allows for excellent control of the gaps, which are as small as 0.25 mm in the first section, in order to avoid problems due to ion buildup.

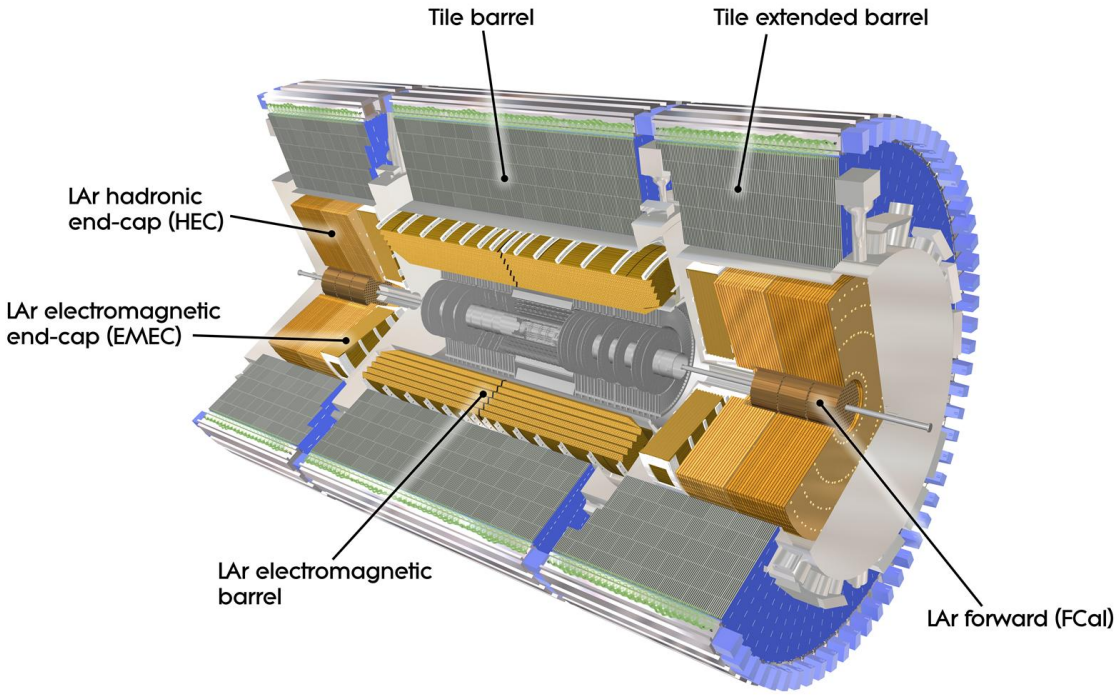

Figure 3.6: Cut-away view of the ATLAS calorimeter system

3.2.4 Muon system

The muon spectrometer [46] of ATLAS is designed to detect charged particles going through and to measure their momentum within the pseudorapidity range $|\eta| < 2.7$. The muon system is also part of the trigger system to trigger on particles within region $|\eta| < 2.4$. The muon spectrometer is located at the very outside of the

whole ATLAS detector. Muon with momenta down to several GeV (3 GeV, due to energy loss in the calorimeters) could be measured alone by the muon spectrometer. The driving performance goal of the muon spectrometer is to reach a stand-alone transverse momentum resolution of approximately 10% for 1 TeV tracks which could translate to a sagitta along the z direction of about 500 μm, to be measured with a resolution of $\leq$ 50 μm. The muon spectrometer could also get adequate momentum resolution and excellent charge identification at high end of the accessible range(3 TeV) by stand-alone measurement.

The precision-tracking chambers have two groups. The end-cap chambers are in front and behind the two end-cap toroid magnets, while the chambers in the barrel region are located between and on the eight coils of the superconducting barrel toroid magnets. The muon chamber system is symmetric around ϕ angle as similar to the symmetry of the toroids, which consists of eight octants. Each octant is sub-divided along azimuthal direction in two sectors with slightly lateral extensions, one large and one small sector, leading to a region of overlap along ϕ. The overlap of the chambers minimizes the gaps in detector coverage. The relative alignment of the adjacent sectors could also be done using the tracks recorded by both the large and small chambers.

The chambers in the barrel are arranged in three concentric cylindrical shells around the beam axis at radii of around 5 meters, 7.5 meters, and 10 meters. The end-cap chambers from large the wheels are perpendicular to the beam direction and located at distance of $|z| \approx$ 7.4 meters, 10.8 meters, 14 meters, 21.5 meters from the integration point. Figure 3.7 shows the cross section view of the muon system in the plane transverse to the beam axis. Figure 3.8 gives the cross section view of the muon system in the plane along the beam axis, z direction.

There are gaps left in the chamber coverage for various purposes in the muon spectrometer. The gap in the center of the detector($|\eta| \approx 0$) is left to allow services

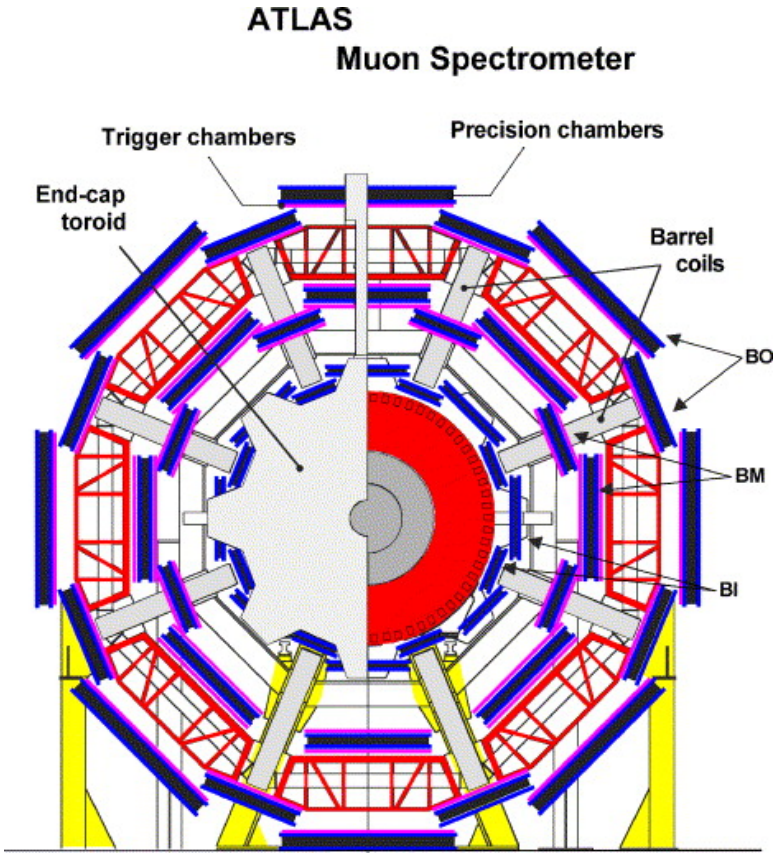

Figure 3.7: Cross-section view of muon system in the plane transverse to the beam axis, $x - y$ plane

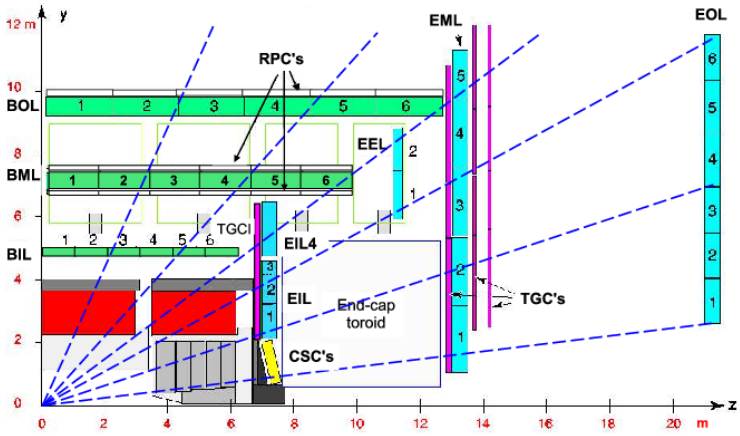

Figure 3.8: Cross-section view of the muon system in the plane along the beam axis, z direction.

to the solenoid magnet, calorimeters and inner detector. This will cause a missing recording angular region of the muon spectrometer about $\pm$ 4.8° ($|\eta| \leq 0.08$) if measured from the interaction point in the large sectors and $\pm$ 2.3° ($|\eta| \leq 0.04$) in the small sectors. The other gaps appear in sectors 12 and 14 due to the support structure(feet) of the ATLAS detector.

The precision momentum measurement is performed by the Monitored Drift Tube chambers(MDT's) [51] at $|\eta| \leq 2.0$. The MDT chambers have three to eight layers of drift tubes, operated at an absolute pressure of 3 bar with an average resolution of 80 μm per tube(35 μm per chamber). In the forward region($2 \leq |\eta| \leq 2.7$), Cathode-Strip Chambers(CSC) [52] are used in the inner most tracking layer because of its higher rate capability and time resolution. The CSC's are multi-wire proportional chambers with cathode planes segmented into strips in orthogonal directions. The resolution of a chamber is 40 μm in the bending plane and about 5 mm in the transverse plane. The MDT wires and CSC strips are located along a muon trajectory within 30 μm using a high-precision optical alignment system.

Another essential design criterion of the muon system was to trigger on muon tracks. A system of fast trigger chambers capable of delivering track information within a few tens of nano-seconds after passage of the particles is designed for the precision-tracking chambers. Resistive Plate Chambers(RPC) [53] and Thin Gap Chambers(TGC) [46, 54] are responsible for the fast triggering in the barrel region($|\eta| \leq 1.05$) and in the end-cap($1.05 \leq |\eta| \leq 2.4$) region. Both of the two types of chambers deliver signals within a spread of 15-25 ns, thus providing the ability to tag the beam-crossing. The trigger chambers measure the track in two dimensions, one in the bending(η) plane and one in the non-bending(ϕ) plane.

The purpose of the precision-tracking chambers is to determine the coordinate of the track in the bending plane. To get the chamber's coordinate in the non-bending plane, we match the MDT and trigger chamber hits in the bending plane and find

the chamber's coordinate in the non-bending plane as the second coordinate of the MDT measurement.

As the muon system is located at the very outside of the ATLAS detector, it has to be designed to tolerate the radiation levels in the experimental hall to protect the detectors and electronics inside from aging effect caused by the radiation. All the components in muon system are required to test under a radiation which is five times of the prediction level by the simulation studies.

3.2.5 Forward detectors

Three smaller sets of detectors are built to provide good coverage in the very forward region(small $|\eta|$) besides the main ATLAS detector systems described before.

Starting from the interacting point along the beam direction, the systems are Cerenkov detector which is called LUCID(LUminosity measurement using Cerenkov Integrating Detector), Zero-Degree Calorimeter(ZDC) and the absolute luminosity detector ALFA(Absolute Luminosity For ATLAS) [55]. LUCID is the main relative luminosity monitor in ATLAS. It's located at a distance of $\pm$17 m from the interaction point, close to TAS(Target Absorber Secondaries) collimator. Zero-Degree Calorimeter(ZDC) is located at $\pm$ 140m which is the point where the LHC beam-pipe is divided into two separate pipes. The ZDC is actually right after beam-pipe splitting point. The ZDC is mainly responsible for detecting forward neutrons in heavy-ion collisions. Absolute luminosity detector ALFA is the farthest detector at approximately $\pm$ 240m from the interaction point. In addition to all the detectors described before, the proton-tagging detectors are located at a even farther distance about $\pm$ 420m from the interaction point.

3.2.6 Trigger,readout, data acquisition, and control systems

The trigger system [47, 48] on ATLAS detector consists three level selections: Level-1 (L1) [47], Level-2 (L2)[48], and event filter. The High-Level Trigger(HLT)[48] refers to the L2 and event filter combined. The L1 trigger is implemented using custom-made electronics specially designed for ATLAS. However, the HLT's are almost all using commercial computers and networking hardware. The diagram of the trigger and data acquisition systems are shown in figure 3.9. The L1 trigger uses the

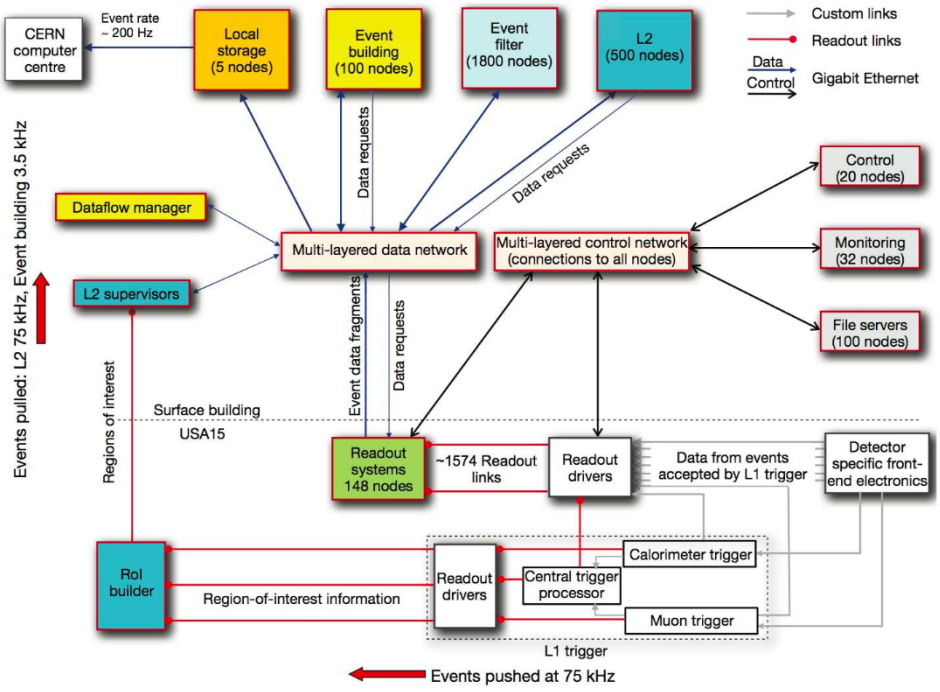

Figure 3.9: Block diagram of the ATLAS trigger and data acquisition systems

signatures from high-p_T muons, electrons/photons, jets, and τ-leptons which decays into hadrons to identify particle decay events. The L1 triggers will also seek events with large missing transverse energy(E_T^{miss}) and large total transverse energy by using reduced-granularity information from a subset of detectors: the Resistive Plate Chambers(RPC) and Thin-Cap Chambers(TGC) for high p_T muons, calorimeter subsystems for electromagnetic clusters, jets, τ-leptons, E_T^{miss}, and large total transverse

energy. The Level-1 trigger reduces the event rate from approximately 40 MHz to 100 kHz[1]. The decision time for a Level-1 accept is $2.5\mu s$.

The Level-2 trigger is seeded by Region-of-Interest(RoI's). These regions follow the area where the L1 trigger has identified possible triggered objects within the event. For Run-2, the Level-2 trigger and event filter computer clusters have been merged into a single event processing HLT farm, which reduces the complexity and allows for dynamic resource sharing between algorithms. This new arrangement reduces code and algorithm duplication which results in a more flexible HLT, reducing duplicated data-fetching.

The HLT algorithms use the full granularity and precision of calorimeter and muon chamber data combined with data from inner detector, to refine the trigger selections. The threshold cuts are improved by good information on energy deposition. Particle identification is enhanced significantly by track reconstruction in the inner detector. The HLT further reduces the events rate from approximately 100 kHz to around 1 kHz.

The data acquisition system(DAQ)[56, 48] receives and buffers the event data from the L1 trigger through readout electronics. The rate will be at L1 trigger rate. The data transmission is performed over point-to-point Readout Links(ROL's). The HLT will request event information from the DAQ system then. For those events fulfilling the L2 trigger selection criteria, they will be used for event-building. The assembled events will be then moved to the event filter for future event selection. The events finally going through event selection will be moved to permanent event storage. The DAQ system, not only controls the movement of data transit in the trigger selection chains, but also provides configuration, controlling and monitoring of the ATLAS detector during data-taking. The Detector Control System(DCS) [57] is responsible for the supervision of detector hardware, for instance, gas systems, power-supply voltages, etc.

CHAPTER IV

Object Reconstruction and Identification

When particles go through different sub-detectors in ATLAS detector, the trigger and data processing system of ATLAS will process and record these signals. The data is saved in different pieces categorized by different sub-detectors. The data at this stage can't be used by physicists for data analysis as it has to go through further processing. The data used for physics analysis has to be object-based which means physicists have to transform and combine the information from different sub-detectors to the information (information of vertex, track, momentum or energy, etc) of different type of particles. This process is called object reconstruction and identification. Reconstruction is the process which combines all the data in different sub-detector of ATLAS to get information about the vertex, track, momentum and energy information associated to certain particles. Only object reconstruction is not enough, furthermore, we also need to identify what kind of particles are associated with the reconstructed information. This process is called object identification. Object reconstruction and identification play important role in physics data analysis because they are the step converting the electric signals and data to physical objects which could be directly used by physicists. On the other hand, the reconstruction and identification are usually associated with significant systematic uncertainties which will affect the sensitivity of a data analysis. So getting an idea about how the reconstruction and

identification work are quite critical.

In the $bb\tau\tau$ analysis, there are electrons, muons, τs ,jets and $E_{\mathrm{T}}^{\mathrm{miss}}$ involved. So there will be discussion on the procedures of reconstructing and identifying these specific types of objects. As we further require some of the jets to be b-tagged, the b-tagging and overlap removal algorithms are discussed within this chapters as well.

4.1 Electrons

Electrons are reconstructed and selected using the measured track properties and shape of energy deposit clusters in the calorimeter, track-to-cluster matching information and the quality of the track. Electron candidates are identified using a likelihood technique [58].

The electron reconstruction procedure consists fitting a track using Inner Detector information and matching it to an energy cluster in the EM calorimeter. Not all of the objects built by the electron reconstruction algorithms are prompt electrons which are considered signal objects. Electron identification(ID) algorithms are then applied after the reconstruction in order to discriminate between prompt, isolated electron candidates(signal) from background-like objects. The background-like objects could possibly come from photon conversions, hadron mis-identification and heavy flavor decays. Figure 4.1 shows how one electron is reconstructed and identified, as well as, the sub-detectors involved in the procedure. There are three levels of electron identification operating points typically provided for electron ID. These are referred as *Loose*, $Medium$, and $Tight$. $Tight$ operating point has the highest background rejection efficiency, while *Loose* working point has the lowest. The operating points are defined such that the set of electron candidates with higher background rejection is a subset of the electron candidates with lower background rejection ($Tight \subset Medium \subset Loose$) [58]. In other words, electrons passing $Tight$ operating point will also pass $Medium$ and *Loose* operating point, for instance.

Loose working point is required for electrons to be passed in this analysis. The *Loose* working point with additional track hit requirement will provide an electron identification efficiency of 95%. The four-momentum of the central electrons ($|\eta| \leq 2.47$) is computed using both the information in the final cluster and the track from inner detector best matched to the original seed cluster. The electron energy is given by the cluster energy. Electron candidates are required to have $p_T \geq 7$ GeV. Due to the barrel-end cap transition region of the calorimeter(Crack Region), the electron candidates in region with $1.37 \leq |\eta| \leq 1.52$ are vetoed. In order to further reject hadronic jets misidentified as electrons, the electrons are required to be isolated by imposing the *Loose* isolation working point requirement. Two of the main isolation variables used are calorimeter-based isolation and track-based isolation. The isolation requires no near-by tracks or calorimeter energy deposits with in a variable size(p_T dependent). This isolation requirement could be inverted to provide control region for estimating background in the signal region.

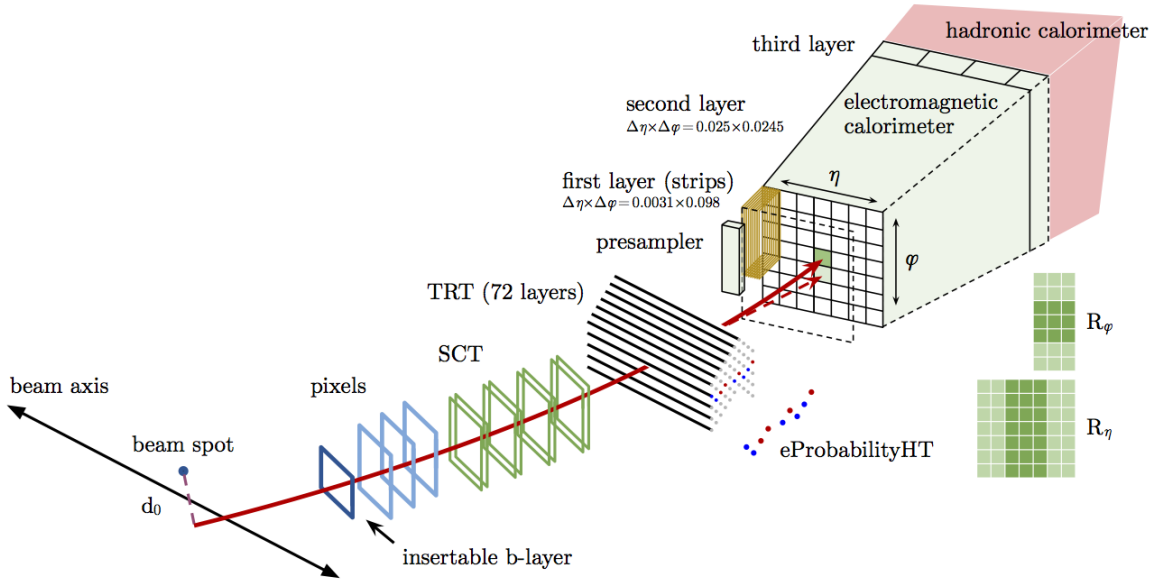

Figure 4.1: Schematic view of the electron reconstruction and identification procedure and the sub-detectors involved

4.2 Muons

Information primarily from the inner detector(ID) and muon spectrometer(MS), supplemented by information from the calorimeters, is used to identify and precisely reconstruct muons in ATLAS detector [59]. Muon reconstruction is first performed independently in the inner detector and muon spectrometer. Then the information from individual sub-detectors is combined to form the muon tracks which will be used in physics analysis.

The muon spectrometer(MS) is the outermost sub-detectors on ATLAS. The goal of MS is to detect charged particles in the pseudorapidity region $|\eta| \leq 2.7$, and provide high momentum resolution better than 3% over a wide p_T range and up to 10% at $p_T \approx 1$ TeV. The Resistive Plate Chambers(RPC, three doublet layers for $|\eta| \leq 1.05$) together with the Thin Gap Chambers(TGC, three triplet and doublet layers for $1.0 \leq |\eta| \leq 2.4$) provide triggering and η, ϕ position measurements of muons. Precise muon momentum measurement is possible up to region $|\eta| = 2.7$ by three layers of Monitored Drift Tube Chambers(MDT). Each of the MDT chamber provide 6 to 8 η measurements along the muon track. The Cathode Strip Chambers(CSC) is installed in the inner layer instead of MDTs for region with $|\eta| \geq 2.0$ in the end cap region for muon momentum measurement. The single hit resolution in the bending plane for the MDT and the CSC is about 80 μm and 60 μm, respectively. Muon reconstruction in the MS starts with a search for hit pattern inside each muon chamber to form segments. The MDT segments are then reconstructed by performing a straight-line fit to the hits found in each layer. The coordinate orthogonal to the bending plane will be provided by the RPC or TGC hits. Segments in the CSC detectors are built using a separate combinational search in the η and ϕ detector plane. The muon track candidates are then built by fitting together hits from segments in different layers. The algorithm used a segment-seeded combinational search starting with the segments generated in the middle layers of the detector where more trigger hits are

available. The search is then extended to use the segments in outer and inner layers as seeds. At least two matching segments are required to build a track in the barrel or endcap region. However, in the barrel-endcap transition region, a single high quality segment with η and ϕ information is enough to build a track. When building the track initially, one segment could be used for different track candidates. The overlap removal algorithm will select the best assignment to a single track or let two tracks share the same segment later. A global χ^2 fit is performed on the hits associated with each track. We will accept the track candidate if the χ^2 of the fit satisfies the selection criteria. Hits providing large contribution to the χ^2 are removed and the track fit is repeated. A hit recovery procedure is also performed looking for additional hits consistent with the candidate trajectory. The track candidate is refit if additional hits are found.

The inner detector(ID) provides an independent measurement of the muon track close to the interaction point. The Silicon Pixels($|\eta| \leq 2.0$), Semi-Conductor Tracker($|\eta| \leq 2.0$) and Radiation Tracker$|\eta| \leq 2.5$ provide high-resolution coordinate measurements for track reconstruction inside an axial magnetic field of 2 T. The reconstructed track in the barrel region has typically 3 Pixel hits, 8 SCT hits, and approximately 30 TRT hits. The muon reconstruction in the inner detector will be similar to other charged particle in the inner detector.

Muon identification is performed according to several reconstruction criteria which will give different muon "types". Based on the availability of information from MS or ID, we define the different types of muon as:

- **Stand-Alone(SA) muons**: the muon trajectory is reconstructed only in the MS. The parameters of the muon track at the interaction point are determined by extrapolating the track back to the point of closest approach to the beam line with consideration of the energy lost in the calorimeter between ID and MS. SA muons are mainly used to extend acceptance in the η range, $2.5 \leq |\eta| \leq 2.7$

which is not covered by the ID. In general, the muons have to transverse at least two layers of MS chambers to provide a track measurement.

- **Combined(CB) muons**: This is the main type of the reconstructed muons. The track reconstruction is performed independently first in the ID and MS. Then a combined track is reconstructed from the independent MS track and ID track.

- **Segment-tagged(ST) muons**: A track in the ID with extrapolated track in the MS associated with at least one local track segment in the MDT or CSC chambers. ST muons are used to increase the acceptance for muons which crossed only one layer of the MS chambers. These muons are usually either have low p_T or fall into regions with low MS acceptance.

- **Calorimeter-tagged(CaloTag) muons**: A track in the ID associated to an energy deposit in the calorimeter compatible with a minimum ionizing particle. This type of muon clearly has the lowest purity because there is no MS information used when reconstructing. However, it recovers acceptance in the uninstrumented regions of the MS. The identification criteria of this muon type is optimized for a region of $|\eta| \leq 0.1$.

The muon candidates are required to have $p_T \geq 7$ GeV, $|\eta| \leq 2.7$ with passing the *loose* identification criteria. The equivalent *loose* working point is used to apply isolation requirements in the tracking detectors and calorimeters to reject non-prompt muons with 99% efficiency, independent of p_T. Same as the electron, the isolation criteria could be reversed to define the control region for validation and possible background estimation too.

4.3 τs

The τ leptons decay either leptonically($\tau \to \ell\nu_\ell\nu_\tau$, $\ell = e, \mu$) or hadronically ($\tau \to$ hadrons + ν_τ, denoted τ_{had}). The proper decay length of τ lepton is 87 μm, meaning that τ leptons decay typically before reaching the active regions of the ATLAS inner detector. Thus, τ could only be identified using its decay products. In this section, only the hadronic τ is considered [60, 61, 62]. As for leptonically decayed τs, we identify their direct decay product, electrons or muons, and process together with the reconstructed hadronic τs when reconstructing the di-τ invariant mass using MMC [63]. The branching ratio of the hadronic τ decay is 65%. Among the hadronic τ decay, one or three charged pions are presented with branching ratio equal to 72% and 22% respectively. The rest 6% of hadronic τ decays are with charged kaons presented mostly. Approximated among 78% of all hadronic τ decays, at most one associated neutral pion is produced [64]. These neutral and charged hadrons from τ decays are the visible decay products of the τ leptons and will be referred as $\tau_{had-vis}$ later.

The main background to the τ hadronic decays is from jets of energetic hadrons produced via fragmentation of quarks and gluons. This kind of background is already presented at the trigger level, which we also refer as *online* level. An electron or a muon could also be misidentified as hadronically decayed τ with leptons misidentified as the charged hadron from τ decay. Information from the narrow shower shape, the distinct number of charged particle tracks and the displaced τ lepton decay vertex are used for both *online* and *offline* event reconstruction.

The $\tau_{had-vis}$ reconstruction is seeded by the energy deposits which have been constructed as individual jet in the calorimeter. The jets are formed using the anti-k_T algorithm which was presented in the jets reconstruction section with distance parameter $R = 0.4$ and calibrated using a local hadronic calibration(LC). Such jets used the calorimeter TopoClusters as inputs. These jets must satisfy the following requirement in order to seed a $\tau_{had-vis}$ candidate:

- $p_T > 10$ GeV
- $|\eta| \leq 2.5$
- A reconstructed primary vertex, at least three associated tracks.

If one or more primary vertices candidates are present, the one with highest $\Sigma p^2_{T,tracks}$ is chosen. Inside one event, multiple simultaneous interactions could be presented, sometimes the chosen primary vertex does not always correspond to the vertex at which the τ lepton is produced. To reduce the pile-ups and increase the reconstruction efficiency, the τ lepton production vertex is identified among the previously reconstructed primary vertex candidates in the event.

The τ vertex(TV) association algorithm uses information from all tracks with p_T > 1 GeV within the region $\Delta R < 0.2$ around the jet seed direction. All these tracks are also required to pass quality criteria based on the number of hits in the inner detector(ID). The p_T of these tracks is summed and the primary vertex candidate to which the largest fraction of the p_T sum is matched is chosen as the TV. New impact parameters are recalculated with respect to the TV and $\tau_{had-vis}$ tracks are selected. TV will be used to determine the $\tau_{had-vis}$ direction, associate tracks and build the coordinate system for the identification variables.

To calculate the three-momentum of $\tau_{had-vis}$, the η and ϕ of the barycenter of the jet seed TopoCluster, which are calibrated at the local hadronic calibration, have to be first computed assuming zero mass for each constituent. The four-momenta of all clusters in the region $\Delta R < 0.2$ around the barycenter are recalculated using the TV coordinates. All the four-momenta are summed later to get the momentum magnitude p^{LC} and the direction of $\tau_{had-vis}$. The mass of the τ_{had} is defined to be zero.

Tracks are associated to the $\tau_{had-vis}$ candidate following the criteria below:

- Tracks have to be in the core region $\Delta R < 0.2$ around the τ_{had} direction.

- Tracks' $p_T > 1$ GeV
- At least 2 associated hits in the pixel detector(including the Insertable B-Layer(IBL)), at least 7 hits in total in the pixel and SCT detectors.
- The closest approach of the track to the TV in the transverse plane $|d_0| < 1.0$ mm, and longitudinally, $|\Delta z_0 sin\theta| < 1.5$ mm

The tracks in the region $0.2 < \Delta R < 0.4$ are used for calculating the identification variables and required to satisfy the same selection criteria. These selection criteria is used when classifying $\tau_{had-vis}$ candidates as a function of its number of associated tracks. The distribution of the number of tracks associated to $\tau_{had-vis}$ candidates is displayed in Fig 4.2 respectively for 1-prong and 3-prong τ decays. Main cause of the underestimation of the number of prongs is tracking inefficiency due to hadronic interactions in the inner detector, while the leading cause of the overestimation of the number of prongs comes from photon conversion tracks which pass the track selection criteria. The reconstruction efficiency is defined as the fraction of 1-prong(3-prong) hadronic τ which are reconstructed as 1-track(3-track) $\tau_{had-vis}$ candidates. The track and vertex selection described before play the dominant role for the reconstruction efficiency. The reconstruction efficiency for 1-prong decays is relatively constant over the whole $\tau_{had-vis}$ p_T range as it is showed in Fig 4.3. However, there is reductions on the efficiency plot for 3-prong decays on very low and high p_T region. The low-p_T region reduction is due to the failure of the minimum transverse momentum requirement on the charged particles, while the high-p_T region is due to the increased collimation of the decay products which leads to an increased probability to miss a track because of overlapping trajectories.

As mentioned before, the jets of energetic hadrons produced via fragmentation of quarks and gluons are the main background which is already presented at the trigger(*online*) level. While the reconstruction of $\tau_{had-vis}$ candidates provide very

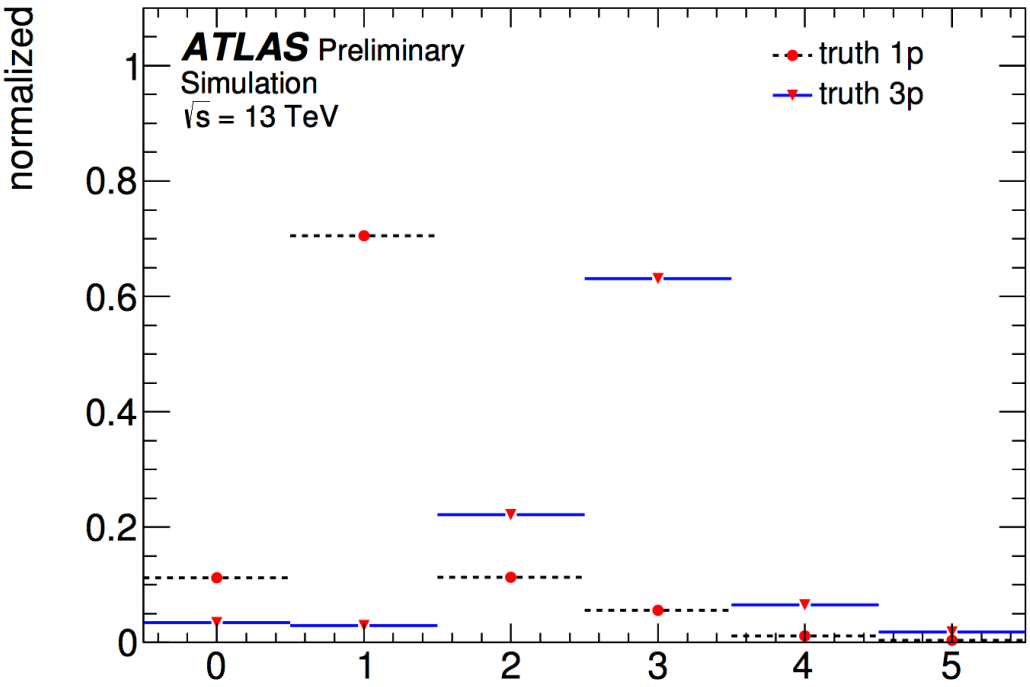

Figure 4.2: Number of reconstructed tracks for $\tau_{had-vis}$ candidates from true 1-prong and 3-prong τ decays.

little rejection against these jet background, a rejection against jets with a separate identification step using the discriminant variables is applied. This rejection method uses the information of the tracks and TopoClusters in the core and isolation region around the $\tau_{had-vis}$ candidate direction. The calorimeter provides information about the longitudinal and lateral shower shape. The ECAL is sensitive to the π^0 content of τ hadronic decays which provide extra information. Separate Boosted Decision Trees(BDT) algorithms are trained for 1-track and 3-track $\tau_{had-vis}$ decays using samples: $Z/\gamma^* \rightarrow \tau\tau$ as signal and di-jet events as background. The full list of the inputs variables for BDT training is provided below and summarized in Table 4.3:

- **Central energy fraction(f_{cent})**: Fraction of the calorimeter transverse energy deposited in the region $\Delta R < 0.1$ with respect to all energy deposited in the region $\Delta R < 0.2$ around the $\tau_{had-vis}$ candidate.

- **Leading track momentum fraction($f^{-1}_{leadtrack}$)** : The transverse energy

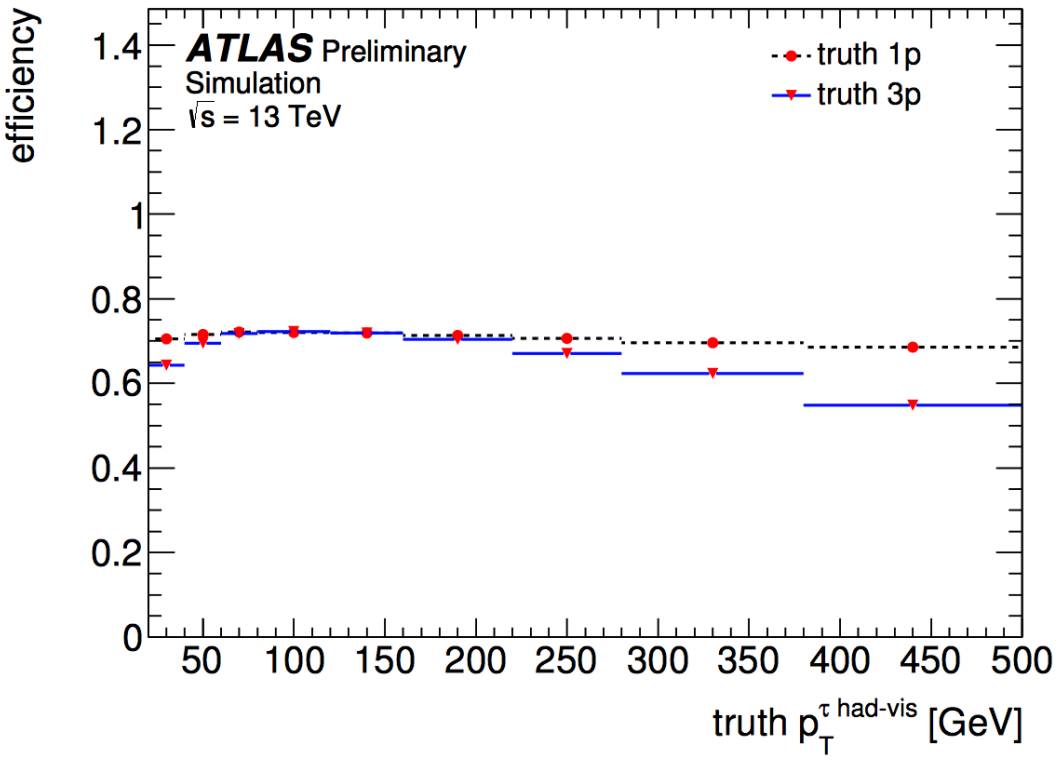

Figure 4.3: Reconstruction efficiency for 1-prong and 3-prong τ decays as a function of $\tau_{had-vis}$ p_T.

Variable	Offline	
	1-track	3-track
f_{cent}	✓	✓
f_{cent}	✓	✓
$f^{-1}_{leadtrack}$	✓	✓
$R^{0.2}_{track}$	✓	✓
$\lvert S_{leadtrack}\rvert$	✓	
f^{track}_{iso}	✓	
ΔR_{Max}		✓
S^{flight}_T		✓
m_{track}		✓
$f^{track-HAD}_{EM}$	✓	✓
f^{EM}_{track}	✓	✓
$m_{EM+track}$	✓	✓
$p_T^{EM+track}/p_T$	✓	✓

Table 4.1: Discrimination variables used as input to the BDT algorithms at offline reconstruction and at trigger level, for 1-track and 3-track $\tau_{had-vis}$ candidates. Check marks mean certain variables are used

sum, calibrated at the EM energy scale, deposited in all cells belonging to the TopoClusters in the core region of the $\tau_{had-vis}$ candidate, divided by the transverse momentum of the highest-p_T charged particle in the core region.

- **Track radius($R^{0.2}_{track}$)**: p_T-weighted ΔR distance of the associated tracks to the $\tau_{had-vis}$ direction, using only tracks in the core region.

- **Leading track IP significance($|S_{leadtrack}|$)**: Calculated with respect to the TV, the absolute value of the transverse impact parameter of the highest p_T track in the core region, divided by its estimated uncertainty.

- **Fraction of tracks p_T in the isolation region(f^{track}_{iso})**: ratio between scalar sum of the p_T of tracks associated with the $\tau_{had-vis}$ in the isolated region $0.2 < \Delta R < 0.4$ and the sum of the p_T of all tracks associated with the $\tau_{had-vis}$.

- **Maximum ΔR(ΔR_{Max})**: In the core region, the maximum ΔR between a track associated with the $\tau_{had-vis}$ candidate and the $\tau_{had-vis}$ direction.

- **Transverse flight path significance(S^{flight}_{T})**: This variable is only defined for multi-track $\tau_{had-vis}$ candidates. It's defined as the decay length of the secondary vertex from the tracks associated with the core region of the $\tau_{had-vis}$ candidate in the transverse plane, divided by its estimated uncertainty.

- **Track mass(m_{track})**: This is the invariant mass calculated from the sum of all four-momentum of all tracks in the core and isolation regions assuming a zero pion mass for each track.

- **Fraction of EM energy from charged pions($f^{track-HAD}_{EM}$)**: Fraction of the electromagnetic energy of the tracks associated with the $\tau_{had-vis}$ candidate in the core region.

- **Ratio of EM energy to track momentum(f_{track}^{EM})**: Sum of the cluster energy deposited in the electromagnetic part of each TopoCluster associated with the $\tau_{had-vis}$ candidate divided by the total sum of the momentum of tracks in the core region.

- **Track-plus-EM-system mass($m_{EM+track}$)**: Invariant mass of the system composed of the tracks and up to two most energetic EM clusters in the core region. The EM cluster energy is TopoCluster energy only deposited in the pre-sampler and first two layers of the EM calorimeter. When calculating the four-momentum of the EM cluster, zero mass and alignment with TopoCluster seed direction are assumed.

- **Ratio of track-plus-EM-system to p_T($p_T^{EM+track}/p_T$)**: Ratio of the $\tau_{had-vis}$ estimated from the vector sum of track momenta which is required to be up to two most energetic EM clusters in the core region to the calorimeter-only measurement of the p_T of $\tau_{had-vis}$.

There are three τ identification working points provided, labelled as *tight*, *medium* and *loose*. Each of them corresponding to different τ identification efficiency and background rejection power. The signal efficiency of different working points (ratio between number of reconstructed $\tau_{had-vis}$ candidates and number of true $\tau_{had-vis}$) for 1-prong and 3-prong τ decays could be seen in Fig 4.4. The BDT score is flatten using a 3D transformation to make the efficiency independent from the true $\tau_{had-vis}$ p_T. Fig 4.4 also shows that the efficiency will keep stable with respect to different pile-up conditions. 1-prong $\tau_{had-vis}$ has a better identification efficiency than the 3-prong $\tau_{had-vis}$). Generally, at low transverse momentum region, $\tau_{had-vis}$ candidates could achieve an 40% signal efficiency while the background rejection efficiency is at 60%. As part of the τ identification procedure, candidates with one core track overlap ($\Delta R < 0.4$) with an electron candidate($p_T > 5$ GeV) which has a high electron identification

likelihood score are rejected. In this analysis, the selected $\tau_{had-vis}$ candidates are required to have $p_T > 20$ GeV, with $|\eta| \leq 2.5$, 1-prong or 3-prong, unit charge and passing a *medium* working point.

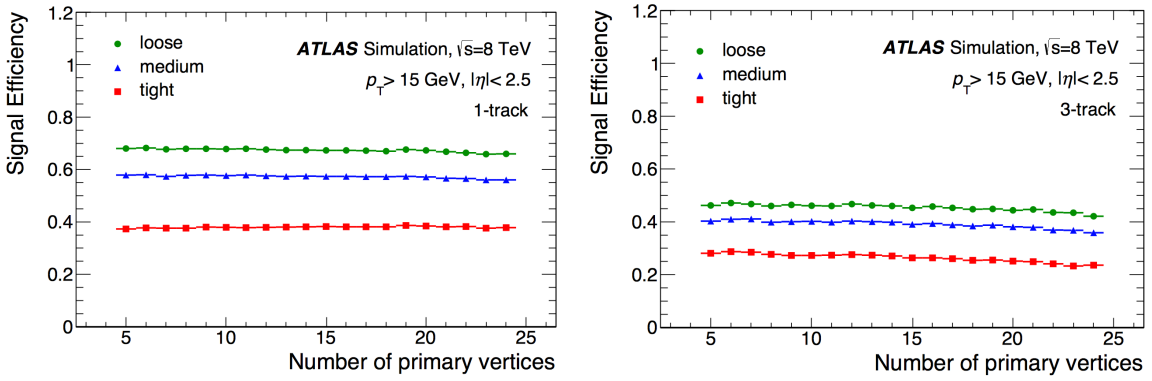

(a) (b)

Figure 4.4: Offline tau identification efficiency at different working point for (a) 1-prong τ decay and (b) 3-prong τ decay from SM and exotic processes in simulated data.

4.4 Jets

Jets are reconstructed using the anti-k_t algorithm [65] with a radius parameter $R = 0.4$ applied to topological clusters of energy deposits in calorimeter cells using the FASTJET software. The jet clustering algorithms are among the main tools for analyzing data from hadronic collisions. We introduce distances d_{ij} [65] between entities (particles, pseudojets) i and j and d_{iB} between the entity i and the beam (B) as showed in Eq. 4.1. Inside the equation, $\Delta_{ij}^2 = (y_i - y_j)^2 + (\phi_i - \phi_j)^2$, k_{tj} is the transverse momentum of the entity, y_i is the rapidity and ϕ_i is the azimuth of particle i. R is the usual radius parameter as 0.4 or 0.6. The parameter p is to govern the relative power of the energy versus geometrical scale. When p = -1, we refer it as the "anti-k_t" jet-clustering algorithm.

$$d_{ij} = min(k_{ti}^{2p}, k_{tj}^{2p}) \frac{\Delta_{ij}^2}{R^2} \tag{4.1a}$$

$$d_{iB} = k_{ti}^{2p} \tag{4.1b}$$

The clustering process will identify the smallest distance d_{ij} and recombine them if they are entities i and j. If the smallest distance is between entity and beam(B), we remove it from the list of entities. The distances are recalculated and the procedure repeated until no entities are left. For anti-k_t algorithm, $d_{ij} = min(1/k_{ti}^2, 1/k_{tj}^2)\Delta_{ij}^2/R^2$, which means the d_{ij} between similarly separated soft particles will be much larger than that between the hard particles. So in the anti-k_t algorithm, soft particles tend to cluster with hard particles long before they cluster among themselves. Hard and soft particles here are a shorthand to describe the kinematic energy of the particles. Hard particles will have more kinematic energy than the soft particles. If a hard particle has no hard neighbors within a distance $2R$, this hard particle will gather all the soft particle around itself within radius R, forming a perfectly conical jet. The anti-k_t algorithm's clustering preference makes it best at resolving jets but worst for studying jet substructures.

When we do the jet clustering using the anti-k_t algorithm, soft particles will not modify the shape of the jet, only the hard particles do. When $\Delta_{12} < R$, hard particle 1 and 2 will cluster to a single jet. The magnitude of the k_t will determine which particle the conical jet will be centered on. If $k_{t1} \gg k_{t2}$, the final single jet will be centered on $k1$, vice versa. However when $k_{t1} \sim k_{t2}$, the shape will be very complex, which will be a union of cones (radius $< R$) around each hard particle plus a cone(of radius R) centered on the final jet.

If another hard particle 2 is present such that $R < \Delta_{12} < 2R$, it's not possible for both to be perfectly conical. If $k_{t1} \gg k_{t2}$, jet 1 will be fully conical and jet 2 will be partly conical because jet 2 will miss the part overlapping with jet 1, vice versa. If $k_{t1} = k_{t2}$, neither of the jets will be conical and we will simply divide the overlap part with a straight line equally between them. When $k_{t1} \sim k_{t2}$, both of the cones will be

clipped with the boundary b between them defined as $\Delta R_{1b}/k_{t1} = \Delta_{2b}/k_{t2}$.

The jet energy is determined from reconstructed cluster energies at the electromagnetic scale. Correction factors derived from the simulation and data accounting for response of the calorimeter to hadrons are applied. The pile-up jets are suppressed using the tracking information [66]. All the jets in this analysis are required to have $p_T > 20$GeV, $|\eta| \leq 2.4$ and are cleaned for detector effects, beam backgrounds and cosmic rays.

4.4.1 b-tagging

A MV2 multivariate discriminant is used to identify the jets originating from b-quark [67, 68]. This discriminant is trained against a background sample containing 10% charm-initiated jets. The MV2 algorithm uses variables from basic b-tagging algorithms(IP2D, IP3D, SV1 and JetFitter) and combined them as a single multivariate discriminant. We use a working point which has average tagging efficiency of 70% for b-jets in $t\bar{t}$ events. This provides a rejection factor of around 381(12) against light(charm) jets.

Correction factors are applied to the simulated event samples to account for difference between data and simulation in the b-tagging efficiency for b, c, and light-jets. The correction for b-jets is derived from the $t\bar{t}$ events with two lepton final states. Jet energy of the b-tagged jets also needs to be corrected because the muon from semi-leptonic B-hadrons will carry away some amount of energy. To do this, we add the four-momentum of the closest muon within ΔR of a jet to the calorimeter-based jet energy after we removed the energy deposited by the muon in the calorimeter. The jet four-momentum is also multiplied by a p_T-dependent correction to account for biases in the response. This correction takes into account the effect of the momentum of the neutrinos produced in B-hadron semi-leptonic decays and improves the resolution of the di-b-jet mass distribution[69]. For non-dominant backgrounds

that are estimated from simulations but typically not produced in associated with b-jets, a "truth-tagging" technique is used in order to retain the full statistical power of the samples. For any given jet, a random MV2 weight above efficiency 70% is generated. Every event is weighted by the efficiency of each jet to actually pass the b-jet selection after the random MV2 value is generated. This technique is contrast from direct tagging. The direct tagging algorithm is applied to the simulated events and events failing a selection based on the b-tagging discriminant are removed. The truth-tagging is applied to all samples except signal, $t\bar{t}$, single top, and $Z \to \tau\tau + bb$ processes in this data analysis.

4.5 Missing transverse energy

The missing transverse momentum (E_T^{miss}) used in the data analysis is an object-based definition. The E_T^{miss} reconstruction process uses reconstructed, calibrated objects to estimate the transverse momentum imbalance in an event[70]. The definition of E_T^{miss} is showed in Eq. 4.2 as the sum of a number of components:

$$E_{x(y)}^{miss} = E_{x(y)}^{miss,e} + E_{x(y)}^{miss,\gamma} + E_{x(y)}^{miss,\tau} + E_{x(y)}^{miss,jets} + E_{x(y)}^{miss,\mu} + E_{x(y)}^{miss,soft} \tag{4.2}$$

The jet, charged lepton, photon terms are negative sum of the momenta for the respective calibrated objects. Calorimeter deposits are associated with reconstructed objects in the following order: electrons(e), photons(γ),hadronically decayed τ, jets and muons(μ). The soft term in the equation is reconstructed from the transverse momentum deposited in the detector without being associated with any reconstructed hard objects(The objects mentioned before.) This term could either be reconstructed using calorimeter-based methods or track-based methods. From the components of $E_{x(y)}^{miss}$, the magnitude E_T^{miss} and azimuthal angle ϕ^{miss} could be calculated as:

$$E_T^{miss} = \sqrt{(E_x^{miss})^2 + (E_y^{miss})^2} \tag{4.3a}$$

$$\phi^{miss} = arctan(\frac{E_y^{miss}}{E_x^{miss}}) \tag{4.3b}$$

The total transverse energy in an event is defined as the scalar sum of all transverse momenta of the objects used to calculate the E_T^{miss}:

$$\sum E_T = \sum p_T^e + \sum p_T^\gamma + \sum p_T^\tau + \sum p_T^{jets} + \sum p_T^\mu + \sum p_T^{soft} \tag{4.4}$$

In the case of the anti-τ used for the fake-τ background estimation, the E_T^{miss} is computed as a τ-like objects instead of a jet-like object to ensure they are calibrated at the τ energy scale rather than the jet energy scale.

4.6 Overlap removal

Objects that have a geometric overlap ($\Delta R = \sqrt{\Delta\eta^2 + \Delta\phi^2}$) are removed according to the following procedure:

- e-jet with $\Delta R = 0.2$. Priority is given to the electron.
- jet-e with $\Delta R = 0.4$. Priority is given to the jet.
- μ-jet with $\Delta R = 0.4$ and fewer than three 3 tracks with $p_T > 500\ MeV$. Priority is given to the μ.
- jet-μ with $\Delta R = 0.4$ and three or more tracks with $p_T > 500\ MeV$. Priority is given to the jets.
- $e - \mu$ with $\Delta R = 0.2$ and sharing an inner detector track. Priority is given to the μ.

- $\mu - \tau$ with $\Delta R = 0.2$. Priority is given to the μ.
- $e - \tau$ with $\Delta R = 0.2$. Priority is given to the electron.
- $\tau - jet$ with $\Delta R = 0.2$. Giving priority to the better reconstructed object with the following precedence:
  - BDT *medium* τ
  - b-tagged jet
  - antiID-τ
  - Light jet

The reconstruction and identification of individual objects have been discussed in this chapter. As different data analysis requires different objects to be present in the final state, thus different event reconstruction criteria will be applied accordingly. The event reconstructions of this data analysis will be discussed in Chapter V.

CHAPTER V

Event Selection

This analysis uses Boosted Decision Tree(BDT)[21] to isolate and discriminate signals from background instead of using series of cuts to do so. However, several pre-selection criteria have to be applied to get rid of significant amount of background before using BDT, as well as to define signal regions and control regions in both $\tau_\ell\tau_{\rm had}$ and $\tau_{\rm had}\tau_{\rm had}$ channels for the data analysis. The BDT plays a critical role in this analysis which turned out to be one of the key features we have chosen to make our final result stand out among all the di-Higgs final states analysis on both ATLAS and CMS.

5.1 Trigger and data cleaning

In the $\tau_\ell\tau_{had}$ channel, events are first checked to see if they pass one of the single lepton triggers(SLT). In the electron channel, multiple single electron triggers are used to maximize event acceptance. The events are required to have at least one electron with $p_T > 24\ GeV$, passing "medium" identification criteria and "loose" isolation requirements. In the later data-taking periods, the electron p_T threshold is raised to 26 GeV, with the identification working point changed to "tight", candidate events can also have at least one electron with $p_T > 60\ GeV$ that passes the identification criteria with no requirement on the isolation, or have at least one electron with $p_T >$

120-140 GeV which passes "loose" identification criteria. In the muon channel, events are required to have a muon with $p_T >$ 24-26 GeV corresponding to different data-taking periods, passing the "loose" isolation criteria or at least one muon with $p_T > 50$ GeV with no other requirements. For the events fail to pass the single lepton triggers, they are tested to see if they pass the lepton-plus-τ triggers(LTT). The LTT triggers require either an electron with $p_T > 17$ GeV or a muon with $p_T > 14$ GeV, together with a hadronic τ with $p_T > 25$ GeV. Both the electron and τ are required to pass their "medium" identification working points respectively. During the later data-taking periods, "loose" isolation criteria, which is equivalent to the corresponding offline isolation requirements, were applied to the light leptons(electrons or muons). Furthermore, during the 2016 data-taking campaign, the LTT are required to have an additional jet at Level-1 passing a 25 GeV p_T threshold.

In the $\tau_{had}\tau_{had}$ channel, events are first tested to see if they pass a single τ trigger(STT). The τs in the STT are required to have $p_T >$ 80-160 GeV. The p_T threshold depends on different data-taking periods. Both of the τs are required to pass the "medium" identification criteria. Events which fail to pass the STT are then tested to see if they pass a di-tau trigger(DTT) or not. The DTT triggers require the leading τ to have $p_T > 35$ GeV and sub-leading τ with $p_T > 25$ GeV. Both of the τs are required to pass the "medium" identification criteria. Similar to the LTT in the $\tau_\ell\tau_{\rm had}$ channel, during the 2016 data-taking campaign, the DTT requires the presence of an additional jet at Level-1 passing a 25 GeV p_T threshold.

For both $\tau_\ell\tau_{had}$ and $\tau_{had}\tau_{had}$ channel, all triggers are run un-pre-scaled. The electrons, muons, and τs reconstructed offline are required to pass the truth-matching to match the triggered objects. Events containing jets but not associated to any real energy deposits are discarded. All events are required to contain at least one primary vertex with at least two associated tracks(with $p_T > 400$ MeV.)

5.2 $\tau_\ell\tau_{had}$ event selection

In the $\tau_\ell\tau_{had}$ channel, event selection that selects event compatible with containing a $l\tau_{had}bb + E_T^{miss}$ final state is applied. Events passing this pre-selection are used for the $\tau_\ell\tau_{\rm had}$ channel BDT later. The selection criteria is listed below:

- SLT events:
  - Exactly one electron passing the 'tight' identification criteria or one muon passing the 'medium' identification criteria (this also includes a requirement that the muon must have $|\eta| < 2.5$), with p_T 1 GeV above the corresponding trigger threshold used in that data-taking period making sure the trigger efficiency is fully turned on.
  - Exactly one hadronic τ with $p_T > 20$ GeV and $|\eta| < 2.3$.
  - At least two jets in the event with $p_T > 45$ (20) GeV for the leading (sub-leading) jet.
- LTT events:
  - Exactly one electron passing the 'tight' identification criteria and with $p_T >$ 18 GeV, or one muon passing the 'medium' identification criteria with p_T > 15 GeV. An upper limit on the p_T corresponding to the equivalent SLT thresholds for that data-taking period is applied.
  - Exactly one hadronic τ with $p_T > 30$ GeV and $|\eta| < 2.3$.
  - At least two jets in the event with $p_T > 80$ (20) GeV for the leading (sub-leading) jet. The p_T threshold for the leading jet is due to the requirement of the presence of a jet in the event for the Level-1 trigger.
- No other electrons or muons
- Opposite-sign charge between the τ and the light lepton (e/μ)

- The invariant mass of the di-τ system (calculated using the Missing Mass Calculator (MMC))[63], $m_{\tau\tau}^{MMC} > 60\ GeV$.

5.3 $\tau_{had}\tau_{had}$ event selection

Similar to the $\tau_\ell\tau_{had}$ channel selection criteria, an event selection is also applied to select events compatible with final state $\tau_{had}\tau_{had}bb$+E_T^{miss}. This selection forms the set of events used for the $\tau_{\rm had}\tau_{\rm had}$ channel BDT later. The selection criteria is as below:

- STT events:
  - Exactly two hadronic τs with $|\eta| < 2.5$. The leading τ must have $p_T >$ 100, 140, or 180 GeV for data periods where the trigger p_T threshold are 80, 125, or 160 GeV, respectively. The sub-leading τ is required to have $p_T > 20\ GeV$.
  - At least two jets in the event with $p_T > 45$ (20) GeV for the leading (sub-leading) jet.
- DTT events:
  - Exactly two hadronic τs with $|\eta| < 2.5$. The leading (sub-leading) τ must have $p_T > 40$ (30) GeV.
  - At least two jets in the event with $p_T > 80$ (20) GeV for the leading (sub-leading) jet. The p_T threshold for the leading jet is due to the Level-1 trigger requirement of the extra jet presence. For events collected during year 2015 (and an equivalent portion of the MC) the leading jet p_T threshold is 45 GeV since there is no Level-1 jet requirement in the triggers.
- The two τs must have opposite-sign charge.

- The $m_{\tau\tau}^{MMC}$ must be $> 60\ GeV$.

- Events containing electrons or muons are vetoed.

For both $\tau_\ell\tau_{had}$ and $\tau_{had}\tau_{had}$ channels, different event categories are split according to the multiplicity of b-tagged jets. The events with exactly two b-tagged jets are used as signal region for BDT. Events with zero or one b-tagged jet are used as control regions for background estimation and validation. For one b-tagged events, the b-tagged jet and the other highest p_T jet are considered. For zero b-tagged events, the two highest p_T jets are used.

5.4 Boosted decision tree training

Boosted decision trees(BDTs) are used in this analysis to discriminate the signals from background processes instead of using different cuts on the kinematic distributions of the events. Decision tree[21] is a kind of machine learning algorithm which could be used for both classification and regression problems. The decision tree used in this data analysis is the C.A.R.T decision tree [21] which uses the Gini Index to justify the attributes with the greatest separation power. The decision tree will finally form a tree structured classification machine containing layers of decision nodes and leaf nodes. For every decision node, the attribute which will give the smallest Gini Index is chosen. As all the kinematic distributions in the events are continuous, so that we will use the binary partition technique to find the working point for the decision nodes. This also means that the attributes we choose could be used for many times when forming the decision tree, unlike the categorical attributes which we could only use once when forming the decision trees. Boosting here refers to AdaBoost [71], which is a kind of ensemble learning algorithm, combining individual learner (Here, it's the decision tree. As decision tree is the only kind of learner we are going to use, it will also be called base learner) to give better performance and prevent over-fitting.

The AdaBoost algorithm will use the classification result of last round from the base learner to adjust the corresponding weight of events in the training samples. All the events in the training samples have equal weights for the first round training using decision tree. Then after the first round, the wrongly classified events will get larger event weight to get more attention from the base learner, while the events classified in the right category will get a smaller weight. The process goes on until we have got enough number of trees. Then we combine results from all the trees to do an average or voting to get the right classification. The number of trees is one of the tuning parameters we have to tune later in order to gain the best performance of the BDT algorithms. There are also other tuning parameters involved when setting up the BDT, they are listed in Table 5.1. *MaxDepth* and *NinNodeSize* are the two stopping rules for the decision trees. *Ncuts* is the step length for the attributes when doing training. You can think this as 0.01 if we do renormalization for each individual to make the range be [0,1]. The *AdaBoostBeta* is one factor in the weight for each base learner. It will control the learning speed of the BDT algorithm. All the values of these parameters are tuned and studied to achieve the best classification performance.

BDT parameter	Value
BoostType	AdaBoost
AdaBoostBeta	0.15
NTrees	200
MaxDepth	4
MinNodeSize	5%
NCuts	100

Table 5.1: Tuned parameters used for BDT training in both $\tau_{\text{had}}\tau_{\text{had}}$ and $\tau_{\ell}\tau_{\text{had}}$ channels.

The variables with the best separation power between signals and backgrounds are used as the BDT input variables. Different variables are used for different sub-channels which is as expected because of different particle composition and kinematic

distributions in sub-channels. These variables are selected by choosing the highest ranked variables with removal of the highly correlated ones. Definitions of the variables used are listed below:

- m_{hh}: The invariant mass of the di-Higgs system which is reconstructed from the di-tau and di-b-jet masses. Scale factors of $m_{\mathrm{h}}\ /m_{\tau\tau}^{MMC}$ and m_{h}/m_{bb} (where m_{h} is the value of the Higgs boson mass used in the simulation, 125 GeV) are applied to the four-momenta of the di-tau and di-b-jet systems, respectively, in order to improve the mass resolution.

- $m_{\tau\tau}^{MMC}$:The invariant mass of the di-tau system, calculated using the MMC algorithm.

- m_{bb}: The invariant mass of the di-b-jet system.

- $\Delta R(\tau,\tau)$: The ΔR between the visible τs decay products.

- $\Delta R(b,b)$: The ΔR between the two b-jets.

- E_T^{miss}: The missing transverse momentum of the event

- E_T^{miss} ϕ centrality: This variable quantifies the position in ϕ of the E_T^{miss} with respect to the visible decay products of the two τs. It is defined as:

$$E_T^{miss}\phi \text{ centrality} = \frac{A+B}{\sqrt{A^2+B^2}}, \tag{5.1}$$

where A and B are given by:

$$A = \frac{\sin(\phi_{E_T^{miss}} - \phi_{\tau_2})}{\sin(\phi_{\tau_1} - \phi_{\tau_2})},\ B = \frac{\sin(\phi_{\tau_1} - \phi_{E_T^{miss}})}{\sin(\phi_{\tau_1} - \phi_{\tau_2})}. \tag{5.2}$$

The E_T^{miss} ϕ centrality is equal to:

- $\sqrt{2}$ when the E_T^{miss} lies exactly between the two τs; or

- 1 if the E_T^{miss} is perfectly aligned with either of the τs; or
- < 1 if the E_T^{miss} lies outside of the ϕ angular region defined by the two τs.

Signal events tend to have larger values of the E_T^{miss} centrality as in these cases the two τs are produced from the decay of a Higgs boson and the reconstructed E_T^{miss} ϕ angle generally falls in between the two visible τ decay products.

- m_T^W: The transverse mass between the lepton and the E_T^{miss} is defined as:

$$m_T^W = \sqrt{2p_T^\ell E_T^{miss}(1 - \cos\Delta\phi)}, \tag{5.3}$$

where p_T^ℓ is the transverse momentum of the lepton. Signal events tend to have a lower m_T^W than the $t\bar{t}$ process because the transverse mass of a lepton and neutrino decaying from a W boson in a $t\bar{t}$ event tends to peak at $m_W \approx 80$ GeV.

- $\Delta\phi(h,h)$: The $\Delta\phi$ angle between the two reconstructed 125 GeV Higgs bosons, where the di-tau direction is taken from the MMC fit.

- $\Delta p_T(\ell,\tau)$: The difference in p_T between the light lepton and the visible hadronic tau decay products. This variable exploits the imbalance in p_T in the visible decay products caused by the different number of neutrinos accompanying leptonic and hadronic tau decays.

- Sub-leading b-jet p_T.

BDT trainings are done with the MC samples weighted by their predicted cross-sections to separate the signal from the expected backgrounds. Events from signals and backgrounds are first required to pass their respective selection criteria with 2 b-tagged jets. In the $\tau_\ell\tau_{had}$ channel, since the $t\bar{t}$ is the only dominant background in the signal region, the BDT training on signals is performed against it only. Both the

real(real τ decays) and fake($t\bar{t}$ decays with jet mis-identified as τ) τ components in $t\bar{t}$ are taken from MC simulation when training the BDTs in $\tau_\ell\tau_{\text{had}}$ channel. The BDTs for the $\tau_{had}\tau_{had}$ channel are trained against the three major backgrounds, as none of them is dominant. The three dominant backgrounds in the $\tau_{had}\tau_{had}$ signal region are $t\bar{t}$, multi-jet background and the $Z \to \tau\tau + Heavy\ Flavor\ jets$. The template and normalization are derived as described in Chapter **??**. Separate BDTs are trained for each mass point in every probing model and for the non-resonant di-Higgs production model.(2HDM resonant signals, RSG resonant signals, Non-resonant di-Higgs SM signals). A signal injection test demonstrated that training BDTs against single mass point signal samples led to m_{hh} resolution to be as small as 12 GeV for lower resonance masses. This resolution is far less than our resonant signal gaps at low resonance masses(50 GeV). Thus there is a chance that a signal might be missing in between two MC signals. In order not to miss a signals falling between two MC signal samples, each target mass is trained using its neighboring mass points in addition to the central mass value(i.e. The BDT trained for 300 GeV will be trained on the signal samples with $m_{H,G}$ = 275, 300 and 325 GeV). When doing the training, the neighboring signal mass points are both normalized to the cross-section of the central mass point.

The Kolmogorov-Smirnov(KS) test [72] is used to check and make sure the BDTs are not over-fitted. The training and application are k-folded(k=2) depending on event numbers to ensure they are statistical independent. Two trainings are performed for each BDT classifier: one training is done on even event number events and applied to odd event number events to validate and use, the other one is done on odd event number events and applied to even event number events.

For resonant di-Higgs searches, the BDT input variables cover all resonance masses, however, BDT input variables for non-resonant di-Higgs search and LTT category in the $\tau_\ell\tau_{had}$ channel are optimized for the low mass region. Similar sets of input vari-

ables are used for the $\tau_{had}\tau_{had}$ channel and LTT category. Table 5.2 lists all the variables used for $\tau_\ell\tau_{had}$ and $\tau_{had}\tau_{had}$.

Variable	$\tau_\ell\tau_{had}$ channel (SLT resonant)	$\tau_\ell\tau_{had}$ channel (SLT non-resonant & LTT)	$\tau_\ell\tau_{had}$ channel
m_{hh}	✓	✓	✓
$m_{\tau\tau}^{MMC}$	✓	✓	✓
m_{bb}	✓	✓	✓
$\Delta R(\tau,\tau)$	✓	✓	✓
$\Delta R(b,b)$	✓	✓	✓
E_T^{miss}	✓		
E_T^{miss} ϕ Centrality	✓		✓
m_T^W	✓	✓	
$\Delta\phi(h,h)$	✓		
$\Delta p_T(\ell,\tau)$	✓		
Sub-leading b-jet p_T	✓		

Table 5.2: Variables used as inputs to the BDTs for the different channels and signal models.

Fig 5.1 shows the distributions of all the BDT input variables used in SLT channels after the background estimations and full fitting procedures. Fig 5.2 are the BDT input variable plots used in LTT and Fig 5.3 are the BDT input distributions used in $\tau_{\rm had}\tau_{\rm had}$ channel. The plots are all in log-scale with different background processes stacked on each other. The red solid lines are the different corresponding signals in each plot. The background processes stacked in are either from Monte Carlo simulations or data-driven estimations. Details about backgrounds will be covered in Chapter VI and Chapter VII.

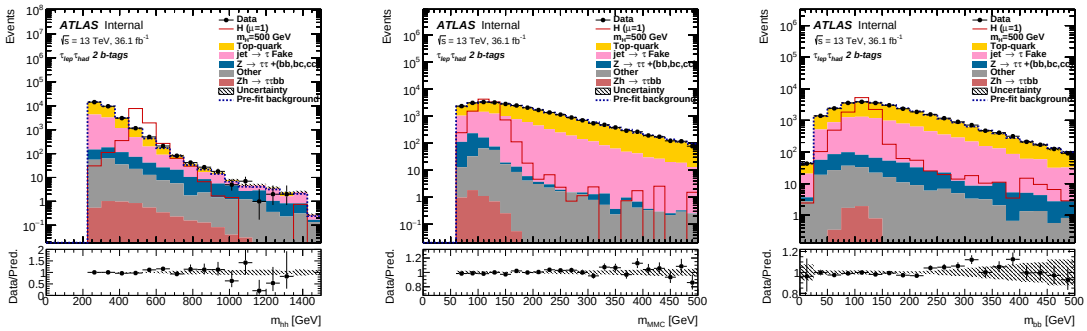

(a) m_{hh}

(b) $m_{\tau\tau}^{\mathrm{MMC}}$

(c) m_{bb}

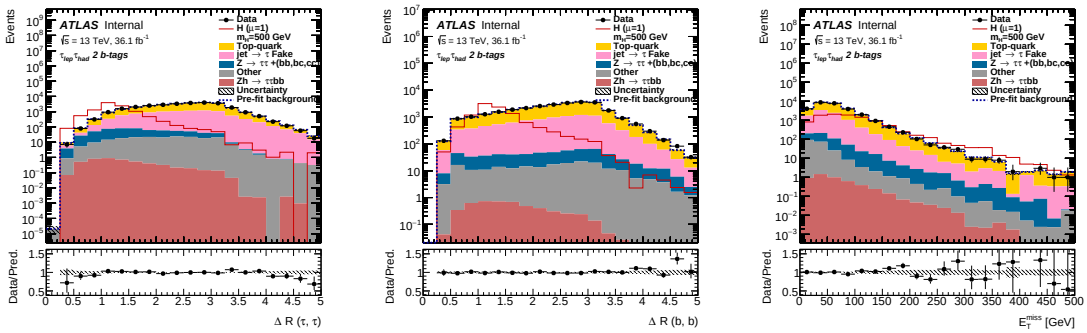

(d) $\Delta R(\tau,\tau)$ (e) $\Delta R(b,b)$ (f) $E_{\mathrm{T}}^{\mathrm{miss}}$

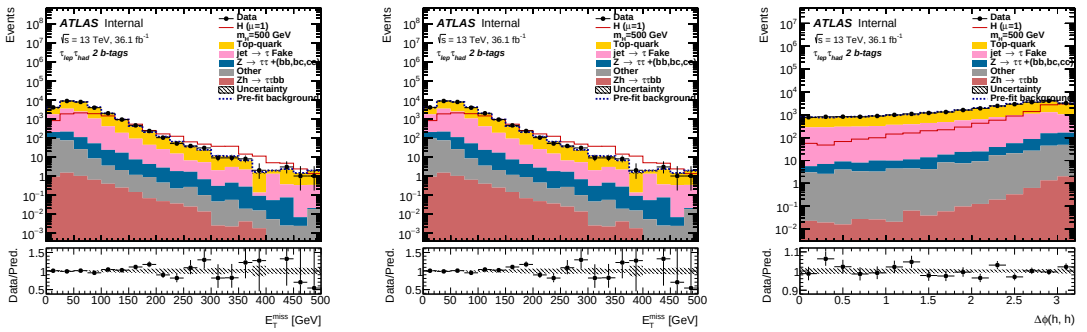

(g) $E_{\mathrm{T}}^{\mathrm{miss}}\phi$ Centrality (h) m_{T}^{W} (i) $\Delta\phi(\mathrm{h},\mathrm{h})$

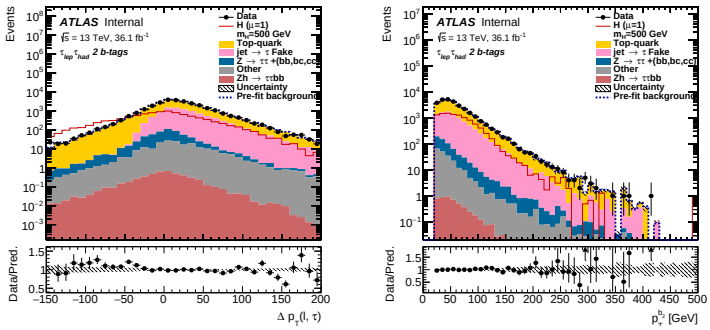

(j) $\Delta p_{\mathrm{T}}(\ell,\tau)$ (k) Sub-leading b-jet p_{T}

Figure 5.1: Distributions of input variables used in the $\tau_\ell\tau_{\mathrm{had}}$ channel BDT (SLT resonant category) after performing the full fitting procedure described in Chapter X and assuming the background-only hypothesis. The 500 GeV 2HDM signal is also shown.

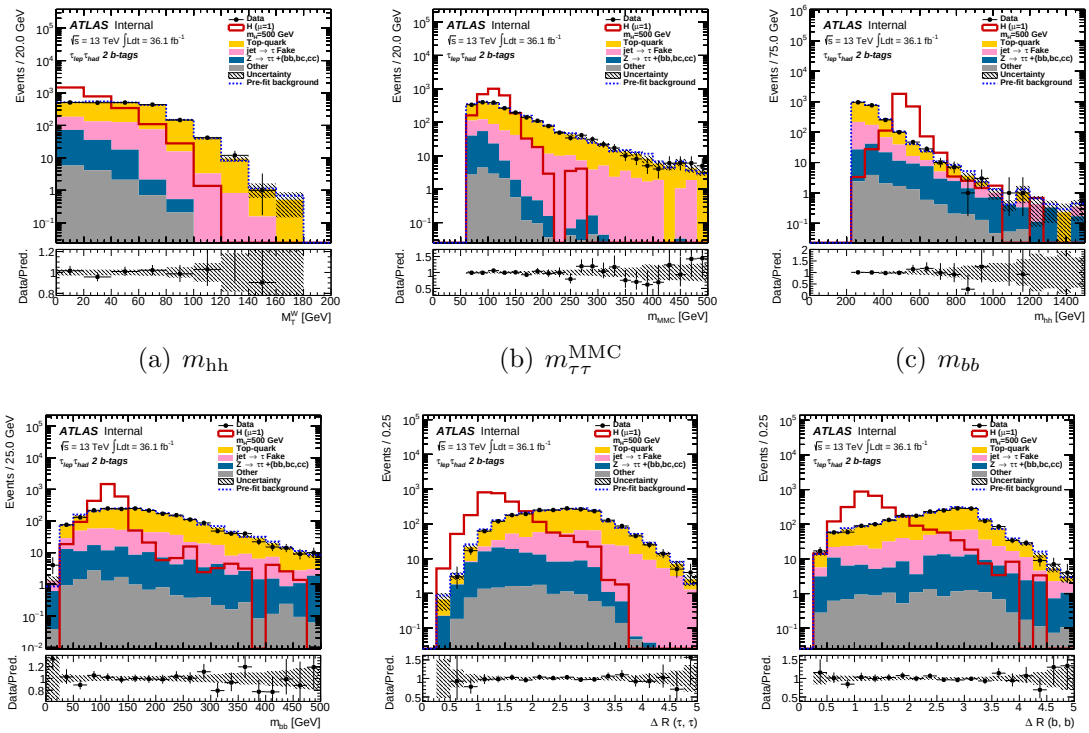

(a) m_{hh} (b) $m_{\tau\tau}^{\mathrm{MMC}}$ (c) m_{bb}

(d) $\Delta R(\tau,\tau)$ (e) $\Delta R(b,b)$ (f) m_{T}^{W}

Figure 5.2: Distributions of input variables used in the $\tau_\ell\tau_{\mathrm{had}}$ channel BDT (LTT channel) after performing the full fitting procedure described in Chapter X and assuming the background-only hypothesis.The 500 GeV 2HDM signal is also shown. The same set of input variables is also used for the non-resonant search in the SLT channel.

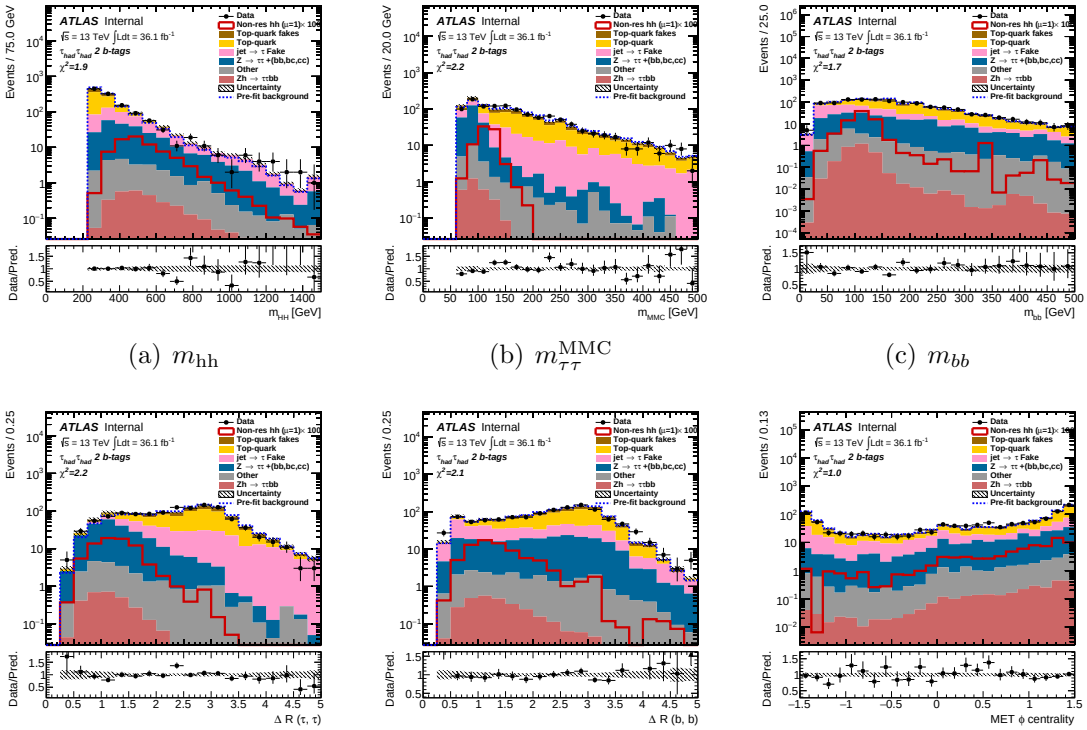

(a) m_{hh} (b) $m_{\tau\tau}^{\mathrm{MMC}}$ (c) m_{bb}

(d) $\Delta R(\tau, \tau)$ (e) $\Delta R(b, b)$ (f) $E_{\mathrm{T}}^{\mathrm{miss}}\phi$ Centrality

Figure 5.3: Distributions of input variables used in the $\tau_{\mathrm{had}}\tau_{\mathrm{had}}$ channel BDT, after performing the full fitting procedure described in Chapter X and assuming the background-only hypothesis.

CHAPTER VI

Data and Monte Carlo Samples

Data is the root of the physics data analysis. Whatever methods used to analyze the data are just as different tools to fetch water from a spring, whether it's a bowl, a bucket, or a plate. While the data is the source of the spring. Thus, it's very important to process data in an efficient and correct way. Monte Carlo simulations are like a well people dig. We could get water from it too. We could use Monte Carlo to simulate the particle collisions and get the same format of output as the real data, however we have to generate them in the proper way and normalize them to the proper amount.

6.1 Data

The LHC provides collisions at a rate of 40MHz, which will be reduced to 100 kHz by the L1 trigger system, then 1 kHz by the high level trigger system of ATLAS [1]. This 1 kHz main physics data stream together with other lower rate physics stream or calibration streams for various subsystems are processed by Athena framework at the ATLAS Tier-0 computing facility. The data preparation is the first stage for physics analysis and produces the primary physics analysis format, the Analysis Object Data (AOD), with calibrations derived in a Prompt Calibration Loop (PCL) running at the Tier-0 computing facility. Furthermore, data preparation also provides

the data quality (DQ) assessment and the luminosity measurement. The data quality assessment is made at several levels during the data preparation work flows. DQ Monitoring(DQM) infrastructure is responsible for the DQ assessment for physics analysis. The DQ problems are summarized in a database down to a granularity of single luminosity block(which is around 1 minute) by the DQ experts at CERN. The global DQ assessment later combines all various DQ problem with logic determined by the Data Quality group to produce the good run list(GRL) for physics analysis. The GRL is directly applied by physicists to exclude data that does not pass the DQ criteria. The AOD from PCL are passed to the ATLAS Derivation Framework to produce a vastly reduced version of the AOD, which we call DAOD. Physicists use DAOD in conjunction with the GRL to process the data and produce final physics result for publications.[73]

The result presented here are based on proton-proton collision data at a center-of-mass energy of$\sqrt{s} = 13\ TeV$, collected by the ATLAS detector at the LHC during year 2015 and 2016. The data used is with an integrated luminosity of 36.1 fb^{-1}. Selected data events are required to have all relevant components of ATLAS detector in good condition. Two good run lists(GRL) are used corresponding separately to 2015 and 2016 data, with luminosity 3.2 fb^{-1} in year 2015 and 32.9 fb^{-1} in year 2016.

Events that cause error or with triggers not being able to process in the online reconstruction are redirected to the 'debug stream'. 7 Events in the 'debug stream' in the $\tau_{lep}\tau_{had}$ channel passed the CxAODMaker pre-selection criteria. 1 out of 7 events passes the SLT event selection, but has zero b-tagged jets and a BDT score of -0.5. There is no event passing the LTT or $\tau_{had}\tau_{had}$ channel selection criteria.

6.2 Monte Carlo samples

Monte Carlo simulations are widely used in the high energy experiment data analysis, including ATLAS experiment [74]. Physicists use Monte Carlo samples to sim-

ulate the collisions between particles. Specifically, Monte Carlo samples are used to simulate the background process which is to the signals of interest as well as the cross section and topology of the predicted theoretical phenomena in signals. The process of generating Monte Carlo simulation samples generally contains two steps. Firstly, various of Monte Carlo generators are used to generate different particle collision and decay processes, including both background and signal processes, with truth information attached. Secondly, all the processes produced using generators are passed to GEANT4[75, 74] detector simulation framework to simulate their interactions with the ATLAS detector. The Monte Carlo simulations coming out from the detector simulation will go through exactly the same data processing framework as the real data and end up with the same format as the actual data. Fig. 6.1 shows a comparison between the processing paths of the actual data and the Monte Carlo simulation samples.

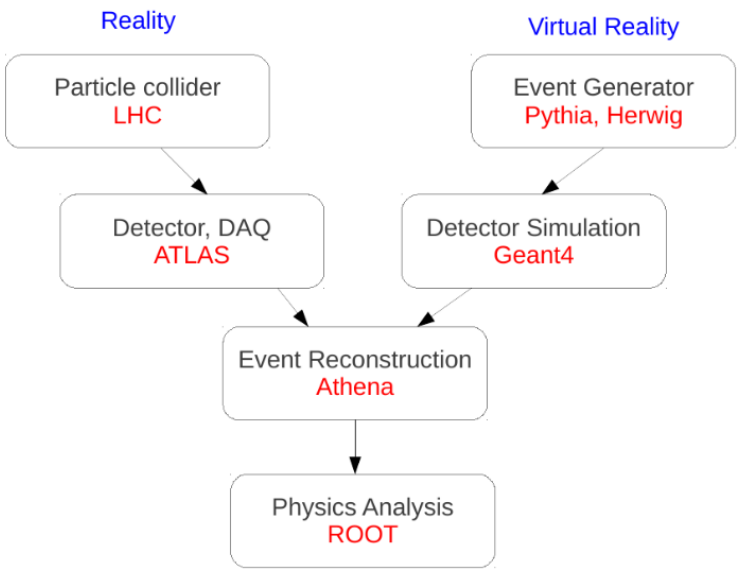

Figure 6.1: A schematic illustration of data processing procedures of the Monte Carlo simulations and real data on ATLAS

The signal samples for resonant di-Higgs production in the extended Higgs sector of Two-Higgs-Doublet Models(2HDM)[6] and the bulk Randall-Sundrum(RS)

model[3, 4, 5] in extra dimensions were produced for 14 different mass points(260, 275, 300,325, 350,400,450,500,550,600,700,800,900,1000 GeV). Only the gluon-fusion produced resonant signals are considered in this analysis. The 2HDM model di-Higgs signals are generated in MadGraph5 at leading-order(LO)[76] and showered using Pythia 8.186 [77]. A14 tune [78] is used together with the NNPDF2.3LO parton distribution function(PDF) set [79]. The decay products, SM Higgs boson mass, m_h is fixed to be 125.0 GeV. The width of the heavy scalar, H, is set to be 4 MeV. The graviton signal G^*_{KK} events are produced with different values of the coupling constant $c = k/\bar{M}_{PI}$ (1.0, 2.0). The k is the curvature of the warped extra dimension and $\bar{M}_{PI}$ is the effective four-dimensional Planck scale equaling to 2.4×10^{18} GeV. The coupling constant c will decide the cross section and natural width of the RSG signals. The resonance width is 55/220 GeV for $c = 1.0/2.0$ assuming a graviton mass of 1 TeV. The $c = 2.0$ samples have a wider width and are used to study broader resonances.

Non-resonant di-Higgs signals assume a Higgs boson mass of 125.09 GeV. The Standard Model production diagrams are simulated using an effective field theory(EFT) model that includes finite top mass correction through form factors. The signals are generated using MG5_aMCNLO v2.2.2 at next-to-leading-order(NLO)[80] and interfaced to the Herwig++ [81] parton shower and hadronization model. UEEE5 tune with CTEQ6L1 PDF set are used. Another set of signals are generated by reweigting the non-resonant signals to account for the effects of taking into account the full top-quark mass dependence[18, 82].

For the generation of $t\bar{t}$ and single top-quarks in the Wt and s-channel, the Powheg-Box v2 generator [83] with the CT10 PDF sets in the matrix element calculations are used. The electroweak t-channel single top-quark events are generated using the Powheg-Box v1 generator. The Powheg generator uses the 4-flavor scheme for the NLO matrix elements calculations together with the fixed four-flavor PDF

set CT10f4. Top-quark spin correlations are preserved for all the top processes. The parton shower, fragmentation, and the underlying events are simulated using Pythia 6.428[84] with the CTEQ6L1 PDF sets and the corresponding Perugia 2012 tune(P2012)[85]. The top-quark mass in all the processes is set to be 172.5 GeV. The bottom and charm hadron decays are modeled using the EvtGen v1.2.0 program[86]. $t\bar{t}$ production cross section is calculated at NNLO+NNLL[87], while for single top processes, the generator NLO cross sections are used.

Events containing W or Z bosons with associated jets are simulated using the Sherpa 2.2.1 generator[88]. Matrix elements are calculated for up to 2 partons at NLO and 4 partons at LO using the Comix[89] and OpenLoops[90] matrix element generators and merged with the Sherpa parton shower[91] using the ME+PS@NLO prescription[92]. The CT10NLO PDF set is used in conjunction with dedicated parton shower tuning developed by the Sherpa authors. All W/Z+$Jets$ events are normalized to the predicted cross sections using NNLO calculations.

Di-boson processes with one of the bosons decaying hadronically and the other leptonically are simulated using the Sherpa 2.1.1 generator[88]. They are calculated for up to one (ZZ) or zero (WW, WZ) additional partons at NLO and up to three additional partons at LO. The CT10 PDF set is used in conjunction with dedicated parton shower tuning developed by the Sherpa authors. The generator NLO cross sections are used.

Standard Model Higgs production in association with a Z boson, subsequently decaying to a $bb\tau\tau$ final state is an irreducible background to this analysis. The $qqZh(Z \to \tau\tau, h \to bb)$ and $qqZh(Z \to bb, h \to \tau\tau)$ processes are generated with Pythia 8.186[84], using the A14 tune and NNPDF23LO PDF set. The gluon-fusion initiated $Zh(Z \to \tau\tau, h \to bb)$ process is generated with Powheg-Box v2[93] using the CT10 PDF sets. The parton shower, fragmentation, and the underlying events are simulated using Pythia 8.186[84] . The AZNLO tune[94] is used, with PDF

set CTEQ6L1, for the modelling of non-perturbative effects. The cross section of the $qqZh(Z \to bb, h \to \tau\tau)$ process is scaled up by 6% in order to account for its gluon-fusion initiated counterpart, due to difficulties in modelling the gluon-fusion component. For all ZH processes, the EvtGen v1.2.0 program[86] is used to model properties of the bottom and charm hadron decays. Other SM Higgs boson processes are checked and found to be negligible.

The complete list of names of Monte Carlo simulation samples, including both signals and backgrounds, is attached in the Appendix with corresponding cross sections and filter efficiency.

CHAPTER VII

Background Estimation

The Confucius once said "While you don't yet understand life, how can you understand about death?". While we don't know the known, how can we understand the unknown? We have to make sure we understand the known at the first place if we want to explore the unknown.

Similarly, the background estimation plays a very critical role in the data analysis. In order to search for new physics or new particles using the LHC data, we have to understand the known processes first, in other words, we have to model the processes already known to us very well. We are able to find new processes only after we have a very good understanding of the processes in the Standard Model.

In both channels, the background processes containing real τ lepton decays are taken from MC simulations. The dominant background processes – $t\bar{t}$ and $Z/\gamma^* \to \tau\tau$ produced with the heavy flavor (bb, bc, cc) – will be normalized with the final fit to the control region. Backgrounds with the reconstructed hadronic τ faking by jets are estimated using the data driven methods. In both $\tau_\ell\tau_{\rm had}$ and $\tau_{\rm had}\tau_{\rm had}$ channels, $t\bar{t}$ events with one or more reconstructed hadronic τ decays mis-reconstructed by jets(so called fake-τs) are estimated separately from data. In the $\tau_\ell\tau_{\rm had}$ channel, all the fake-τ background from $t\bar{t}$, W+jets, multi-jet are estimated using an inclusive fake-factor method at the same time. In the $\tau_{\rm had}\tau_{\rm had}$ channel, the fake-τ $t\bar{t}$ background is

estimated from data by measuring the Fake Rate(probability for a jet from a hadronic W boson decay to be reconstructed as a hadronic τ), which is then used to correct the MC simulation.

After the background estimation, the background modeling are compared with data in 0,1 and 2 b-tag regions after the pre-selection described in Chapter V. We found in both $\tau_\ell\tau_{\rm had}$ and $\tau_{\rm had}\tau_{\rm had}$ channels, the background modelings are in good agreement with data and work as desired.

7.1 $t\bar{t}$ with true hadronic τ decays

In both $\tau_\ell\tau_{\rm had}$ and $\tau_{\rm had}\tau_{\rm had}$ channels, the $t\bar{t}$ background with true hadronic τ decays is estimated using Monte Carlo simulations. The normalization of true τ $t\bar{t}$ background is determined in the final fit. The normalization scale factor is mostly dominated by the low-score region in the $\tau_\ell\tau_{\rm had}$ BDT distribution where the true τ $t\bar{t}$ are the dominant background. The normalization between the $\tau_\ell\tau_{\rm had}$ and the $\tau_{\rm had}\tau_{\rm had}$ channels can only differ within an acceptance uncertainty. A normalization factor of 1.00 ± 0.12 is obtained overall, with the $\tau_{\rm had}\tau_{\rm had}$ channel varied down by 18%.

7.2 Fake τ background estimation in the $\tau_\ell\tau_{\rm had}$ channel

In the $\tau_\ell\tau_{\rm had}$ channel, the major source of the backgrounds where reconstructed hadronic τs are faked by jets(fake τ background) are $t\bar{t}$, W+jets and multi-jet background. We use the so called "combined fake factor" method to estimate the fake τ background all at once in the $\tau_\ell\tau_{\rm had}$ channel, for both SLT and LTT events[95]. Because of the correlation between the three sources of fake-τ background, we are unable to estimate them one by one in series. The τ "fake-factor" is used to weight the fake-τ events in the control region to get the right modeling of the corresponding background in the signal region(SR). Due to different kinematic distributions between

SLT and LTT categories, the τ fake-factors have to be calculated separately for SLT and LTT events.

In the 2 b-tag signal region, the dominant source of the fake τ background is $t\bar{t}$ (with fake τ decays, while some $t\bar{t}$ decays to real τs). Small contributions of fake τ background also come from multi-jet, single top, and W+$Jets$ processes. In the 0 b-tag control region, the dominant source of the fake τ background is W+$Jets$ events. However, in the 1 b-tag control region, either of the $t\bar{t}$ and W+$Jets$ backgrounds dominates roughly 50% percent of total fake τ background. The τ fake factors are measured regardless of $\tau_{\mathrm{e}}\tau_{\mathrm{had}}$ or $\tau_{\mu}\tau_{\mathrm{had}}$ channel because we know that the jet faking τ rate should be independent from the charged lepton flavor in principle. This is verified by comparing the τ fake factor from $\tau_{\mathrm{e}}\tau_{\mathrm{had}}$ and $\tau_{\mu}\tau_{\mathrm{had}}$ channels. We found there is no significant difference between the τ fake factors calculated from $\tau_{\mathrm{e}}\tau_{\mathrm{had}}$ and $\tau_{\mu}\tau_{\mathrm{had}}$ channels. The τ fake factors(FF) are calculated separately for each process($t\bar{t}$, W+$Jets$, multi-jet) in their corresponding control regions for 1-prong and 3-prong hadronic τ decays. The control region for each process makes that certain background absolutely dominant. The τ fake factors are parameterized on τ p_{T} eventually and applied on τ p_{T} to get the distributions in the signal region.

The control region definitions for $t\bar{t}$, W+jets, and multi-jet background are as below:

- $t\bar{t}$: $m_{\mathrm{T}} > 40$ GeV, in 2 b-tags region
- W+$Jets$: $m_{\mathrm{T}} > 40$ GeV, in 0 b-tags region
- Multi-jet : inverted lepton isolation requirements ("tight" electrons and "medium" muons are required to fail their respective "loose" isolation working points), in 0 or 1 b-tag regions

The fake τ enriched sample is defined by applying the pre-selection defined in Chapter V, but requiring the hadronic τ criteria replaced by the "anti-τ" requirement.

We require "Medium" τ ID in the signal region, while in the fake τ region, we require it to fail "Medium" τ ID but with a BDT score > 0.35. In the case where the event contains more than one anti-τ, one is chosen randomly. The τ fake factors are defined using the equation below:

$$FF = \frac{N(\tau)}{N(\text{anti}-\tau)} \tag{7.1}$$

Fig 7.1 shows the fake factors used to calculate the combined fake factor in the SLT sub-channels. In Fig 7.2 and Fig 7.3, the fake factors in LTT sub-channel are showed in $\tau_{\text{e}}\tau_{\text{had}}$ and $\tau_{\mu}\tau_{\text{had}}$ categories respectively. As there are no significant difference between the fake factors in $\tau_{\text{e}}\tau_{\text{had}}$ and $\tau_{\mu}\tau_{\text{had}}$ categories, we use inclusive fake factors in LTT sub-channel.

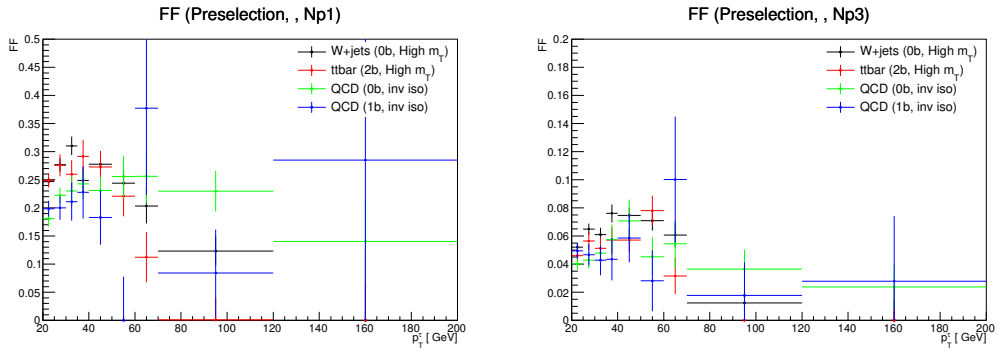

Figure 7.1: Fake factors for 1-prong (left) and 3-prong (right) τs for W+$Jets$ in the 0 b-tag region, $t\bar{t}$ in the 2 b-tag region, and multi-jet processes in the 0 and 1 b-tag regions for the $\tau_{\ell}\tau_{\text{had}}$ channel (SLT category).

As described before, the fake factors are calculated for 1-prong and 3-prong hadronic τ decays separately. The combined fake factor is then calculated using the individual fake factors for different processes ($t\bar{t}$, W+jets, multi-jet) by applying corresponding component fractional ratios. The combined FF is applied to the fake τ control region (full signal selection with τ ID failed, BDT score > 0.35) to model the correct normalization and shape of the fake τ background in signal region. The

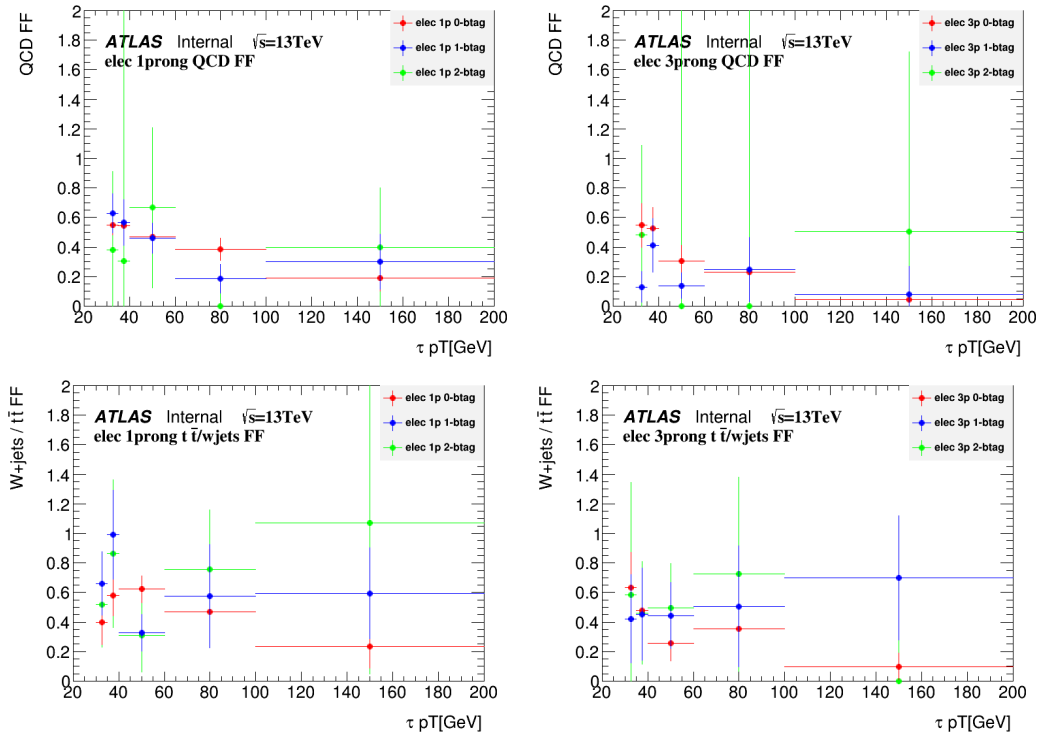

Figure 7.2: Fake factors for 1-prong (left) and 3-prong (right) τs for multi-jet (top) and $W+Jets/t\bar{t}$ (bottom) for the $e\tau_{\mathrm{h}}$ channel (LTT category). For the $W+Jets/t\bar{t}$ plots, the 0 b-tag region is dominated by $W+Jets$ events and the 2 b-tag region by $t\bar{t}$ events, while the 1 b-tag region is a mixture of the two.

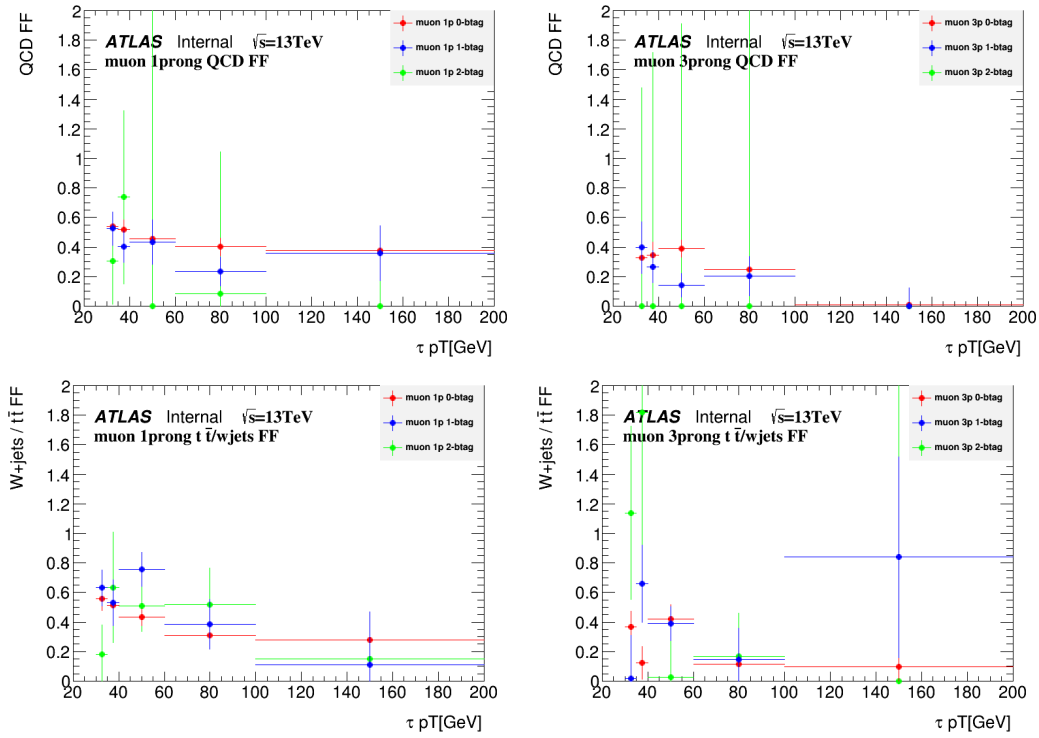

Figure 7.3: Fake factors for 1-prong (left) and 3-prong (right) τs for multi-jet (top) and $W+Jets/t\bar{t}$ (bottom) for the $\mu\tau_{\mathrm{h}}$ channel (LTT category). For the $W+Jets/t\bar{t}$ plots, the 0 b-tag region is dominated by $W+Jets$ events and the 2 b-tag region by $t\bar{t}$ events, while the 1 b-tag region is a mixture of the two.

combined fake factor is defined as:

$$FF(\text{comb}) = FF(\text{QCD}) \times \text{r}_{\text{QCD}} + FF(W/t\bar{t}) \times (1 - \text{r}_{\text{QCD}}) \tag{7.2}$$

Since the 0(2) b-tag region is completely dominated by W+$Jets$ ($t\bar{t}$) events, we will neglect the $t\bar{t}$ (W+$Jets$) when calculating the combined fake factor in this region. This is the reason that in Eq. 7.2 we have FF(W/$t\bar{t}$) for 0 b-tag and 2 b-tag correspondingly. In the 1 b-tag control region, fake factors are defined separately for W+$Jets$ and $t\bar{t}$ processes and the relative contributions are taken using MC predictions. The r_{QCD} is the component percentage of the fake-τ QCD background out of all the fake-τ background. Due to different amount of QCD background fraction in different tag region, the r_{QCD} is computed separately in each tag region.

The r_{QCD} is measured as a function of the τ p_{T} and defined as the fraction of fakes in the anti-τ region coming from multi-jet. It is defined as:

$$\text{r}_{\text{QCD}} = \frac{N(\text{multi} - \text{jet}, \text{data})}{N(\text{data}) - N(\text{true}\,\tau_{\text{had}}, \text{MC})} \tag{7.3}$$

The numerator is calculated by using data to subtract all predicted MC events in the anti-τ region, both fake and true τ background apart from multi-jet as shown in Eq 7.4, while the denominator is calculated by using data to subtract MC predicted background with only true τ_{had} decays.

$$N(\text{multi} - \text{jet}, \text{data}) = N(\text{data}) - N(\text{true}\,\tau_{\text{had}}, \text{MC} + \text{fake}\,\tau_{\text{had}}, \text{MC}). \tag{7.4}$$

The r_{QCD} is also cross checked in the previous run using data driven estimation with the lepton fake factor method. Both of these two methods give almost identical r_{QCD} value. Due to simplicity, we choose to just use the r_{QCD} from the MC prediction. r_{QCD} is calculated for 1-prong and 3-prong hadronic τ decays separately in each tag

region for $\tau_e\tau_{had}$ and $\tau_\mu\tau_{had}$ category events.

Fig 7.4 and 7.5 are the r_{QCD} distribution used when calculating the combined fake factors. The $\tau_e\tau_{had}$ and $\tau_\mu\tau_{had}$ sub channels have different r_{QCD} distributions and we use them separately in the calculation of the combined fake factors.

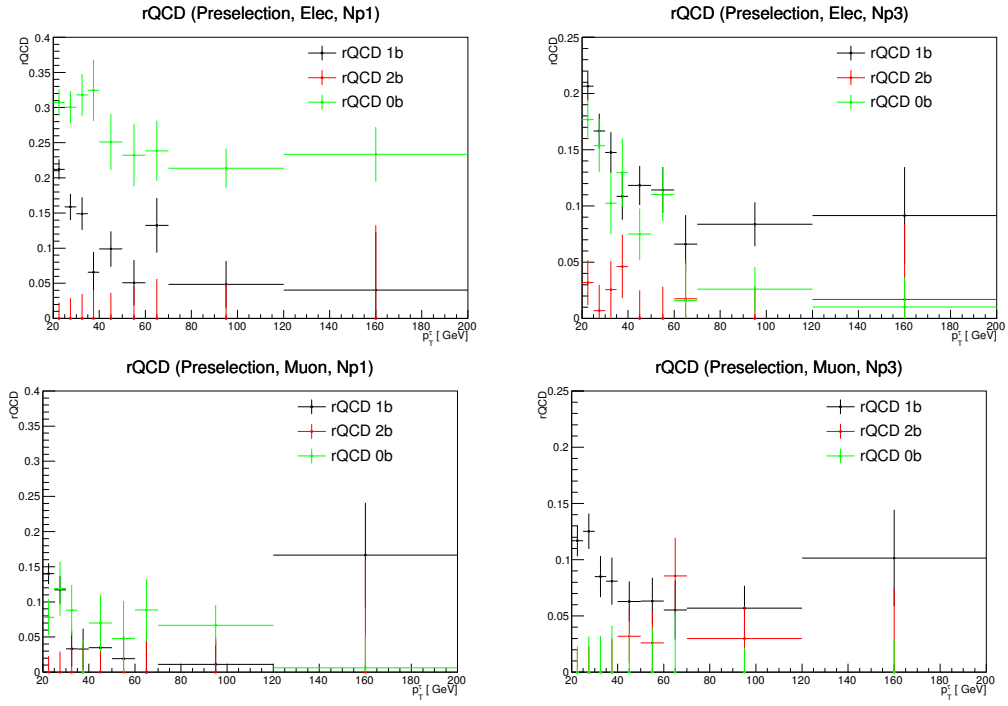

Figure 7.4: r_{QCD} for 1-prong (left) and 3-prong (right) τs for the $e\tau_h$ channel (top) and $\mu\tau_h$ channel (bottom) (SLT category).

Due to the low statistics in LTT category 2 b-tag signal region, the r_{QCD} and FF in this region have extremely large uncertainties. In order to avoid large statistical uncertainties, we use the r_{QCD} and FF calculated from 1 b-tag for the estimation of fake τ background in the 2 b-tag region in LTT category. The validity of the combined fake factor method is cross checked in the same sign control region. The same sign control region is defined as events passing all pre-selection criteria but requiring the hadronic τ and lepton to have the same sign charge. The same sign control region is dominated by the fake τ background. We found good agreement between the data and estimated fake τ background using combined fake factor method in the same sign

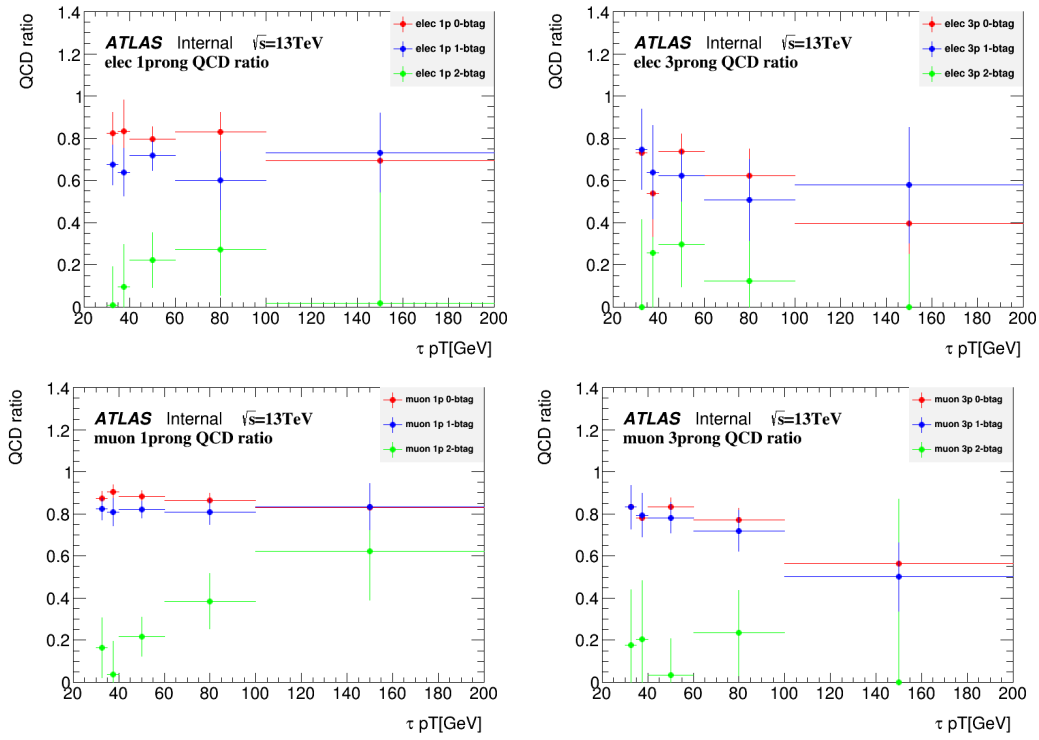

Figure 7.5: r_{QCD} for 1-prong (left) and 3-prong (right) τs for the $e\tau_h$ channel (top) and $\mu\tau_h$ channel (bottom) (LTT category).

control region. When doing the validation of the background estimation in the same sign control region, we used the r_{QCD} and FF derived from the same sign control region instead from the normal opposite sign region.

The possible background processes with jets misidentified as a light lepton(e/μ) are estimated from Monte Carlo simulation because the jet faking lepton rate is well modeled by MC and the discrepancies have a negligible impact on the analysis compared with the impact caused by the jet faking τ rate. Approximately, the jet-to-τ fake rate is 12 times larger than the jet-to-lepton fake rate and with a much larger associated uncertainties.

7.3 $t\bar{t}$ with fake-τ background estimation in the $\tau_{\text{had}}\tau_{\text{had}}$ channel

In the $\tau_{\text{had}}\tau_{\text{had}}$ channel, the $t\bar{t}$ background with one or more jets misidentified as a hadronic τ (fake τ $t\bar{t}$) is simulated with MC and corrected using fake-rates derived from data in a control region because we knew that the $t\bar{t}$ events passing the τ ID in $\tau_{\text{had}}\tau_{\text{had}}$ channel are badly modeled. The control region used to derive the τ fake-rates is defined using the $\tau_{\ell}\tau_{\text{had}}$ channel SLT event pre-selection with transverse mass between the lepton and the $E_{\text{T}}^{\text{miss}}(m_{\text{T}}^{W})$ greater than 80 GeV in the 2 b-tagged region(The $t\bar{t}$ control region in $\tau_{\ell}\tau_{\text{had}}$ channel is with the $m_{\text{T}}^{W} > 40$ GeV), however, without the τ ID requirements applied on the reconstructed τs. The control region is enriched with semi-leptonic $t\bar{t}$ events (ℓ + jet + 2 b-jet + $E_{\text{T}}^{\text{miss}}$ final state) which is used to calculate the fake-rates(FR). The fake rate is defined as the probability of a jet passing the τ ID requirements:

$$FR = \frac{N(\text{pass})}{N(\text{total})} \tag{7.5}$$

The FR is parameterized on τ p_{T} calculated for 1-prong and 3-prong τs separately. The FR is derived inclusively across the $\tau_{\text{e}}\tau_{\text{had}}$ and $\tau_{\mu}\tau_{\text{had}}$ channels to have smaller statistical uncertainty. We are able to do this because we know, in principle, the lepton flavor type should have no effect on the jet faking τ rate. The FR from $\tau_{\text{e}}\tau_{\text{had}}$ and $\tau_{\mu}\tau_{\text{had}}$ are also cross checked and turned out to be within statistical uncertainties. N(total) in Eq. 7.5 is the number of events passing the SLT selection described before but without the "Medium" τ ID requirement(τ-ID BDT > 0.35, !Medium). N(pass) is the subset of the N(total) events with one of the jets passing the offline "Medium" τ ID requirement and the online τ ID. The online τ ID is achieved by requiring the τ to be trigger-matched to the *tau25* trigger. The $t\bar{t}$ with true hadronic τ decays and other Monte Carlo backgrounds are subtracted from the numerator and denominator when

calculating the FR in order to make this FR specifically for fake τ $t\bar{t}$ background. Fig 7.6 illustrates the distribution of the $t\bar{t}$ fake rate used here with respected to τ p_{T}.

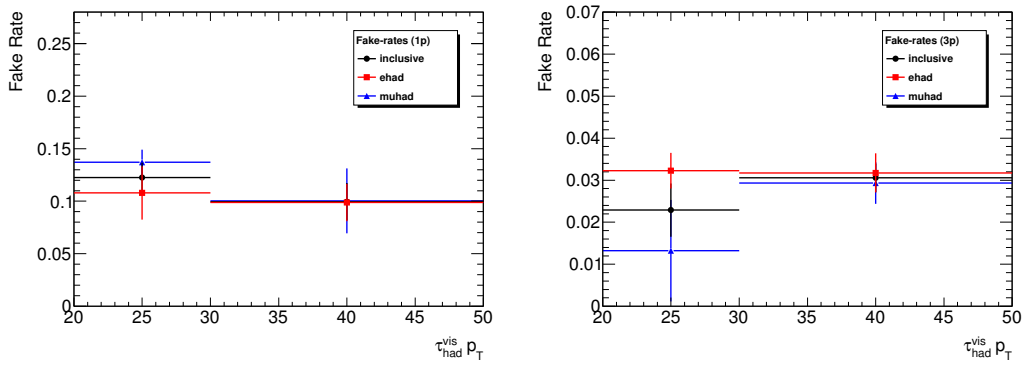

Figure 7.6: Fake rates for one-prong (left) and three-prong (right) τs for the $t\bar{t}$ background estimation procedure in the $\tau_{\mathrm{had}}\tau_{\mathrm{had}}$ channel. The categories 'ehad' and 'muhad' had refer to the semi-leptonic decay modes with $e\tau_{\mathrm{had}}$ and $\mu\tau_{\mathrm{had}}$ final states, respectively.

The τ fake-rates are then applied to fake-τ $t\bar{t}$ events taken from MC that have passed the $\tau_{\mathrm{had}}\tau_{\mathrm{had}}$ channel event pre-selection but have not been required to pass the τ trigger or offline τ ID(tau ID > 0.35) because the τ ID requirements would bias the overall prediction. The DTT p_{T} threshold are applied to these fake-τ $t\bar{t}$ events before applying the τ FR. A p_{T} dependent systematic uncertainty is applied to account for the difference in the p_{T} distribution which would arise from combining the DTT and the STT. The FR is applied to both τs if both of the reconstructed τs are misidentified by jets since we use the FR to correct τs themselves rather than a per-event weight. In the case where both of the τs from $t\bar{t}$ events are real, we will neglect these events here because the prediction of these events are entirely from MC simulation.

7.4 Multi-jet background estimation in the $\tau_{\text{had}}\tau_{\text{had}}$ channel

A data-driven ABCD method is used to estimate the multi-jet background in the $\tau_{\text{had}}\tau_{\text{had}}$ channel. The ABCD method uses two uncorrelated variables to cut out 4 orthogonal regions. One of the 4 regions should be our signal region. We label these 4 regions as region A, region B, region C and region D. Because of the fact that the two variables used to split these four regions are uncorrelated, there will be a proportional relationship between these four regions which could be used to model the distributions in the signal region, as showed in Eq. 7.6.

$$N_D = N_c \times N_A/N_B \tag{7.6}$$

A illustration plot of this methodology is showed in Fig 7.7 as well. The ratio of N_A/N_B in the equation is often called scale factor or fake factor.

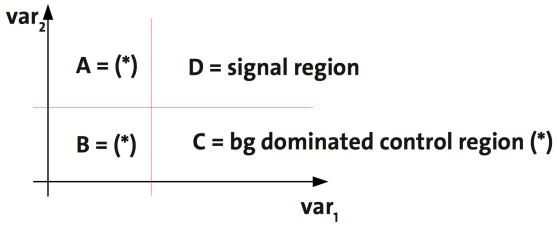

Figure 7.7: A illustration of the general ABCD method

The two control regions used here are a same-sign region(SS) where both of the hadronic τs are required to have same sign charge and anti-τ region, where the hadronic τ is required to fail the τ BDT 'Medium' working point with BDT score $>$ 0.35. The Multi-jet events in the opposite sign(OS) di-τ signal region are modeled with events from the opposite sign anti-τ region, weighted by a fake-factor(FF). The fake-factors are calculated in the SS control region as the ratio of the number of events with both τ candidates to events containing at least one anti-τ. The FF is defined as below in Eq. 7.7:

$$N^{\tau}_{\mathrm{OS},i} = N^{\mathrm{anti}-\tau}_{\mathrm{OS},i} \frac{N^{\tau}_{\mathrm{SS},i}}{N^{\mathrm{anti}-\tau}_{\mathrm{SS},i}}; FF = \frac{N^{\tau}_{\mathrm{SS},i}}{N^{\mathrm{anti}-\tau}_{\mathrm{SS},i}} \tag{7.7}$$

where i represents a bin with certain number of τ decay multiplicity, STT or DTT in $(p_{\mathrm{T}}^{\tau_0}, p_{\mathrm{T}}^{\tau_1})$, and $N^{\tau}_{\mathrm{SS},i}/N^{\mathrm{anti}-\tau}_{\mathrm{SS},i}$ is called the fake factor. These fake factors are shown in Fig 7.8 with projection onto leading τ p_{T} as we know the fake factors used in the formula are two-dimensional.

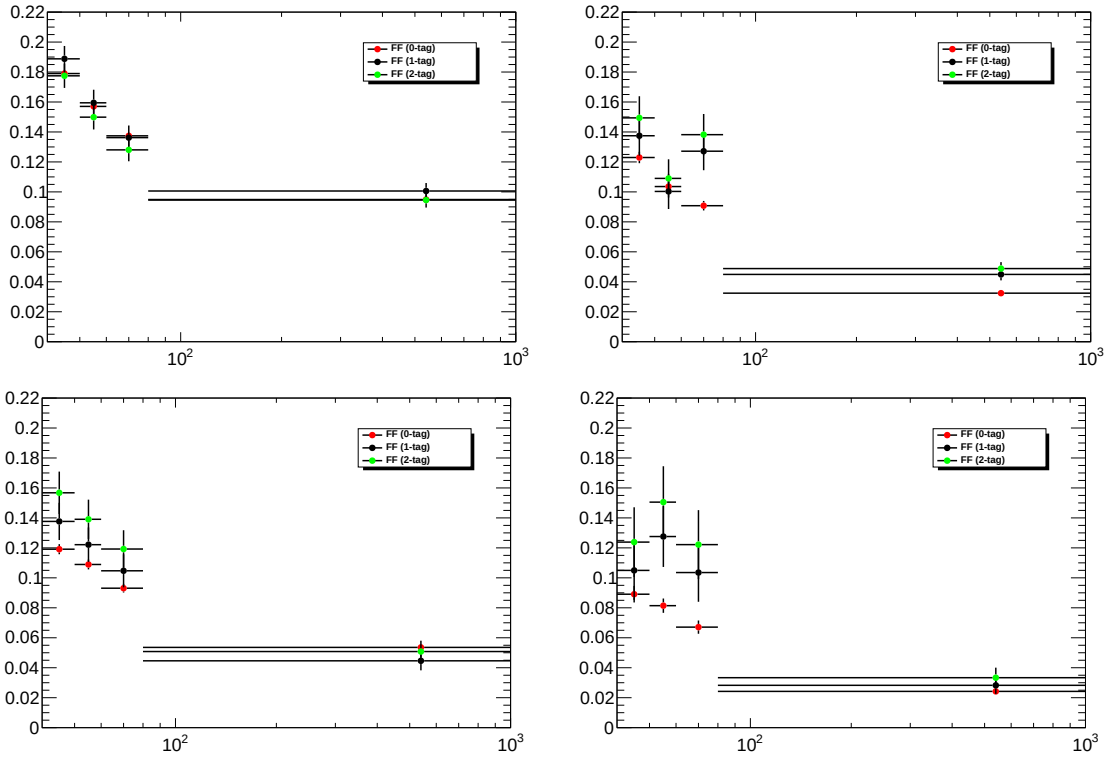

Figure 7.8: Fake factor projections onto the leading τ p_{T} for 1 and 2 b-tag events for τ for 1-prong,1-prong (top left), 1-prong,3-prong (top right), 3,prong,1-prong (bottom left) and 3-prong,3-prong (bottom right) τ pairs in the DTT region, used to determine the multi-jet background in the $\tau_{\mathrm{had}}\tau_{\mathrm{had}}$ channel. (The descriptions are ordered as leading,sub-leading.) The fake-factors are determined in the SS control region and are applied to OS anti-τ events to model multi-jet background in the SR. The fake factors used in the analysis are 2-dimensional, parameterized on the p_{T} of the leading and sub-leading τ.

In the anti-τ control region, one anti-τ may be paired with another anti-τ, or

with a 'Medium' τ candidate (i.e. one passing the nominal τ candidate selection requirements). A random selection is performed if there is more than one possible combination of candidates for pairing. Events with two 'Medium' τ candidates are rejected from the anti-τ selection. The number of events in the SS control region is of the same order of magnitude as in the OS region, while the number of events in the anti-τ control region is an order of magnitude larger than that in the τ candidate region. In each of the regions, the contributions from other background processes (including the fake-τ $t\bar{t}$ background component, which is estimated using a data-driven method in the $\tau_{\text{had}}\tau_{\text{had}}$ channel for BDT inputs variables) are subtracted from the data using MC predictions.

Separate fake-factors are calculated for STT and DTT events, and for 1-prong and 3-prong hadronic τs. Different fake-factors are calculated in the 0, and 1 b-tag regions. The fake factors in the 0 and 1 b-tag regions for DTT events are determined in a two-dimensional grid in bins of $p_{\text{T}}^{\tau_0}$ vs. $p_{\text{T}}^{\tau_1}$. However, the STT and DTT 2 b-tag regions do not have sufficient statistics to allow for the determination of p_{T}-dependent fake-factors. For DTT events, the 2D fake factors from the 1 b-tag region are applied in the 2-tag region, while for STT events, unbinned 1-tag fake-factors(scale factor) are applied in the 2-tag region. A 1-tag to 2-tag transfer-factor is applied in both cases, as shown in Table 7.1. Transfer factor is defined as the ratio between the inclusive fake-factors(single bin) derived in the 1 and 2 b-tag regions for both triggers together but calculated separately for 1-prong 1-prong, 1-prong 3-prong, 3-prong 1-prong, and 3-prong 3-prong events.(Multiplicity of the leading τ decay and multiplicity of the sub-leading τ decay)

7.5 Z+Heavy flavor jets background normalization

The cross-section of the Z boson production in association with heavy flavor jets(b, c) is known to be badly modeled by Monte Carlo simulation. Thus we use

b-tag and prongs	Factor
1Tag1P1P FF	0.141
1Tag1P3P FF	0.0576
1Tag3P1P FF	0.0861
1Tag3P3P FF	0.0449
2Tag1P1P FF	0.136
2Tag1P3P FF	0.0553
2Tag3P1P FF	0.103
2Tag3P3P FF	0.0445

Table 7.1: Inclusive fake-factors (FF) for DTT multi-jet events.

a data-driven method to model this kind of background. As we know the production of the jets is independent of the decay mode of the Z boson, we could choose the $Z \rightarrow \mu\mu$ $+Heavy\ Flavor\ Jets$ control region to derive the scale factor and then generalize it to all Z+$Heavy\ Flavor\ Jets$ background. The advantage of the using the $Z \rightarrow \mu\mu$ $+Heavy\ Flavor\ Jets$ control region is that it provides a high purity sample which is orthogonal to the signal region. The $Z \rightarrow \mu\mu$ $+Heavy\ Flavor\ Jets$ control region is defined as below:

- events passing single muon trigger
- exactly two muons with p_{T}> 27 GeV
- di-muon invariant mass($m_{\mu\mu}$) between 81 GeV and 101 GeV
- two b-tagged jets, leading jet p_{T}> 45 GeV, sub-leading jet p_{T}> 20 GeV
- Higgs mass window veto, $m_{bb} < 80\ GeV$ or $m_{bb} > 140\ GeV$, to remove contamination from SM $VH(H \rightarrow bb)$ process.

The normalization scale factor of the Z+$Heavy\ Flavor\ Jets$ background is derived in the final fit by including $Z \rightarrow \mu\mu + cc, bc, bb$ control region as one normalization nuisance parameter. Both the Z+$Heavy\ Flavor\ Jets$ background and true τ $t\bar{t}$ background are allowed to float in the final fit to get the right normalization scale factors. We assume that the normalization factor for $Z \rightarrow \mu\mu + cc, bc, bb$ and $Z \rightarrow$

$\tau\tau + cc, bc, bb$ are correlated in the two regions. The $t\bar{t}$ background is also correlated in the two regions. The normalization factor for the Z+$Heavy\ Flavor\ Jets$ background is determined to be 1.45 ± 0.15 by the background-only fit. As this scale factor is determined in the limit fit, uncertainty here is the full profiled uncertainty. This procedure is common for both $\tau_\ell\tau_{\rm had}$ and $\tau_{\rm had}\tau_{\rm had}$ channels. Table 7.2 shows the yields of different background processes in the Z+$Heavy\ Flavor\ Jets$ control region (background-only post-fit).

Sample	Post-fit yield
$Z \to \ell\ell + (cc, bc, bb)$	8540 ± 450
Top quark	4030 ± 420
Other $(W + Z + (ll, lc, lb) + VV)$	320 ± 120
Total Background	12890 ± 110
Data	12897

Table 7.2: Event yields in the $Z \to \mu\mu$+ 2 b-tag control region for a background-only fit. The category 'Other' includes contributions from W+jets, Z/γ^*+light-flavour jets, and di-boson processes.

7.6 $Z \to ee$ background normalization

The $Z \to ee$+$Jets$ background has a negligible contribution in the $\tau_{\rm had}\tau_{\rm had}$ channel because of the fact that the two electrons are very unlikely to be misidentified as hadronic τs at the same time. The normalization of the $Z \to ee + Jets$ background is checked in a $Z \to ee + Jets$ control region. The definition of the control regions is:

- Standard event selection in $\tau_\ell\tau_{\rm had}$ and $\tau_{\rm had}\tau_{\rm had}$ region.
- $m_{\rm T}^W < 40\ GeV$.
- $E_{\rm T}^{\rm miss}$ ϕ centrality > 0.
- di-τ visible mass, $81\ GeV < m_{\tau\tau}^{\rm visible} < 101\ GeV$.
- zero or one b-tagged jet in the event.

The Z+$Heavy\ Flavor\ Jets$ background normalization factor described in Section 7.5 is applied to the $Z \rightarrow ee$+cc, bc, bb processes. In the zero b-tag control region, we found a normalization factor of 0.81±0.06. A normalization factor consistent with unity is derived in the one b-tag region. No normalization is applied to the central value of the $Z \rightarrow ee$+b-jet(s) background in the signal region. However, an uncertainty covering the difference between the zero b-tag normalization factor and unity (1.0±0.19) is applied to the 2 b-tag signal region in order to cover mis-modelings in the rate of electrons to fake hadronic τ decays.

CHAPTER VIII

Systematic Uncertainties

"A little error may lead to a large discrepancy" as an old saying in Chinese said. Determining and constraining systematic uncertainties is very critical to a data analysis no matter for search new physics or measuring Standard Model processes. The uncertainties could significantly affect the sensitivity of the data analysis thus it's very important to assess systematic uncertainties correctly and precisely. The systematic uncertainties are estimated and propagated through the full analysis to the final result. For each systematic uncertainty, together with the variation on background normalization are always propagated into the fit. However, variations of the discriminant shape are only propagated when they are significant.

8.1 Luminosity uncertainties

The total nominal luminosity used in this data analysis is about 36.1 fb^{-1}. The uncertainty on the integrated luminosity of the data set used in this analysis is 2.1%, estimated following the same methodology as in reference[96]. The number is derived from a preliminary calibration of the luminosity scale using $x - y$ beam-separation scans performed in August 2015 and May 2016. This correlated systematic uncertainty is applied to all signals and backgrounds processes because the signals and backgrounds are all normalized to the same luminosity as the data used. The lu-

minosity uncertainty is not applied to fake τ backgrounds which are estimated from data using a data-driven method in both channels.

8.2 Detector-related uncertainties

The background and signal Monte Carlo simulations both have detector simulations involved as described in Chapter VI. Thus we have to include the uncertainties related to detector simulations when using Monte Carlo simulations. In the $\tau_\ell\tau_{\rm had}$ channel, there are leptons presented. So we will have to take account the systematic uncertainties related to muons and electrons. In both $\tau_\ell\tau_{\rm had}$ and $\tau_{\rm had}\tau_{\rm had}$ channel, there are τs, jets and $E_{\rm T}^{\rm miss}$ involved, so that we will have to also take into account the systematic uncertainties of τ, jets and $E_{\rm T}^{\rm miss}$. Lastly, the jets are required to be specifically b-jets. We will also consider the systematic uncertainties related to the flavor tagging. The systematic uncertainties of the leptons are small compared with those related to τs and jets. Table 8.1 summarized the categories of systematic uncertainties considered in this analysis.

- Electrons: The electron energy scale and resolution are corrected to ensure good agreement between MC predictions and data. Uncertainties related to electron trigger, identification, reconstruction efficiency and isolation are taken into account.

- Muon: In order to minimize the differences in resolution between data and MC events, scaling and smearing corrections are applied to the $p_{\rm T}$ of simulated muons. So there will be systematic uncertainty on these corrections as a shape dependent systematic uncertainties in the final fit. Besides these systematic uncertainties on the corrections, muon identification efficiency and trigger selection efficiency difference between data and Monte Carlo are also taken into account as systematic uncertainties.

Systematic uncertainty	Type	Components
Luminosity	N	1
Pile-up	SN	1
Reconstructed Objects		
Electron trigger+reco+ID+isolation	SN	4
Electron energy scale	SN	1
Muon trigger+reco+ID+isolation	SN	12
Muon momentum scale+resolution	SN	3
τ trigger+reco+ID+EOR	SN	9
τ energy scale	SN	3
Jet energy scale	SN	3
Jet energy resolution	SN	1
Jets JVT	SN	1
Jet flavour tagging	SN	14
Missing transverse momentum	SN	3

Table 8.1: List of systematic uncertainties considered. An "N" means that the uncertainty is taken as normalization-only for all processes and channels affected, whereas "SN" means that the uncertainty is taken on both shape and normalization. Some of the systematic uncertainties are split into several components for a more accurate treatment.

- Tau: The τ energy scale and identification efficiency is corrected in Monte Carlo to get better agreement with data. Systematic uncertainties related to the τ-electron overlap removal, τ trigger and reconstruction are also considered as normalization and shape variation in the final fit. None of these systematic uncertainties has a shape change on the final BDT more than 5%.

- Jet: The jet energy scale(JES) and resolution(JER) uncertainties, as well as, uncertainty due to pile-up effect are taken into account for jets.

- $E_{\mathrm{T}}^{\mathrm{miss}}$: Uncertainties on the energy scale and resolution of the electrons, muons, jets and τs are propagated to the calculation of the $E_{\mathrm{T}}^{\mathrm{miss}}$, which also has additional dedicated uncertainties on the scale, resolution and reconstruction efficiency of the tracks not associated to any of the reconstructed objects, along with the modeling of the underlying event.

- Flavor tagging: The flavor tagging efficiency is found to be different between MC simulation and data. So a correction is derived to account for this difference which is measured separately for b, c, and light-flavor jets[67]. The calibrations and uncertainties on the mis-identification of c and light-flavor jets as b-jets are derived from samples of W + c-jet events and multi-jet events in Run 2 data. The uncertainty on the c-jet calibration is inflated by the difference measured in W + c-jet events and semi-leptonic $t\bar{t}$ decay events. Correction factors for b-jets using $t\bar{t}$ events have been derived using Run 2 data. All three correction factors have many sources of uncertainty and are decomposed into uncorrelated components, which are then treated independently resulting in 3 uncertainties for c-jets, 4 uncertainties for b-jets, and 5 for light-flavor jets. Table 8.2 lists the systematic uncertainties considered on flavor tagging.

Flavour tagging variations
FT_EFF_extrapolation
FT_EFF_extrapolation_from_charm
FT_EFF_Eigen_Light_0
FT_EFF_Eigen_Light_1
FT_EFF_Eigen_Light_2
FT_EFF_Eigen_Light_3
FT_EFF_Eigen_Light_4
FT_EFF_Eigen_B_0
FT_EFF_Eigen_B_1
FT_EFF_Eigen_B_2
FT_EFF_Eigen_C_0
FT_EFF_Eigen_C_1
FT_EFF_Eigen_C_2
FT_EFF_Eigen_C_3

Table 8.2: List of systematic uncertainties related to flavor-tagging considered in the analysis.

Table 8.3 gives a summary of the systematic uncertainties related to electrons, muons, τs, jets and $E_{\mathrm{T}}^{\mathrm{miss}}$ which are taken into account in the analysis.

Systematic uncertainty
MUON_SCALE
MUON_MS
MUON_ID
MUON_TTVA_SYS
MUON_TTVA_STAT
MUON_EFF_SYS
MUON_EFF_STAT
MUON_EFF_TrigSystUncertainty
MUON_EFF_TrigStatUncertainty
MUON_ISO_SYS
MUON_ISO_STAT
MUON_EFF_SYS_LOWPT
MUON_EFF_STAT_LOWPT
MUON_SAGITTA_RHO
MUON_SAGITTA_RESBIAS
EG_SCALE_ALL
EG_RESOLUTION_ALL
EL_EFF_Reco_TOTAL_1NPCOR_PLUS_UNCOR
EL_EFF_ID_TOTAL_1NPCOR_PLUS_UNCOR
EL_EFF_Trigger_TOTAL_1NPCOR_PLUS_UNCOR
EL_EFF_Iso_TOTAL_1NPCOR_PLUS_UNCOR
TAUS_TRUEHADTAU_SME_TES_DETECTOR
TAUS_TRUEHADTAU_SME_TES_INSITU
TAUS_TRUEHADTAU_SME_TES_MODEL
TAUS_TRUEHADTAU_EFF_ELEOLR_TOTAL
TAUS_TRUEHADTAU_EFF_JETID_TOTAL
TAUS_TRUEHADTAU_EFF_JETID_HIGHPT
TAUS_TRUEHADTAU_EFF_RECO_TOTAL
TAUS_TRUEHADTAU_EFF_RECO_HIGHPT
TAUS_TRUEHADTAU_EFF_TRIGGER_TOTAL2016
TAUS_TRUEHADTAU_EFF_TRIGGER_STATMC2015
TAUS_TRUEHADTAU_EFF_TRIGGER_SYST2015
TAUS_TRUEHADTAU_EFF_TRIGGER_TOTAL
JET_GroupedNP_1
JET_GroupedNP_2
JET_GroupedNP_3
JET_JER_SINGLE_NP
JET_JvtEfficiency
MET_SoftTrk_Scale
MET_SoftTrk_ResoPerp
MET_SoftTrk_ResoPara
PRW_DATASF

Table 8.3: List of systematic uncertainties related to electrons, muons, τs, jets and $E_{\mathrm{T}}^{\mathrm{miss}}$ considered in the analysis.

8.3 Background modeling uncertainties

8.3.1 Uncertainties on Z+$Jets$ modeling

Uncertainties on the $Z + jets$ background modeling related to the choice of renormalization and factorization scales are evaluated using the event weights included in the Sherpa 2.2.1 samples, varying the scales by different combinations up and down a factor of two. The envelop of all these variations is taken as the overall uncertainty related to the choice of scale. Fig. 8.1 shows these variations with different scale combination in terms of invariant mass of the two b-jets (m_{bb}) and transverse momenta of these two b-jets($p_{\mathrm{T}}(bb)$).

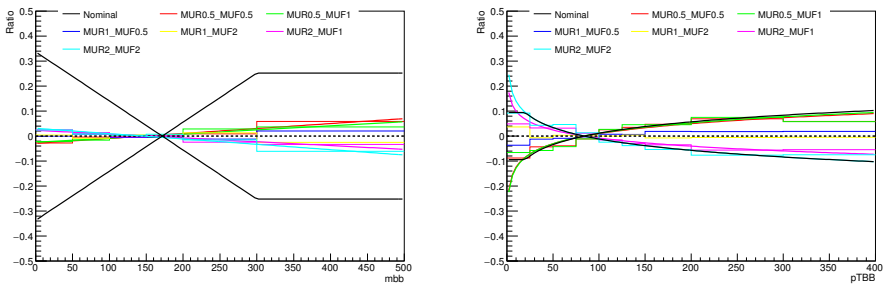

Figure 8.1: Effects of renormalization and factorization scale uncertainties on Z+$Jets$ background modeling for m_{bb} (left) and $p_{\mathrm{T}}(bb)$ (right) distributions.

The uncertainty on the choice of PDF set is evaluated in the identical way, also using the event weights included in the samples. The PDF variations include 100 replicas of the nominal NNPDF3.0 PDF set and central values of two different PDF sets, MMHT2014nnlo68cl and CT14nnlo. The NNPDF intra-PDF uncertainty is estimated as the standard deviation of the 101 NNPDF3.0 sets. The uncertainty from choice of the other two nominal PDF sets are set as the envelop of the differences from the nominal NNPDF set. Fig. 8.2 shows the variations on different PDF choices.

The uncertainty on choice of different Monte Carlo generator is done by comparing with $Z + Jets$ samples simulated using MG5_aMCNLO v2.2.2[97] at leading order

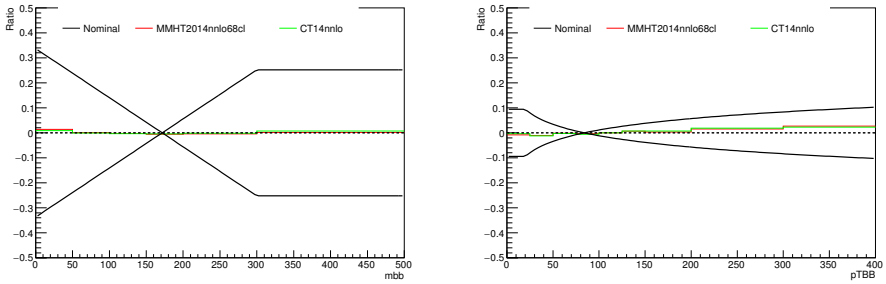

Figure 8.2: Effects of choice of PDF set on Z+$Jets$ background modelling in the $\tau_\ell\tau_{\text{had}}$ channel for m_{bb} (left) and $p_{\text{T}}(bb)$ (right) distributions.

interfaced to the Pythia 8.186[98] parton shower model. The A14 tune is used together with the NNPDF2.3LO PDF set[79]. The EvtGen v1.2.0 program[99] is used for properties of the bottom and charm hadron decays. The comparison plots of these two generators are showed in Fig. 8.3.

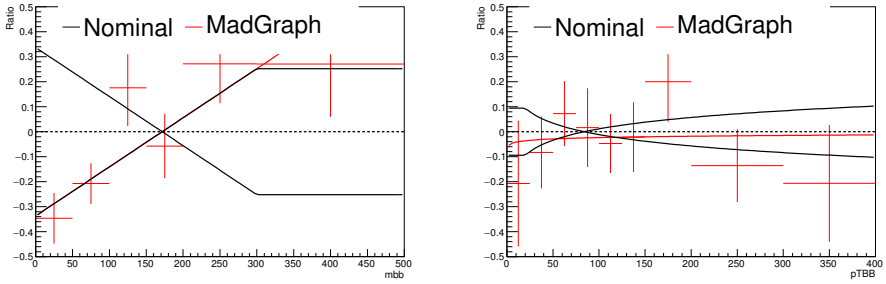

Figure 8.3: Effects of generator choice on Z+$Jets$ background modeling in the $\tau_\ell\tau_{\text{had}}$ channel for m_{bb} (left) and $p_{\text{T}}(bb)$ (right) distributions.

For all sources of these systematic uncertainties, the discrepancy from the nominal sample is parameterized on m_{bb} and $p_{\text{T}}(bb)$. These two variables have the largest variations after the modifications on generator level. The discrepancy got propagated through the analysis as a shape uncertainty onto the BDT output score. The effect of these systematic uncertainties on the BDT output distributions is shown in Fig 8.4. Blue and red solid lines in the plots represent the upper and downward systematic uncertainty fluctuation directions.

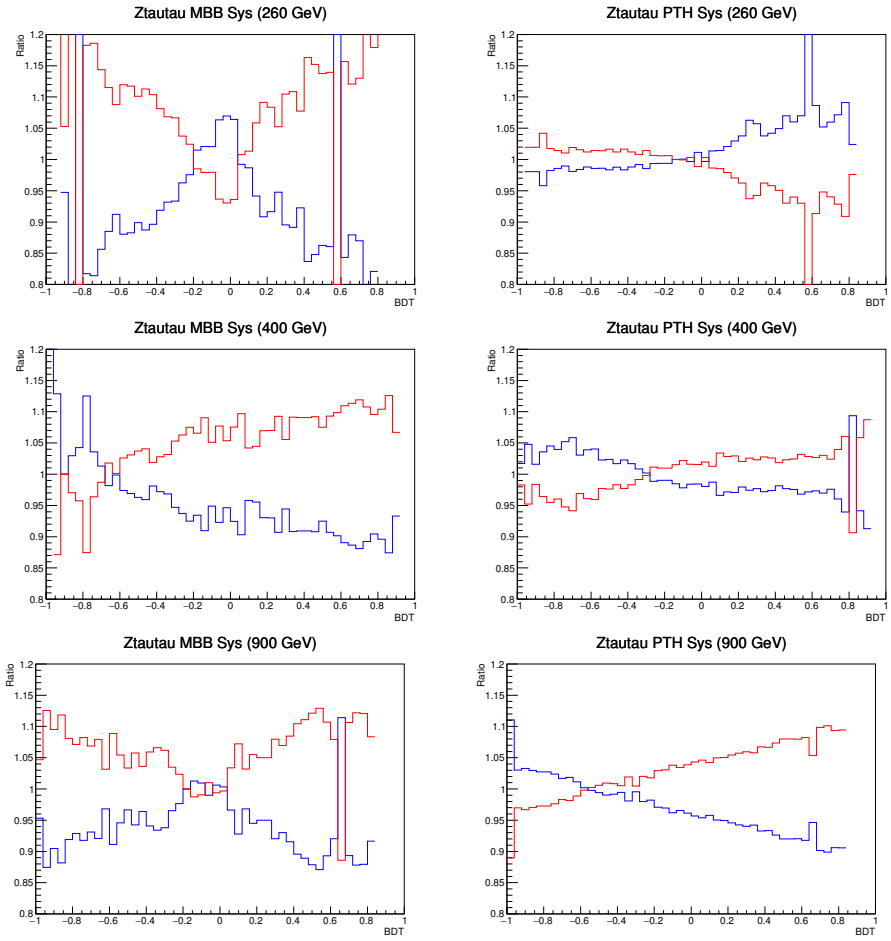

Figure 8.4: The combined systematic uncertainties from all sources on Z+$Jets$ background modeling in the $\tau_\ell\tau_{\rm had}$ channel for m_{bb} (left) and $p_{\rm T}(bb)$ (right) distributions, for the 260 GeV (top), 400 GeV (center) and 900 GeV (bottom) signal mass point trainings.

8.3.2 $W+Jets$ systematic uncertainty in $\tau_{\text{had}}\tau_{\text{had}}$ channel

In the $\tau_\ell\tau_{\text{had}}$ channel signal region with 2 b-tagged jets, true τ $W+Jets$ plays a really small role among all the backgrounds. A 30% uncertainty is assigned to account for the uncertainties on production of $W+HeavyFlavorJets$. This is estimated from the VH resonances analysis[100] with sources of uncertainties coming from generator comparison, factorization and renormalization scale, PDF, and α_s variations.

In the $\tau_{\text{had}}\tau_{\text{had}}$ channel, significant amount of $W+Jets$ background is presented. Instead of only considering true τ background in the $\tau_\ell\tau_{\text{had}}$ channel, we also have to estimate the uncertainty on the fake τ background from the $W+Jets$ Monte Carlo simulations. In order to do this, we compare the MC simulation and data-driven prediction of $W+Jets$ background in the 0 b-tag control region from $\tau_\ell\tau_{\text{had}}$ channel which is dominated by $W+Jets$. We found a 31% uncertainty to cover the difference between MC simulation and data-driven estimation. Table 8.4 shows the comparison of the yields from MC simulation and data-driven prediction in the 0 b-tag control region for $W+Jets$ background.

		Tranfer factors
	MC W+jets fakes	43739.1
	data driven	57288.7
	difference	+ 30.98%

Table 8.4: Estimation of the uncertainty on the τ fakes by comparing the MC prediction to the data driven prediction in the $\tau_\ell\tau_{\text{had}}$channel.

Together with the production uncertainty of the $W+Jets$, which is 30%, Adding these two uncertainties(31% and 30%) in quadrature gives us 43%. Thus, to be conservative, we assign a 50% uncertainty as the total uncertainty of the $W+Jets$ background in the $\tau_{\text{had}}\tau_{\text{had}}$ channel. Even we choose a relatively large uncertainty here to be conservative, checks have been done to study the effect of this uncertainty. As $W + Jets$ only accounts for less than 1% contribution of total yields in the signal region, thus this systematic uncertainty really makes no difference in the result.

8.3.3 Uncertainties on top quark modeling

In both $\tau_\ell\tau_{\text{had}}$ and $\tau_{\text{had}}\tau_{\text{had}}$ channels, the $t\bar{t}$ background component with fake τ decays uses data-driven method to estimate instead of using Monte Carlo simulation. So the generator level uncertainties of $t\bar{t}$ background are only applied to the $t\bar{t}$ component with true hadronic τ decays.

Generator level uncertainties related to $t\bar{t}$ modeling contain the uncertainties associated with shower radiation and hadronization model. The estimation of these systematic uncertainties follows the procedures below:

- Change the Powheg+Pythia 6 factorization and normalization factors up and down by a factor of 2
- Compare the fragmentation model to Powheg+Herwig simulation
- Compare samples generated by aMC@NLO and showered using Herwig++ to samples generated by Powheg and showered by Herwig++ to cover the uncertainty due to the hard scatter generation in different generators.

Similar to what has been done for the $Z+Jets$ background, the shape of these different variations are parameterized as functions of m_{bb} and $p_{\text{T}}(bb)$. Still, this is due to the fact that these two variables are the most sensitive which have the largest variations among all the kinematic variables. All these variations will be propagated to the change in the BDT output score used for the final fit. Fig 8.5 and Fig. 8.6 show the generator systematic uncertainty effect on m_{bb} and $p_{\text{T}}(bb)$ in SLT and LTT categories.

Variation shapes from the $\tau_\ell\tau_{\text{had}}$ channel are used for $\tau_{\text{had}}\tau_{\text{had}}$ channel because in principle the top background in $\tau_{\text{had}}\tau_{\text{had}}$ channel should have identical variation shapes. However, the overall change in acceptance due to the variations are significantly different for $\tau_\ell\tau_{\text{had}}$ and $\tau_{\text{had}}\tau_{\text{had}}$ channels. An uncertainty is estimated to cover the discrepancy on acceptance between two channels by comparing the MC-to-MC

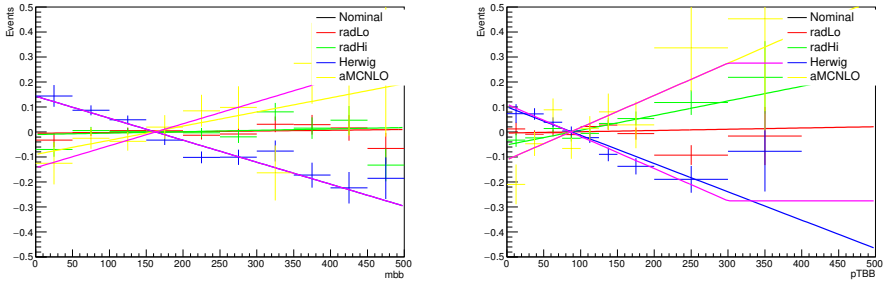

Figure 8.5: Effects of $t\bar{t}$ generator acceptance uncertainties in the $\tau_\ell\tau_{\text{had}}$ SLT channel for m_{bb} (left) and $p_{\text{T}}(bb)$ (right) distributions. The magenta lines represent the symmetric envelopes that are taken as the uncertainty.

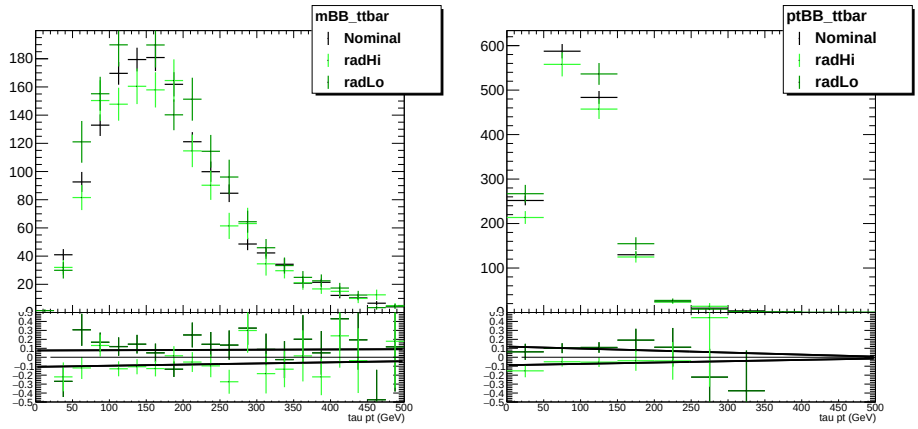

Figure 8.6: Effects of $t\bar{t}$ generator acceptance uncertainties in the $\tau_\ell\tau_{\text{had}}$ LTT channel for m_{bb} (left) and $p_{\text{T}}(bb)$ (right) distributions.

ratio of true $t\bar{t}$ yields change in $\tau_{\text{had}}\tau_{\text{had}}$ and $\tau_\ell\tau_{\text{had}}$ signal region. It is found to be 30% up and 32% down.

8.3.4 $Z \to ee$ and SM Higgs process uncertainties

For the $Z \to ee$ background, a normalization factor is derived in the $Z \to ee$ control region with one b-tag and it is found to be consistent with 1.0. In this case, no normalization correction factor is applied. However, we still have to consider the uncertainty on this unity normalization factor to cover any discrepancy between data and simulation in the rate for electrons faking τs. To check this, we compare the normalization factor derived from the 0 b-tag $Z \to ee$ control region with the one we get from 1 b-tag $Z \to ee$ control region which is unity. We found a 19% discrepancy between these two normalization factors. We apply a 19% uncertainties to cover the discrepancy between electron faking τ rate in data and MC simulations.

For the SM ZH background, a normalization uncertainty of 28% is applied based on the latest experimental uncertainty of this measurement. A 30% uncertainty is applied to the top-quark associated Higgs production background ttH.

8.3.5 Uncertainties on fake-τ background estimate in $\tau_\ell\tau_{\text{had}}$ channel

The fake τ background in the $\tau_\ell\tau_{\text{had}}$ channel is estimated and modeled using a data-driven combined fake factor method. Several different systematic uncertainties are applied for the fake-τ background in $\tau_\ell\tau_{\text{had}}$ channel. The τ fake factors are used to estimate the fake τ background in the signal region. So that the statistical uncertainty together with the variations in the fake-τ estimation are included as a source of normalization uncertainty. The fake factors are allowed to vary up and down by their statistical uncertainty. When using the template from the anti-τ region before applying fake factors, the true τ $t\bar{t}$ background are subtracted. So the contribution from the true τ $t\bar{t}$ component is varied up and down by detector-related uncertainties,

theoretical uncertainties related to $t\bar{t}$ modeling, and also a 6% NLO cross section uncertainty on $t\bar{t}$ production. Fig 8.7 shows the detector related uncertainty effect on the true τ $t\bar{t}$ shape which will be subtracted when doing fake τ background estimation. Fig 8.8 and 8.9 give the variation of the true τ $t\bar{t}$ on generator level uncertainties. In the control region where τ fake factors are applied to, contributions from electroweak, single top, di-boson and Higgs background MC simulations are varied up and down by 50% when estimating the fake τ background.

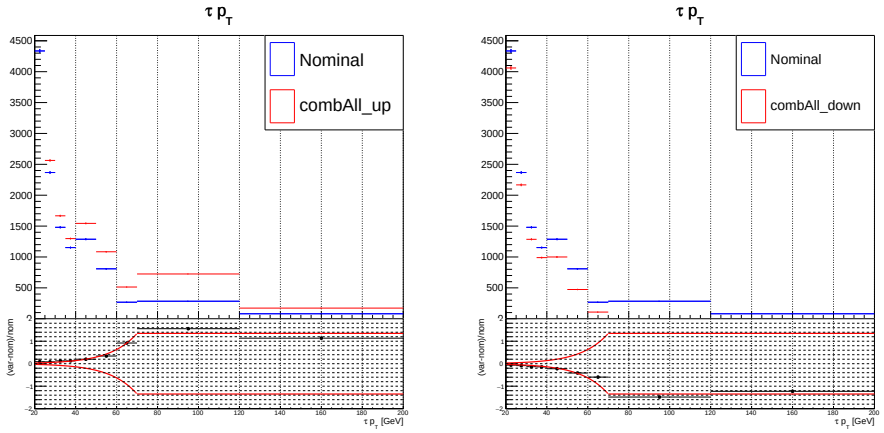

Figure 8.7: The estimated shape variation due to the effect of detector-related systematic variations on the $t\bar{t}$ background component that is subtracted from the data as part of the fake factor method. All sources of systematic uncertainty are considered, but those lead to negligible variations are not included.

When using the combined fake factor method to estimate the fake τ background, the r_{QCD} is also involved in this procedure. So the systematic uncertainties related to the r_{QCD} should also be taken into account. Similar techniques to the uncertainty evaluation on fake factors are used here for the r_{QCD} systematic uncertainties. When calculating r_{QCD}, there are MC simulation background subtraction involved too. The uncertainties on MC simulations have to be considered. All backgrounds except $t\bar{t}$ are varied by a uncertainty of 50% when calculating the r_{QCD}. The detector related uncertainties and generator related uncertainties on $t\bar{t}$ modeling are also propagated through the r_{QCD} calculation. Both shape and normalization uncertainties are in-

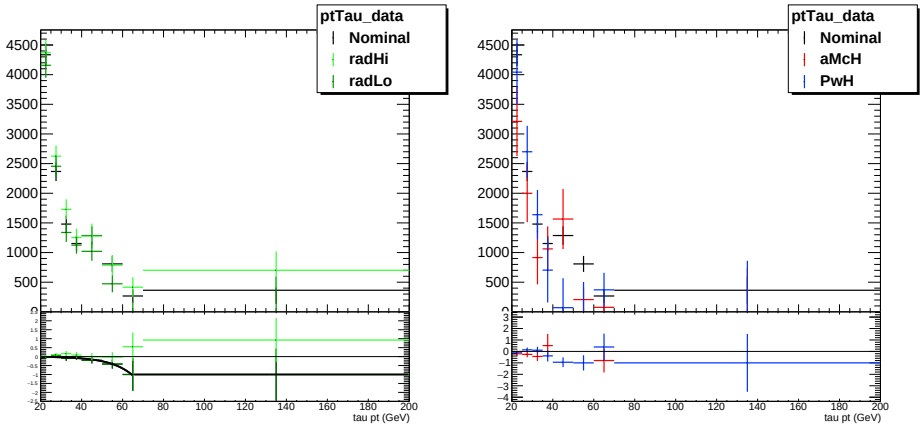

Figure 8.8: Shape variations when using different $t\bar{t}$ MC generators in the fake-τ estimate in the $\tau_\ell\tau_{\text{had}}$ channel (SLT category). In the Herwig case the large statistical uncertainties dominate.

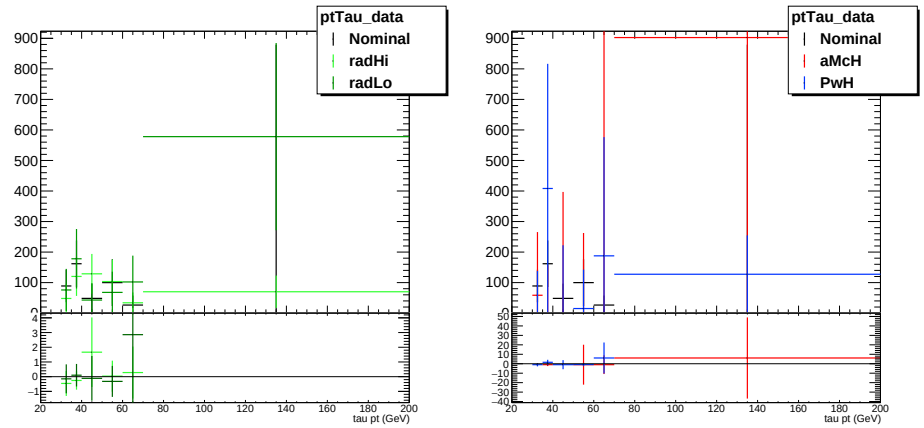

Figure 8.9: Shape variations when using different $t\bar{t}$ MC generators in the fake-τ estimate in the $\tau_\ell\tau_{\text{had}}$ channel (LTT category). In the Herwig case the large statistical uncertainties dominate.

cluded.

The multi-jet fake factors are derived from a control region with leptons failing the isolation requirement. While the signal region does have an isolation requirement on the leptons. An extra systematic uncertainty is derived to cover any discrepancy caused by this. We compare the multi-jet fake factors derived from the isolated lepton, same sign region with the ones from non-isolated lepton, same sign region. The difference between fake factors from these two regions are considered to cover the difference between isolated and non-isolated lepton region.

A systematic uncertainty is assigned to cover the difference in composition of fake τs in the anti-tau control region and the signal region. A fit to the ratio of data to simulation of the m_{hh} distribution in a region with same-sign charge τ and lepton and 2 b-tags is parameterized to obtain a variation on the output BDT score. The fit is symmetrized in order to provide both up and down variations. The variable m_{hh} is chosen for the parameterization since this shows the largest variation in fake-τ composition across the distribution, and shows the greatest discrepancies between data and MC out of all of the BDT input variables.

An additional uncertainty on the fake-τ component of the $t\bar{t}$ background is estimated by evaluating the fake factor in MC simulations using the nominal selection and in a high m_{T} region ($m_{\mathrm{T}}>$ 40 GeV, normal $t\bar{t}$ control region definition). The difference between the two for each bin is then applied as up and down variations to the nominal fake factor derived from data and the $t\bar{t}$ background estimation is re-calculated in each case. The shape of this uncertainty is found to be flat therefore this is treated as a normalization only uncertainty. Fig 8.10 is the plot showing the difference between the low and high m_{T} region $t\bar{t}$ fake factors in the SLT and LTT sub-channels. All other uncertainties are included as shape and normalization uncertainties in the fit. For each systematic variation, $\mathrm{r_{QCD}}$ is recalculated.

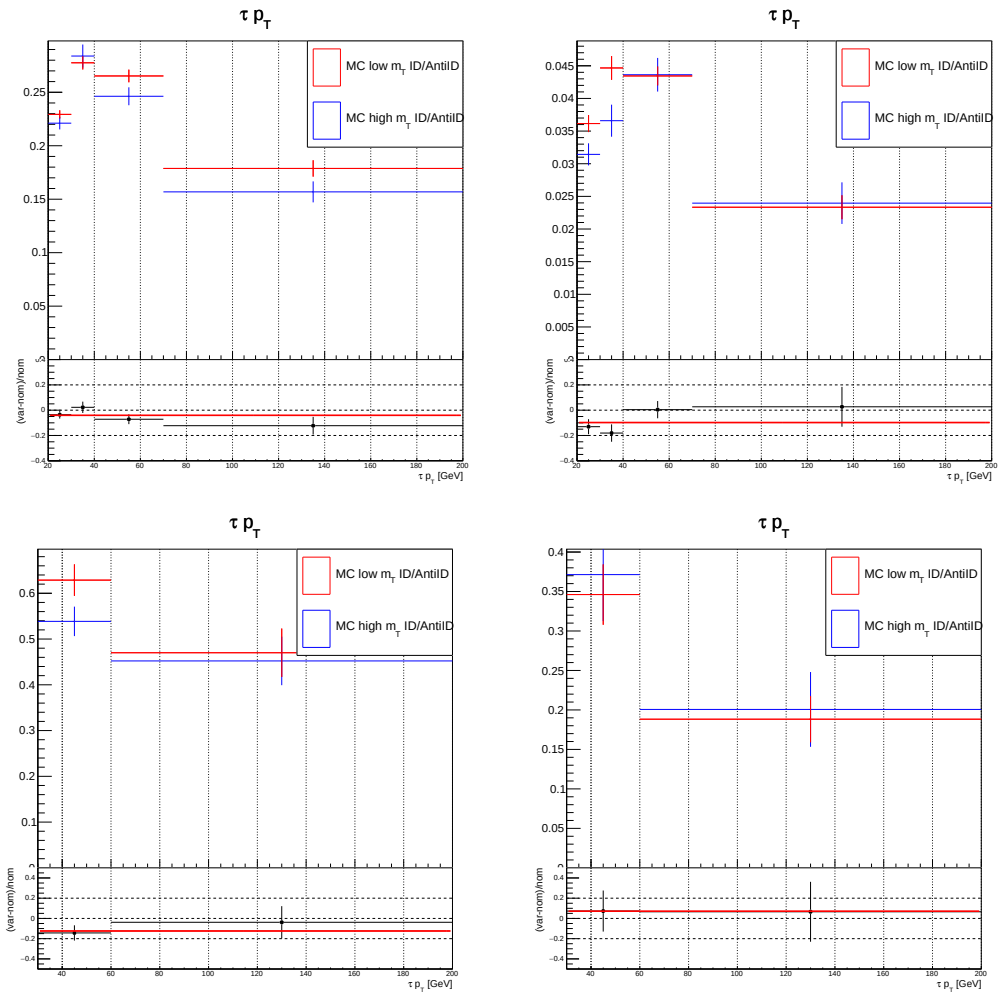

Figure 8.10: Effects on the fake factors for $t\bar{t}$ background when deriving them in high and low (i.e. the nominal) m_{T} regions with 2 b-tags for SLT (top) and LTT (bottom) category events for 1-prong (left) and 3-prong (right) τs.

8.3.6 Uncertainties on fake-τ background estimation in the $\tau_{\text{had}}\tau_{\text{had}}$ channel

As is done in the $\tau_\ell\tau_{\text{had}}$ channel, a systematic uncertainty is also assigned to cover the difference in composition of fake τs in the anti-τ control region and the signal region by using the difference between data and simulation of the leading τ p_{T} distribution in the 1 b-tag region to provide a parameterization of the variation on the output BDT score.

The fake-factors for the multi-jet background estimation are allowed to vary up and down by their statistical uncertainty. A systematic uncertainty due to variations in the contributions from electroweak, top, di-boson and Higgs boson background processes is estimated by varying them up and down by a conservative 50% when re-calculating the fake-factors. All of these uncertainties are included as both shape and normalization effects.

The transfer factors (defined as the ratio of inclusive fake-factors in the 2 b-tag region to the value of an inclusive fake-factor derived in the 1-tag region) are statistically limited. The transfer factors are varied within their statistical uncertainties to evaluate the normalization uncertainty.

The multi-jet modeling we finally got is actually in the opposite sign(OS) region while we do have to use the fake factors derived in the same sign(SS) region. This is one obvious difference between them. In order to account for differences in the fake-τ modeling between the opposite-sign and same-sign regions, the ratio of OS τs to OS anti-τs is compared to the ratio of SS τs to SS anti-τs, in a multi-jet control region defined by adding the requirement that $\delta\phi(\tau\tau) > 2.0$ to the standard selection. The double ratio is taken as a p_{T}-dependent systematic uncertainty. Fig 8.11 shows the fake factors from the OS and SS regions.

Several sources of uncertainties related to the estimation of the $t\bar{t}$ background component containing fake-τs are considered. The contribution of MC events con-

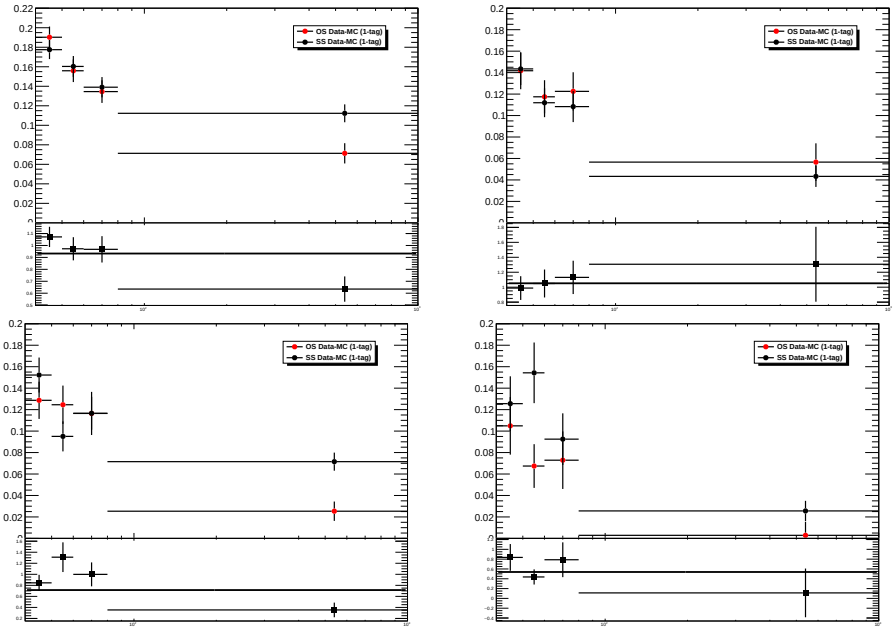

Figure 8.11: The ratio of the number of ID to anti-ID events in OS events and in SS events in the hadhad channel QCD CR as a function of τ p_{T}. The fit to the double ratio in the bottom panels is taken as the systematic uncertainty on the fake factors in the hadhad channel. From top to bottom, left to right, these plots show the τ fake factors for the 1P1P, 1P3P, 3P1P and 3P3P τ pairs in SS and OS regions.

taining a true hadronic τ that is subtracted from the data region used to derive the fake-rates is varied up and down by 10%. This variation covers the normalization uncertainty on the $t\bar{t}$ background derived in the final fit, as all other background processes have a negligible contribution in this region. The m_{T} cut is varied from its nominal value of 80 GeV to 65 GeV, making the control region closer to the signal region, although decreasing the purity of the region. The fake-τ $t\bar{t}$ component is evaluated for each of the theoretical uncertainties (described in Section 8.3.3). Since the statistical precision of the fake-τ component is poor and the variations are compatible with those observed in the true-τ $t\bar{t}$ component, the latter is used to evaluate both shape and normalization effects due to these sources of uncertainty. A p_{T} dependent systematic uncertainty is applied to account for the difference in the p_{T} distribution due to applying only DTT p_{T} threshold cuts but not DTT + STT cuts. This goes up to 30% at high p_{T} where the STT is dominant. Finally, the derived fake rates are varied up and down by their statistical uncertainty.

8.4 Theoretical uncertainties on signal

The theoretical uncertainty on the cross-section for non-resonant Standard Model Higgs pair-production is $33.41^{+4.3}_{-6.00}$(scale) $\pm$5 (theory) $\pm$2.3 (α_s) $\pm$2.1(PDF) fb[101, 102]. All the related uncertainties are added quadratically, summing up to 8% which is applied as a normalization uncertainty to the signal.

The signal samples are generated with modified parameters to probe uncertainties on parton density functions, uncertainties in renormalization and factorization scale and uncertainties due to modeling of parton shower and underlying event including multi-parton interactions. The uncertainties are calculated by comparing the acceptance times efficiency(A x ϵ) for different modifications. The uncertainties related to choice of different PDFs are found to be negligible for all signals in this analysis. For the non-resonant signal, the renormalization and factorization scale uncertainties are

also negligible, however, the uncertainty on the parton shower modeling is found to be 5% for the $\tau_\ell\tau_{\text{had}}$ signals and 9% for the $\tau_{\text{had}}\tau_{\text{had}}$ signals. For the resonant signals, the renormalization and factorization scale uncertainty together with the parton shower uncertainty are calculated to be 12% for both channels.

CHAPTER IX

Statistical Methods

People say that the language of science is mathematics. I say the language of experimental physics is statistics. The statistical analysis provides a bridge connecting the theoretical predictions and experimental observations. It plays a critical role helping us to interpret the experimental analysis. Events on LHC happen with certain probability determined by physics laws. Furthermore, as an experiment, the systematic uncertainties have to be taken into account. The statistical analysis method is the tool to wrap all of them together, giving us the final interpretation of our experimental observations. The statistical method in experimental particle physics could easily extend to a very long book, there will be too much content to cover if one wants to go into details. Thus this chapter will just introduce the construction of the statistical model for data analysis on LHC, different test statics used in different hypothesis testing scenarios (evaluation of the significance for new discovery uses different test statics from setting upper limit on the production rate of physics models). The treatment of systematic uncertainties will also be briefly discussed in this chapter.

9.1 Profiled likelihood function

In order to construct a test static, we will use the method called Profiled Likelihood Method[103, 104]. The construction of the likelihood function uses the product of independent Poisson distributions in all bins of the measured histograms in signal region and the background control region.

Suppose we have measured our real data in the signal region on variable x. The choice of x should follow the principle that signals and backgrounds have significant shape difference on x because finally we will fit our background and signal simulations, whether using Monte Carlo or data-driven method to estimate, to the shape of this measured variable. In this analysis, x is the BDT output score in the signal region on which signals and backgrounds distribute differently with great significance. We could construct a histogram denoted as $\mathbf{n} = (n_1, \ldots, n_N)$ from bin 1 to bin N. The expectation value of each bin n_i could be written as:

$$E[n_i] = \mu s_i + b_i \tag{9.1}$$

The expected number of events in the ith bin from signal and background are:

$$s_i = s_{tot} \int_{\text{bin i}} f_s(x; \boldsymbol{\theta_s}) dx \tag{9.2}$$

$$b_i = b_{tot} \int_{\text{bin i}} f_b(x; \boldsymbol{\theta_b}) dx \tag{9.3}$$

where μ is a parameter that determines the strength of the signal process within range [0,1]. When $\mu = 0$, it corresponds to background-only hypothesis and $\mu = 1$ corresponds to the nominal signal hypothesis. $f_s(x; \boldsymbol{\theta_s})$ and $f_b(x; \boldsymbol{\theta_b})$ are the probability density functions(pdfs) of the variable x for signal and background events. $\boldsymbol{\theta_s}$ and $\boldsymbol{\theta_b}$ are the parameters which determine the shape of the pdfs of signal and background.

s_{tot} and b_{tot} are the total expected number of signal and background. $\boldsymbol{\theta_s}$, $\boldsymbol{\theta_b}$ and b_{tot} are the related parameters but not the ones we are interested, we call them nuisance parameters. The signal normalization s_{tot} is not a nuisance parameter because it is fixed to the value predicted by the nominal signal model.

Besides the signal region histogram $\mathbf{n}$ mentioned before, physicists usually include a subsidiary measurement histogram from a background enriched control region to help constrain the nuisance parameter. In this analysis, it's the Z+$Heavy\ Flavor\ Jets$ background control region. Suppose that we have got a histogram $\mathbf{m} = (m_1, \ldots, m_M)$ from a background control region. The expectation number of entries in each bin of $\mathbf{m}$ could be written as:

$$E[m_i] = u_i(\boldsymbol{\theta}) \tag{9.4}$$

The construction of this measurement provides the normalization factor of the Z+$Heavy\ Flavor\ Jets$ background, which has bad Monte Carlo modeling, while generally, the auxiliary measurement of a background control region could provide information on the signal and background shape parameters as well.

The likelihood function is constructed using the product of Poisson probability for all bins with knowing that all the bins in histogram n and m are independent, as showed in Eq. 9.5:

$$L(\mu, \boldsymbol{\theta}) = \prod_{j=1}^{N} \frac{(\mu s_j + b_j)^{n_j}}{n_j!} e^{-(\mu s_j + b_j)} \prod_{k=1}^{M} \frac{u_k^{m_k}}{m_k!} e^{-u_k} \tag{9.5}$$

The likelihood function depends on the signal strength μ and the nuisance parameters θ. Noticing that Eq. 9.5 has no systematic uncertainty involved yet. We surely have to figure out ways to incorporate the systematic uncertainties into the binned Poisson likelihood function because the systematic uncertainties are always critical to determine how good our experiment is. There are mainly two types of systematic

uncertainties in general, multiplicative uncertainties and shape uncertainties. Multiplicative uncertainties are relatively easier to deal with while the shape uncertainties need the techniques which we call "morphing" to be incorporated into the likelihood function.

Multiplicative uncertainties are easy to incorporate into the likelihood function as it will be just an extra scale factor added in the likelihood function. One example of the multiplicative uncertainties is the systematic uncertainty of the integrated luminosity. Usually, the integrated luminosity is measured in some auxiliary measurement in other experiment. Assuming the integrated luminosity value is measured as $\tilde{L} \pm \sigma_L$, the likelihood function then could be written with the integrated luminosity systematic uncertainty implemented as below[105]:

$$L(\mu, \boldsymbol{\theta}, L) \times N(L|\tilde{L}, \sigma_L) \tag{9.6}$$

where function $N(L|\tilde{L}, \sigma_L)$ is a Gaussian distribution with mean value $\tilde{L}$ and width σ_L which is used to constrain the nuisance parameter L. The likelihood function $L(\mu, \boldsymbol{\theta}, L)$ depends on L, not $\tilde{L}$ now. In addition to the systematic uncertainties on the integrated luminosity, the systematic uncertainties on cross section and overall efficiency also belong to this type of systematic uncertainties.

Many systematic uncertainties result in an overall change in the shape of the observed spectrum instead of the normalization. This type of systematic uncertainties is more complicated to be wrapped into the likelihood function than the multiplicative uncertainties. One typical systematic uncertainties belonging to this category is the energy scale uncertainty which will affect all jet energy in an event in the same direction. We model it by altering the corresponding nuisance parameter up an down by one standard deviation in the Monte Carlo simulation and recalculating the shifted measurement. Thus, we get one nominal histogram with two extra histograms by shifting the nuisance parameters. We could denote them as, ϵ_{ji}^0, ϵ_{ji}^-, ϵ_{ji}^+, in

which, i, j means the ith bin in the histogram from systematic uncertainty source j. The technique used to extrapolate from these three measurement value into a continuous estimate in each bin of the systematic uncertainties is called "morphing"[105]. Among different "morphing" methods, the "vertical morphing" is the most commonly used and the most straightforward. The "vertical morphing" is done by introducing another random distributed parameter f as:

$$\epsilon_{ji} = \frac{f(f-1)}{2}\epsilon_{ji}^{-} - (f-1)(f+1)\epsilon_{ji}^{0} + \frac{f(f+1)}{2}\epsilon_{ji}^{+} \tag{9.7}$$

f is the random variable introduced with a certain distribution(usually Gaussian) with σ_f=1. The morphing method could be easily extended to multi-source systematic uncertainties situation by linearly adding the extrapolation expression together. There are also some more sophisticated methods to deal with the shape systematic uncertainties, such as "horizontal morphing",etc.

After having an idea about how we construct the likelihood function, we could go one step further to construct the profiled likelihood ratio[104]:

$$\lambda(\mu) = \frac{L(\mu, \hat{\hat{\boldsymbol{\theta}}})}{L(\hat{\mu}, \hat{\boldsymbol{\theta}})} \tag{9.8}$$

In Eq. 9.8, $\hat{\hat{\boldsymbol{\theta}}}$ is the value of $\boldsymbol{\theta}$ which maximizes the likelihood function L for specific value of μ, while $\hat{\boldsymbol{\theta}}$ and $\hat{\mu}$ are the values of $\boldsymbol{\theta}$ and μ which maximizes the unconditional likelihood function. $\hat{\hat{\boldsymbol{\theta}}}$ is the conditional maximum-likelihood estimator of $\boldsymbol{\theta}$ with respect to μ. $\hat{\boldsymbol{\theta}}$ and $\hat{\mu}$ are the maximize-likelihood estimator of $\boldsymbol{\theta}$ and μ. It is not hard to notice that $\lambda(\mu)$ is a function of signal strength μ, which is the thing we are interested the most. Other nuisance parameters are gone by using the likelihood ratio. It's obvious that the value of $\lambda(\mu)$ will fall into range [0,1]. A $\lambda(\mu)$ value closer to 1 implies a good agreement between the data and hypothesized value of μ, while a closing to 0 value of $\lambda(\mu)$ means bad agreement between data and hypothesized value

of μ.

9.2 Test statics

After briefly describing how the profiled likelihood ratio is constructed, we will discuss the test statics[104] we used for the hypothesis test in our data analysis. A test static is a random variable calculated from sample data to determine the degree of agreement between the sample of data and the null hypothesis. The observed value of the test static will change corresponding to different samples. The test static contains the information of the sample of data to determine whether we should reject the null hypothesis. A very simple example of the test static could be illustrated in the experiment of tossing a coin. Imagine we have a coin and we want to know if the coin is fair or not, One way we could do is that we toss the coin many, many times and count how many times head appears. The number of times that head appears is actually a test static of this experiment. This number actually contains the information with which we could tell if the coin is fair or not. If head appears a lot of times or it appears only few times, we know that the coin has a large possibility to be unfair. If the head appears roughly half of the total toss times, we know the coin is likely to be fair.

We have introduced $\lambda(\mu)$ before as a test static, however, it is convenient to use the log test static:

$$t_\mu = -2\ln\lambda(\mu) \tag{9.9}$$

Higher value of t_μ correspond to increasing incompatibility between data and μ. We define the p-value to quantify the level of disagreement as:

$$p_\mu = \int_{t_{\mu,obs}}^{\infty} f(t_\mu|\mu)dt_\mu \tag{9.10}$$

Smaller p-value implies larger incompatibility between the observed μ value and our hypothesis. We usually convert the p-value into an equivalent significance, which is defined below:

$$Z = \Phi^{-1}(1-p) \tag{9.11}$$

where Φ^{-1} is the quantile of the standard Gaussian. Greater value of Z implies greater incompatibility between observation from data and hypothesis.

If we assume that the presence of the new signal can only increase the mean event rate, which means $\mu \geq 0$, the test static is defined as :

$$\tilde{\lambda}(\mu) = \begin{cases} \dfrac{L(\mu, \hat{\hat{\boldsymbol{\theta}}}(\mu))}{L(\mu, \hat{\boldsymbol{\theta}})} & \hat{\mu} \geq 0 \\ \dfrac{L(0, \hat{\hat{\boldsymbol{\theta}}}(\mu))}{L(0, \hat{\hat{\boldsymbol{\theta}}}(0))} & \hat{\mu} < 0 \end{cases} \tag{9.12}$$

Where $\hat{\hat{\boldsymbol{\theta}}}(0)$ and $\hat{\hat{\boldsymbol{\theta}}}(\mu)$ are the maximization likelihood estimators of θ for signal strength equaling to 0 and μ. The corresponding log test static of $\tilde{\lambda}(\mu)$ is :

$$\tilde{t}(\mu) = -2ln\tilde{\lambda}(\mu) = \begin{cases} -2\ln\dfrac{L(\mu, \hat{\hat{\boldsymbol{\theta}}}(\mu))}{L(\mu, \hat{\boldsymbol{\theta}})} & \hat{\mu} \geq 0 \\ -2\ln\dfrac{L(0, \hat{\hat{\boldsymbol{\theta}}}(\mu))}{L(0, \hat{\hat{\boldsymbol{\theta}}}(0))} & \hat{\mu} < 0 \end{cases} \tag{9.13}$$

Similar to $t(\mu)$, we could use $\tilde{\lambda}(\mu)$ to quantify the level of disagreement between the data and the hypothesized value of μ with p-value.

For the discovery of a positive signal, a different test static q_0 is used, it is defined as:

$$q_0 = \begin{cases} -2\ln\lambda(0) & \hat{\mu} \geq 0 \\ 0 & \hat{\mu} < 0 \end{cases} \tag{9.14}$$

Thus the p_0 value used to reject the $\mu = 0$ hypothesis is defined as:

$$p_0 = \int_{q_0,obs}^{\infty} f(q_0|0)dq_0 \tag{9.15}$$

Sometimes, if we are unable to rule out the $\mu = 0$ hypothesis, which means we don't manage to find the target signals, we will have to establish an upper limit on the strength parameter μ for the signals to quantify the possibility that the signals will appear. The test static used to set the upper limit is :

$$q_\mu = \begin{cases} -2\ln\lambda(\mu) & \hat{\mu} \leq \mu \\ 0 & \hat{\mu} > \mu \end{cases} \tag{9.16}$$

with the p-value defined as:

$$p_\mu = \int_{q_\mu,obs}^{\infty} f(q_\mu|\mu)dq_\mu \tag{9.17}$$

Once we have done with choosing the appropriate test static for the corresponding hypothesis test no matter it's for discovery or for setting upper limit, we will have to get the probability distribution function(pdf) of the test static in order to do the integral to get significance or to get the significance limit range. There are two ways to get the pdf of the test statics, one is the asymptotic method, the other one is to use Monte Carlo to generate toy for the test static distribution. The second method is usually more common as sometimes it is not easy to get the asymptotic expression of the pdf.

CHAPTER X

Analysis Result

For all signals in all channels, the BDT output score is used in the final fit as the discriminating variables. The upper limits are placed on two benchmark models for the resonant di-Higgs production: the CP even spin-0 heavy Higgs boson predicted by 2HDM in the narrow width approximation and the spin-2 Randall Sundrum KK graviton with different coupling constant $k/\bar{M}_{PI}$ in the Randall Sundrum graviton model. The resonant signal masses varied between 260 GeV and 1 TeV. The two decay products Higgs are considered as Standard Model like Higgs boson with m_h= 125 GeV and the non-resonant Standard Model Higgs pair-production is also considered. The upper limit is placed for the non-resonant Standard Model Higgs pair-production for both with and without the finite top mass reweighting correction. The finite top mass correction is to correct the infinite top mass assumption when calculating the NLO SM Higgs pair-production cross section.

The BDT output score histograms used for the final fit have to be binned reasonably in order to reduce the statistical fluctuation of the final result. The binning of the BDT score distributions used in the final fit are optimized for different signals. In the $\tau_\ell\tau_{\text{had}}$ channel, for the non-resonant SM signal BDT distribution, it's required to have binning to keep the statistical uncertainty of each bin below 20%, this number is required to be 40% for the resonant signals in the $\tau_\ell\tau_{\text{had}}$ channel. In the $\tau_{\text{had}}\tau_{\text{had}}$

channel, it is required to have statistical uncertainties below 50% for each bin. If there is no signal presented in a certain bin, that bin is required to have statistical uncertainty smaller 1%. The minimum number of events in each bin for both $\tau_\ell\tau_{\text{had}}$ and $\tau_{\text{had}}\tau_{\text{had}}$ channel is restricted to be above the thresholds for $\tau_\ell\tau_{\text{had}}$ and $\tau_{\text{had}}\tau_{\text{had}}$ channels respectively. (10 for $\tau_\ell\tau_{\text{had}}$ channel and 5 for $\tau_{\text{had}}\tau_{\text{had}}$ channel)

To assess the compatibility of the SM background-only hypothesis with the observations in the signal regions, a profile likelihood ratio test is performed. All systematic uncertainties and statistical uncertainties coming from signal and background processes are implemented as deviations from the nominal model scaled by nuisance parameters that are profiled in the fit, as well as the normalization factor for $Z+bb, bc, cc$ background processes by including the $Z \to \mu\mu$+2b-jets control region as a single bin in the fit. The number of observed data events is found to be compatible with the fitting number of background events. No significant excess over the expected background from SM processes is observed, thus we perform a profile likelihood ratio test following the CLs[106] prescription using the data to set upper limits on resonant and non-resonant Higgs pair production at 95% C.L.

The BDT output score responses for the 2HDM heavy Higgs search are shown in Fig 10.1 and Fig 10.2 in $\tau_\ell\tau_{\text{had}}$ channel for the SLT and LTT categories. 300 GeV, 500 GeV and 1000 GeV(800 GeV) signal BDT score are selected for SLT(LTT) category to show as these three masses could basically represent low mass, medium mass and high mass range signal BDT responses. Fig 10.3 and Fig 10.4 are the BDT responses of different RSG signals with the coupling constant $k/\bar{M}_{PI}$ equaling 1 and 2 in the $\tau_\ell\tau_{\text{had}}$ channel for SLT and LTT categories. All the binnings are optimized as described. BDT score responses in the $\tau_{\text{had}}\tau_{\text{had}}$ channel are shown in Fig 10.5 and Fig 10.6 for 2HDM and RSG model respectively. 300 GeV, 500 GeV and 1000 GeV signals are chosen to show for both 2HDM and RSG signals. Different coupling constant $k/\bar{M}_{PI}$ = 1 and 2 are showed for RSG model in $\tau_{\text{had}}\tau_{\text{had}}$ channel. For the Non-resonant SM

Higgs pair-production, Fig 10.7 and Fig 10.8 give the BDT output score responses with and without the finite top mass correction in the SLT and LTT categories in $\tau_\ell\tau_{\text{had}}$ and $\tau_{\text{had}}\tau_{\text{had}}$ channel. All these BDT score are using the corresponding binning strategy as well, as described before for each sub channel.

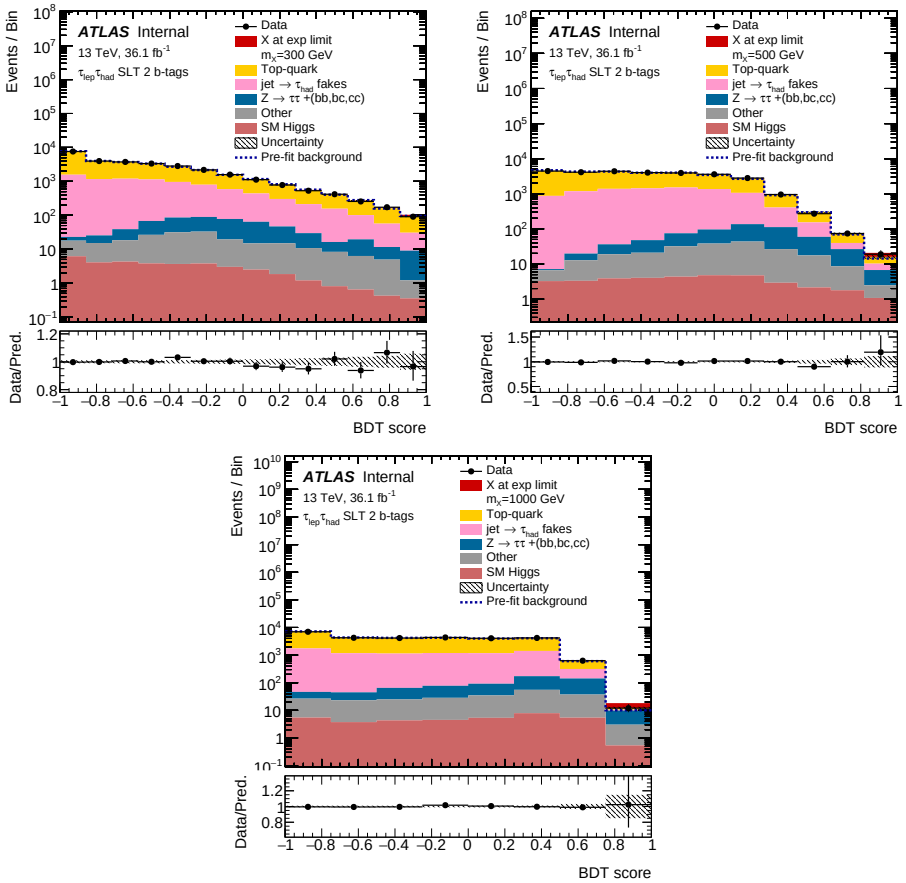

Figure 10.1: Distribution of the BDT output for 2HDM signal in the $\tau_\ell\tau_{\text{had}}$ SLT channel for resonance masses of 300 GeV(top left), 500 GeV(top right) and 1000 GeV(bottom), using the optimized binning and after performing the final fit. A background-only hypothesis is assumed.

The expected number of signals and background events in the 2 b-tag signal regions after the fit assuming background-only hypothesis are given in Table 10.1

The result for the resonance searches are presented as exclusion limits on the hh-production cross-section with respect to the resonance mass. The expected limits for 2HDM and RS Graviton signal models are shown in Fig 10.9 and Fig 10.10 for

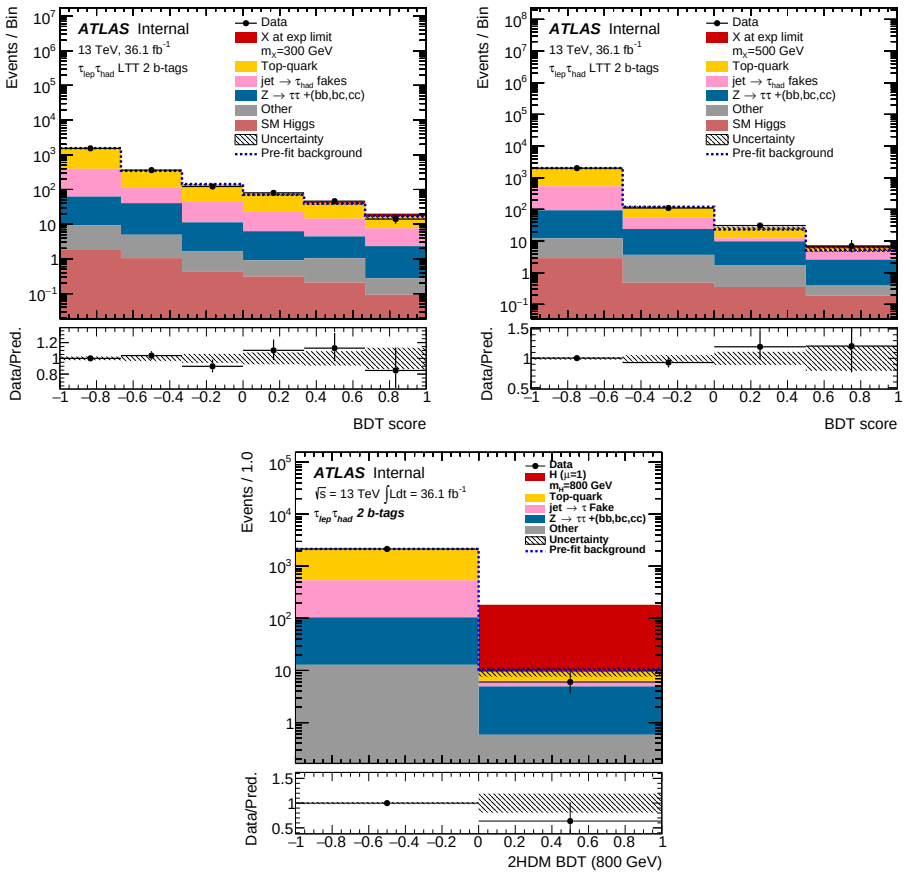

Figure 10.2: Distribution of the BDT output for 2HDM signal in the $\tau_\ell\tau_{\text{had}}$ LTT channel for resonance masses of 300 GeV(top left), 500 GeV(top right) and 800 GeV(bottom), using the optimized binning and after performing the final fit. A background-only hypothesis is assumed.

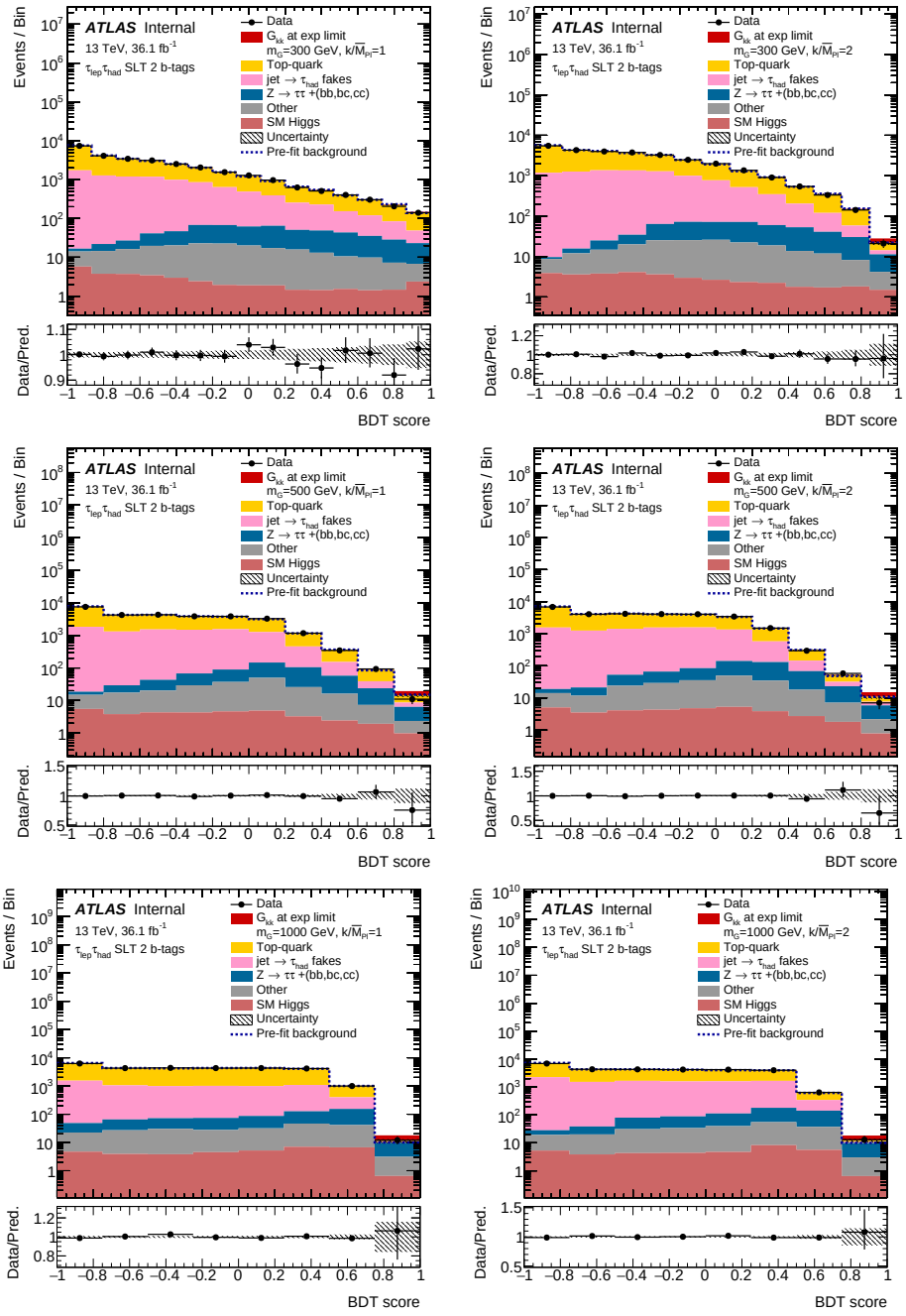

Figure 10.3: Distribution of the BDT output for RS graviton c=1(left) and c=2 (right) signals in the $\tau_\ell\tau_{\text{had}}$ SLT channel for resonance masses of 300 GeV (top), 500 GeV (middle) and 1000 GeV (bottom), using the optimized binning and after performing the final fit. A background-only hypothesis is assumed.

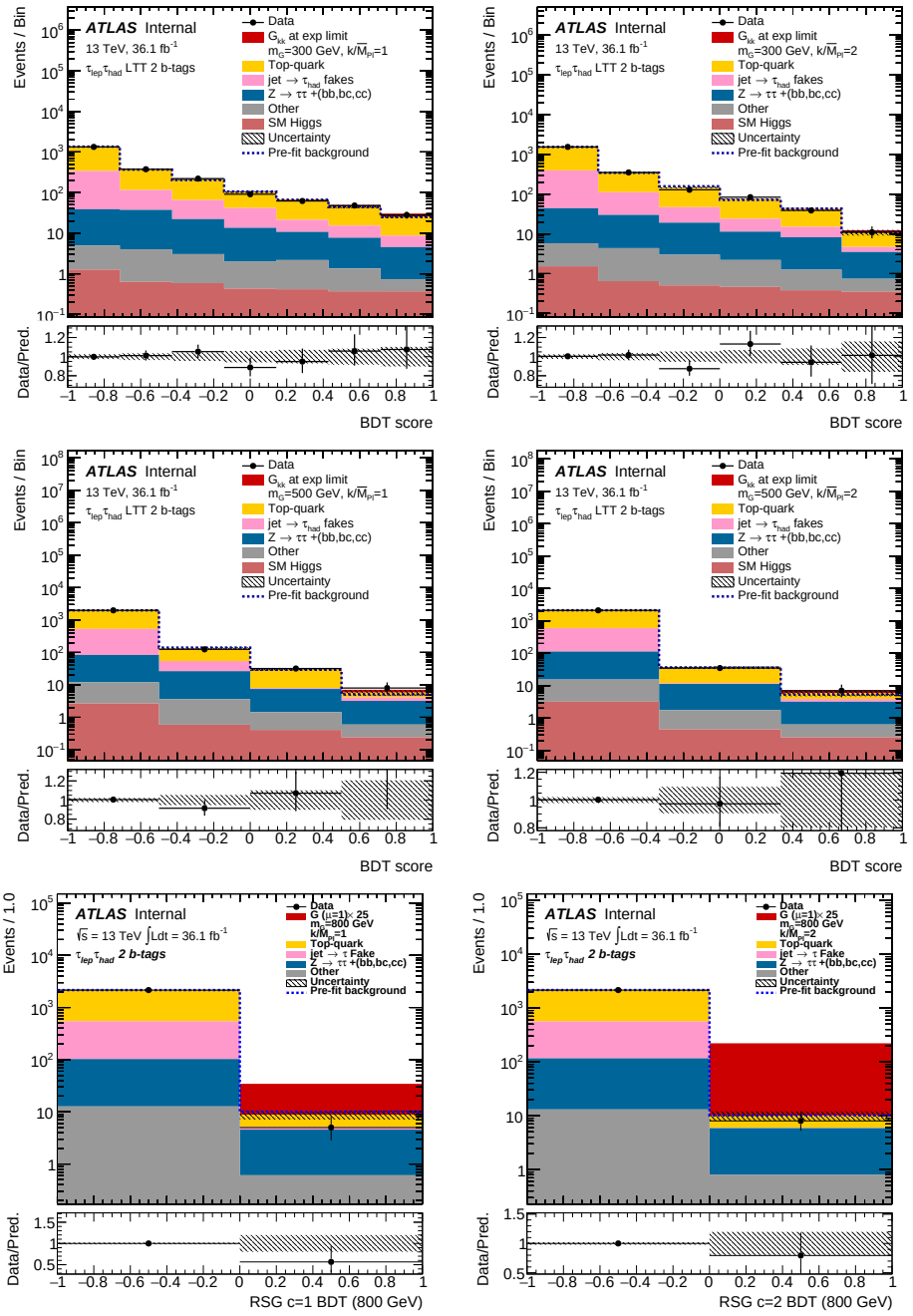

Figure 10.4: Distribution of the BDT output for RS graviton c=1(left) and c=2 (right) signals in the $\tau_\ell\tau_{\text{had}}$ LTT channel for resonance masses of 300 GeV (top), 500 GeV (middle) and 800 GeV (bottom), using the optimized binning and after performing the final fit. A background-only hypothesis is assumed.

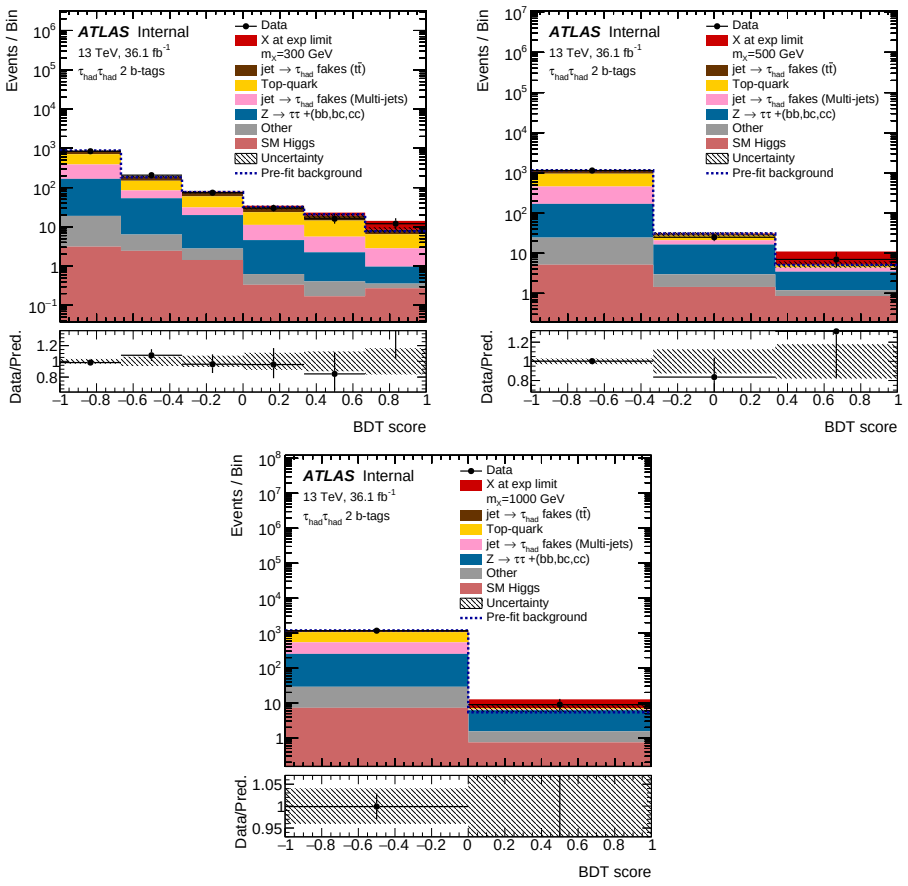

Figure 10.5: Distribution of the BDT output for 2HDM signal in the $\tau_{\text{had}}\tau_{\text{had}}$ channel for resonance masses of 300 GeV(top left), 500 GeV(top right) and 1000 GeV(bottom), using the optimized binning and after performing the final fit. A background-only hypothesis is assumed.

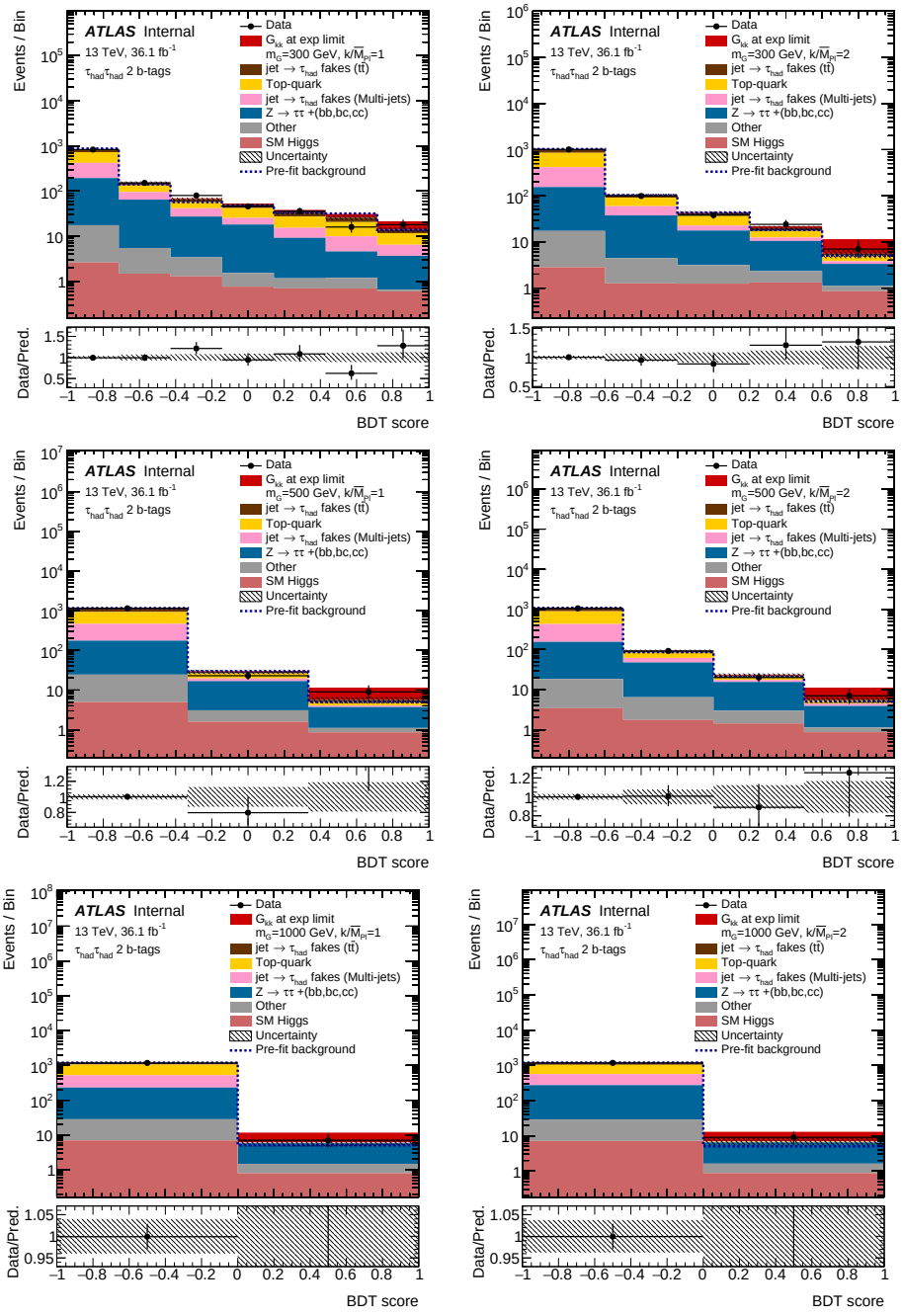

Figure 10.6: Distribution of the BDT output for RS graviton c=1(left) and c=2 (right) signals in the $\tau_{\text{had}}\tau_{\text{had}}$ channel for resonance masses of 300 GeV (top), 500 GeV (middle) and 1000 GeV (bottom), using the optimized binning and after performing the final fit. A background-only hypothesis is assumed.

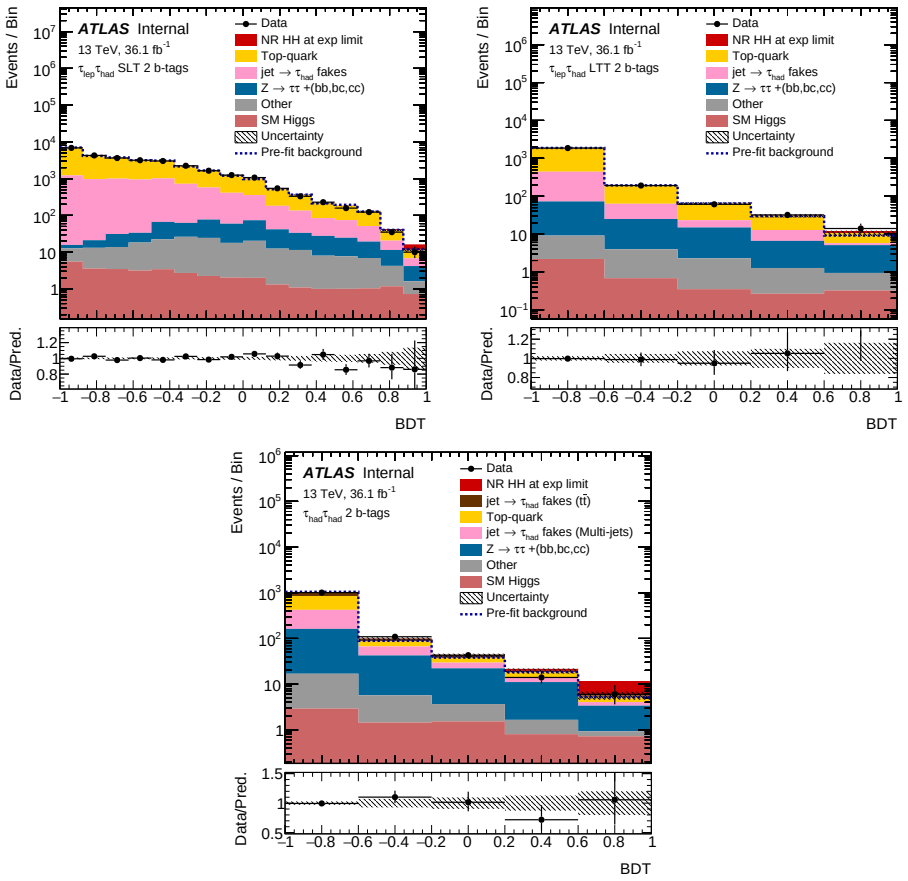

Figure 10.7: Distribution of the BDT score for the non-resonant Higgs pair-production assuming finite top mass in SLT channel(top left), LTT channel(top right) and $\tau_{\text{had}}\tau_{\text{had}}$ channel(bottom), using the optimized binning and after performing the final fit with full systematic uncertainties.

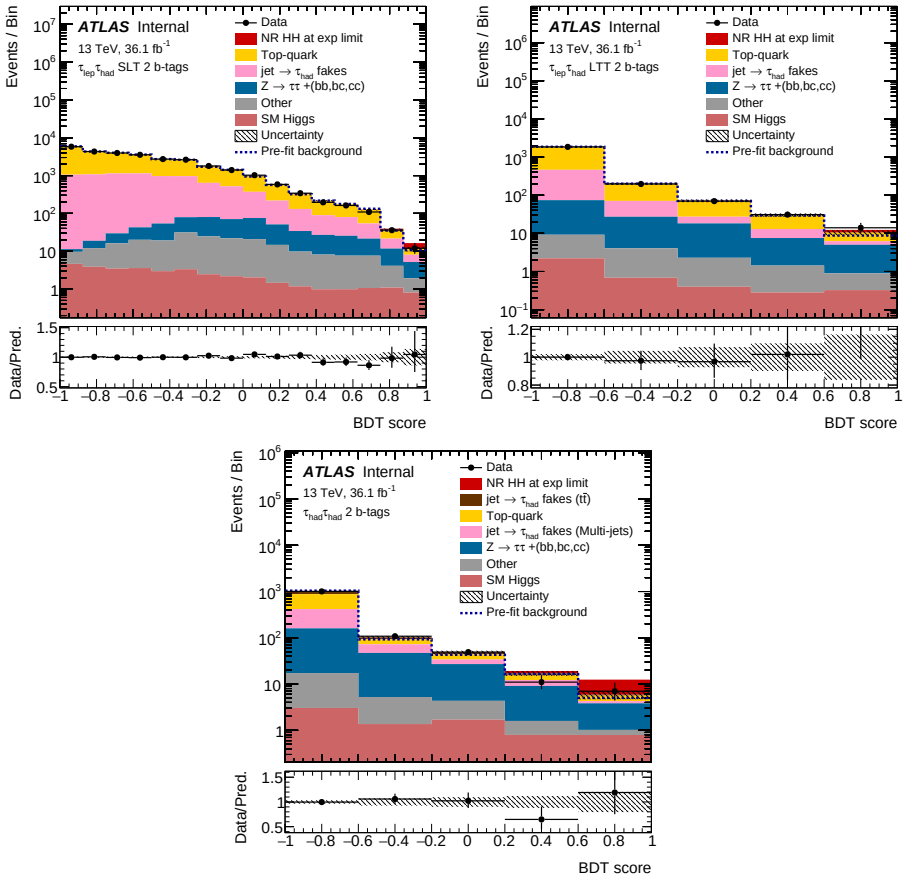

Figure 10.8: Distribution of the BDT score for the non-resonant Higgs pair-production without finite top mass correction in SLT channel(top left), LTT channel(top right) and $\tau_{\text{had}}\tau_{\text{had}}$ channel(bottom), using the optimized binning and after performing the final fit with full systematic uncertainties.

	$\tau_\ell\tau_{\text{had}}$ channel		$\tau_{\text{had}}\tau_{\text{had}}$ channel
	(SLT)	(LTT)	
$t\bar{t}$	17800 ± 1100	1475 ± 94	360± 100
Single top	1130 ± 110	72.9 ± 7.6	39.7 ± 5.9
QCD fakes	-	-	294 ± 57
$t\bar{t}$fakes	-	-	160 ± 120
Fakes	9000 ± 1100	475 ± 76	-
$Z \to \tau\tau + (cc, bc, bb)$	416 ± 97	117 ± 28	291 ± 91
Other (W + Z + DY + VV)	197 ± 32	14.5 ± 2.3	22.9 ± 5.9
SM Higgs	37.6 ± 10	4.1 ± 1	8.2 ± 2.1
Total Background	28610 ± 180	2159 ± 46	1178 ± 40
Data	28612	2161	1180
$G(300, c = 1) \to bb\tau\tau$	23.6 ± 3.7	7.5 ± 1.2	13.1 ± 2.6
$G(500, c = 1) \to bb\tau\tau$	42.4 ± 6.4	9.9 ± 1.5	36.3 ± 7
$G(1000/800(LTT), c = 1) \to bb\tau\tau$	2.56 ± 0.4	1.06 ± 0.16	2.11 ± 0.43
$G(300, c = 2) \to bb\tau\tau$	327 ± 50	82 ± 13	240 ± 46
$G(500, c = 2) \to bb\tau\tau$	193 ± 29	39.7 ± 6.1	187 ± 36
$G(1000/800(LTT), c = 2) \to bb\tau\tau$	8.6 ± 1.3	3.63 ± 0.56	7.9 ± 1.6
$H(300) \to bb\tau\tau$	39.1 ± 6.3	11.8 ± 1.9	17.9 ± 3.6
$H(500) \to bb\tau\tau$	3.41 ± 0.52	0.88 ± 0.13	2.84 ± 0.54
$H(1000/800(LTT)) \to bb\tau\tau$	0.0267 ± 0.0041	0.0228 ± 0.0035	0.0222 ± 0.0044
Non-res. hh	1.04 ± 0.14	0.290 ± 0.043	0.79 ± 0.15
Non-res.(top mass RW) hh	0.99 ± 0.13	0.225 ± 0.033	0.75 ± 0.14

Table 10.1: Post-fit expected number of signal and background events and observed number of data events after applying the selection criteria and requiring exactly 2 b-jets and assuming a background-only hypothesis. The Fake background includes all processes in which the hadronic τ is faked by a jet. The $t\bar{t}$ background includes events with true taus or hadronic τs faked by leptons (very small). The category 'Other' includes contributions from W+jets, $Z/\gamma^* \to \ell\ell$+jets, and di-boson processes

the $\tau_\ell\tau_{\rm had}$ and $\tau_{\rm had}\tau_{\rm had}$ channels. The $\tau_\ell\tau_{\rm had}$ channel result is shown respectively in SLT and LTT categories. Different coupling constant $k/\bar{M}_{PI}$=1 and 2 for RSG expected limit are shown. The RSG $k/\bar{M}_{PI}$=1 has less signal mass points than the RSG $k/\bar{M}_{PI}$=2 and 2HDM signals. This is because we requested RSG $k/\bar{M}_{PI}$=1 signals much earlier than we decided to have a finer gap between the resonant signals. We have tried to reweight the RSG $k/\bar{M}_{PI}$=2 signals to make up the RSG $k/\bar{M}_{PI}$=1 intermediate mass points. It turned out to be not working so well. So we decided to not have the intermediate mass points for the RSG c=1 signals. The upper limits for LTT stopped at 800 GeV because of the fact that lepton-tau trigger events are not sensitive to high mass regions. The $\tau_{\rm had}\tau_{\rm had}$ channel result is shown in Fig 10.10. Similar to $\tau_\ell\tau_{\rm had}$ channel, different results are presented for different coupling constants c=1 and c=2 for RSG model.

The combined results of searches in all channels for resonant HH production are presented in Fig 10.11 as exclusion limits on the cross-section times branching ratio to $bb\tau\tau$ with respect to the resonance mass. The expected and observed limits for 2HDM and G_{KK} signal models are both shown. The 2HDM scalar resonances X are interpreted in the hMSSM with tanβ = 2, where tanβ is the ratio of the vacuum expectation values of the scalar doublets. Result shows that middle mass range, eg. $305 < m_X < 402$ GeV are excluded at 95% CL. In the RS-Graviton model, gravitons with mass between mass range $325 < m_{G_{KK}} < 885$ GeV are excluded for $k/\bar{M}_{PI} = 1$ at 95% CL. While if assuming $k/\bar{M}_{PI} = 2$ in the RS-Graviton model, the gravitons are excluded in almost all mass range from 260 GeV to 1000 GeV. Above about 600 GeV, the limits are not sensitive to the coupling constant $k/\bar{M}_{PI}$ in the RSG model. The limits of the resonant HH shown here are significantly improved compared with previous results in the $bb\tau\tau$ channel and competitive with limits obtained in other HH channels.

The non-resonant results are presented with upper limits on the cross section

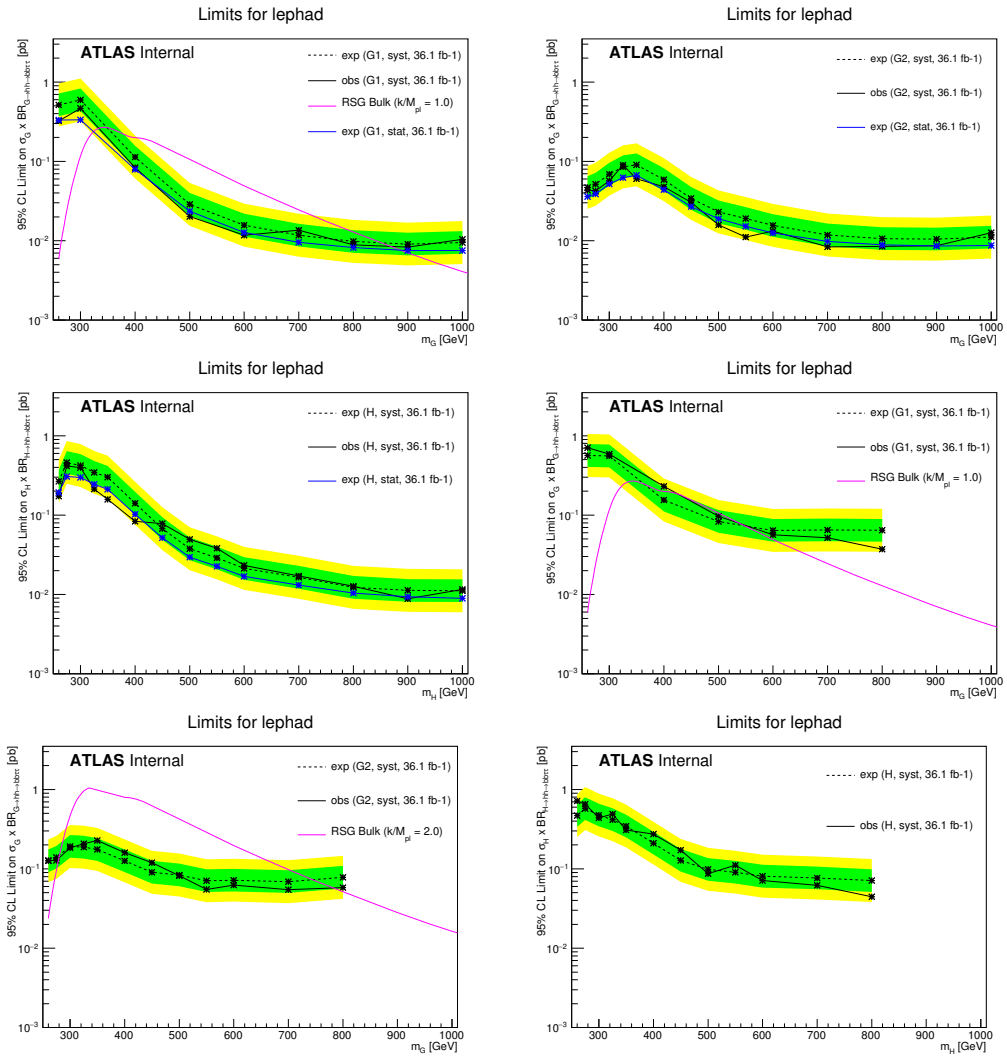

Figure 10.9: Expected limits at 95% C.L. on the cross-sections of the RS $G \to hh$,c=1 (top left), RS $G \to hh$,c=2 (top right) and 2HDM $H \to hh$ (middle left) for the $\tau_\ell\tau_{\text{had}}$ channel SLT category; RS $G \to hh$,c=1 (middle right), RS $G \to hh$,c=2 (bottom left) and 2HDM $H \to hh$ (bottom right) for the LTT category.

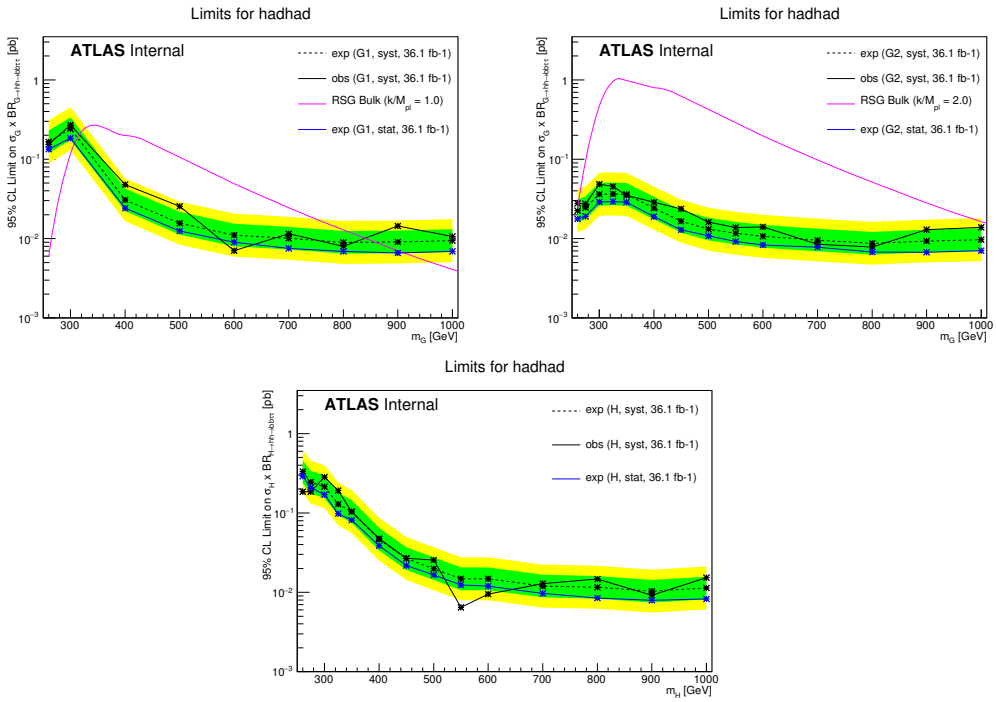

Figure 10.10: Expected limits at 95% C.L. on the cross-sections of the RS $G \to hh$,c=1 (left), RS $G \to hh$,c=2 (right) and 2HDM $H \to hh$ (bottom) for the $\tau_{\text{had}}\tau_{\text{had}}$ channel.

for non-resonant HH production times the $HH \to bb\tau\tau$ branching ratio. The ratio between itself and the SM prediction is also calculated and shown. The non-resonant results are shown in Table 10.2. The observed(expected) limit combining all $\tau_\ell\tau_{\text{had}}$ and $\tau_{\text{had}}\tau_{\text{had}}$ channels for non-resonant HH production is 30.9 fb(36.0 fb), which is 12.7(14.8) times the SM prediction. This is the result with the finite top mass reweighting correction. The non-resonant HH result from this $bb\tau\tau$ channel is the best result for HH non-resonant pair production so far among all the channels from all different experiments.

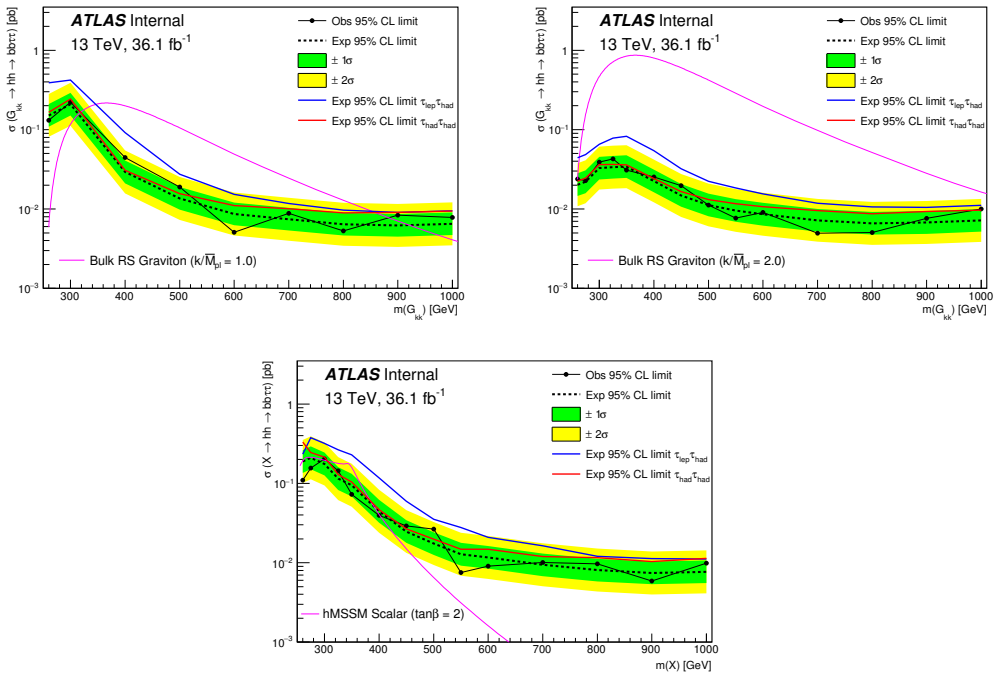

Figure 10.11: Observed and expected limits at 95% CL on the cross-section of $G_{KK} \to HH$(top) for $k/\bar{M}_{PI} = 1$(left) and $k/\bar{M}_{PI} = 2$(right) and the $X \to HH$(bottom) processes combining all $\tau_\ell\tau_{\text{had}}$ and $\tau_{\text{had}}\tau_{\text{had}}$ channels. The expected cross-section for the hMSSM scalar X production and the RS graviton production with $k/\bar{M}_{PI}$= 1.0 or 2.0 are also shown in the respective plots

Table 10.2: Upper limits on the production cross section times the $HH \to bb\tau\tau$ branching ratio for NR HH at 95% CL and their ratio to the SM prediction.

		Observed	-2σ	-1σ	Expected	+1σ	+2σ
$\tau_\ell\tau_{\text{had}}$	$\sigma(HH \to bb\tau\tau)$ [fb]	57.3	37.1	49.9	69.2	96.3	129
	$\sigma/\sigma_{\text{SM}}$	23.5	15.2	20.5	28.4	39.5	53.0
$\tau_{\text{had}}\tau_{\text{had}}$	$\sigma(HH \to bb\tau\tau)$ [fb]	39.9	22.7	30.5	42.4	59.0	79.0
	$\sigma/\sigma_{\text{SM}}$	16.4	9.3	12.5	17.4	24.2	32.4
Combination	$\sigma(HH \to bb\tau\tau)$ [fb]	30.9	19.3	26.0	36.0	50.1	67.2
	$\sigma/\sigma_{\text{SM}}$	12.7	7.9	10.7	14.8	20.6	27.6

CHAPTER XI

Conclusions

A search for resonant and non-resonant di-Higgs pair production is conducted in the $bb\tau\tau$ final state channel using the year 2015+2016 data collected by ATLAS detector with total integrated luminosity 36.1 fb^{-1} delivered by the LHC at $\sqrt{s} = 13$ TeV. This Run II data analysis added an extra $\tau_{\text{had}}\tau_{\text{had}}$ sub-channel and an extra lepton-τ trigger category compared with the Run I analysis, which give the analysis more statistics. Adding the lepton-τ trigger category events improves the final result of the resonant BSM particle search in the low mass range by about 50%. Instead of using a cut-based data analysis strategy, this data analysis uses the Boosted Decision Tree(BDT)[21, 71] machine learning algorithm to gain extraordinary discriminant power between signals and backgrounds, which improves the result by roughly overall 50% in all channels. These novel features of this data analysis make it stand out from all the di-Higgs final state analysis on both ATLAS[1] and CMS[8] detectors. The non-resonant Higgs pair production result excludes an enhancement of the SM expectation by more than a factor of 12.7 at 95% C.L, which is the best sensitivity physicists have reached so far. There is no evidence observed from 260 GeV to 1000 GeV range supporting the existence of the scalar heavy Higgs in 2HDM[6, 7] and a spin-2 Kaluza-Klein graviton G_{kk} in Randall-Sundrum Graviton model[3, 4, 5]. Thus an upper limit is placed on the corresponding production cross section times the $bb\tau\tau$

final state branching ratio. The results are interpreted in a simplified minimal supersymmetric model, hMSSM[107, 108] and the RS Graviton model. In the hMSSM with the light CP-even Higgs boson mass fixed at 125 GeV, the mass range 305 GeV through 402 GeV is excluded at 95% C.L for $\tan\beta = 2$, where $\tan\beta$ is the ratio of the VEVs between the two Higgs doublets. RS Gravitons are excluded at 95% CL from 325 GeV through 885 GeV with coupling constant $k/\bar{M}_{Pl} = 1$, as well as, 260 GeV through 1000 GeV with coupling constant $k/\bar{M}_{Pl} = 2$.

APPENDIX

Cross Section Information of Monte Carlo Samples Used in This Analysis

The cross-section information used to normalize the MC processes could be found in this section. Table A.1 and Table A.2 are lists of Monte Carlo signal and background samples of different processes used in this analysis with their DataSet ID, effective cross sections and Names.

DSID	Effective xsec [pb] (xsec*k-factor*FE)	Name
Signal		
Non res		
342622	0.025221 * 1.0 * 0.22653	aMcAtNloHerwigppEG_UEEE5_CTEQ6L1_CT10ME_hh_ttbb_lh
342623	0.025198 * 1.0 * 0.20969	aMcAtNloHerwigppEG_UEEE5_CTEQ6L1_CT10ME_hh_ttbb_hh
Graviton HadHad		
303351	2.72E-01 * 1.0 * 0.057289 * 0.414	RS_G_hh_bbtt_hh_c10_M260 MadGraphPythia8EvtGen_A14NNPDF23LO_RS_G_hh_bbtt_hh_c10_M260
303352	1.32 * 1.0 * 0.057229 * 0.414	RS_G_hh_bbtt_hh_c10_M300 MadGraphPythia8EvtGen_A14NNPDF23LO_RS_G_hh_bbtt_hh_c10_M300
303353	1.91 * 1.0 * 0.060278 * 0.414	RS_G_hh_bbtt_hh_c10_M400 MadGraphPythia8EvtGen_A14NNPDF23LO_RS_G_hh_bbtt_hh_c10_M400
303354	8.90E-01 * 1.0 * 0.062730 * 0.414	RS_G_hh_bbtt_hh_c10_M500 MadGraphPythia8EvtGen_A14NNPDF23LO_RS_G_hh_bbtt_hh_c10_M500
303355	4.10E-01 * 1.0 * 0.064623 * 0.414	RS_G_hh_bbtt_hh_c10_M600 MadGraphPythia8EvtGen_A14NNPDF23LO_RS_G_hh_bbtt_hh_c10_M600
303356	2.01E-01 * 1.0 * 0.066336 * 0.414	RS_G_hh_bbtt_hh_c10_M700 MadGraphPythia8EvtGen_A14NNPDF23LO_RS_G_hh_bbtt_hh_c10_M700
303357	1.05E-01 * 1.0 * 0.067214 * 0.414	RS_G_hh_bbtt_hh_c10_M800 MadGraphPythia8EvtGen_A14NNPDF23LO_RS_G_hh_bbtt_hh_c10_M800
303358	5.80E-02 * 1.0 * 0.068266 * 0.414	RS_G_hh_bbtt_hh_c10_M900 MadGraphPythia8EvtGen_A14NNPDF23LO_RS_G_hh_bbtt_hh_c10_M900
303359	3.40E-02 * 1.0 * 0.069159 * 0.414	RS_G_hh_bbtt_hh_c10_M1000 MadGraphPythia8EvtGen_A14NNPDF23LO_RS_G_hh_bbtt_hh_c10_M1000
Graviton LepHad		
303395	0.2719 * 1.0 * 4.7893E-02 * 0.414	Ghhbbtautau260c10 MGPy8EG_A14NNPDF23LO_RS_G_hh_bbtt_lh_c10_M260
303396	1.3199 * 1.0 * 4.7993E-02 * 0.414	Ghhbbtautau300c10 MGPy8EG_A14NNPDF23LO_RS_G_hh_bbtt_lh_c10_M300
303397	1.901 * 1.0 * 5.3828E-02 * 0.414	Ghhbbtautau400c10 MGPy8EG_A14NNPDF23LO_RS_G_hh_bbtt_lh_c10_M400
303398	0.8924 * 1.0 * 5.8507E-02 * 0.414	Ghhbbtautau500c10 MGPy8EG_A14NNPDF23LO_RS_G_hh_bbtt_lh_c10_M500
303399	0.4104 * 1.0 * 6.1981E-02 * 0.414	Ghhbbtautau600c10 MGPy8EG_A14NNPDF23LO_RS_G_hh_bbtt_lh_c10_M600
303400	0.20148* 1.0 * 6.4597E-02 * 0.414	Ghhbbtautau700c10 MGPy8EG_A14NNPDF23LO_RS_G_hh_bbtt_lh_c10_M700
303401	0.10549* 1.0 * 6.6660E-02 * 0.414	Ghhbbtautau800c10 MGPy8EG_A14NNPDF23LO_RS_G_hh_bbtt_lh_c10_M800
303402	0.05835* 1.0 * 6.8206E-02 * 0.414	Ghhbbtautau900c10 MGPy8EG_A14NNPDF23LO_RS_G_hh_bbtt_lh_c10_M900
303403	0.03368* 1.0 * 6.9496E-02 * 0.414	Ghhbbtautau1000c10 MGPy8EG_A14NNPDF23LO_RS_G_hh_bbtt_lh_c10_M1000
2HDM HadHad		
342635	440.38 * 1.0* 5.4777E-02 * 0.414	Hhhbbtautau260MGPy8EG_A14NNPDF23LO_X260tohh_bbtautau_hadhad
342636	637.2 * 1.0* 5.5548E-02 * 0.414	Hhhbbtautau300MGPy8EG_A14NNPDF23LO_X300hh_bbtautau_hadhad
342637	646.17 * 1.0* 5.8067E-02 * 0.414	Hhhbbtautau400MGPy8EG_A14NNPDF23LO_X400hh_bbtautau_hadhad
342638	276.9 * 1.0* 6.0078E-02 * 0.414	Hhhbbtautau500MGPy8EG_A14NNPDF23LO_X500hh_bbtautau_hadhad
342639	107.99 * 1.0* 6.1877E-02 * 0.414	Hhhbbtautau600MGPy8EG_A14NNPDF23LO_X600hh_bbtautau_hadhad
342640	44.137 * 1.0* 6.3132E-02 * 0.414	Hhhbbtautau700MGPy8EG_A14NNPDF23LO_X700hh_bbtautau_hadhad
342641	19.26 * 1.0* 6.4319E-02 * 0.414	Hhhbbtautau800MGPy8EG_A14NNPDF23LO_X800hh_bbtautau_hadhad
342642	8.9373 * 1.0* 6.5253E-02 * 0.414	Hhhbbtautau900MGPy8EG_A14NNPDF23LO_X900hh_bbtautau_hadhad
342643	4.3826 * 1.0* 6.5969E-02 * 0.414	Hhhbbtautau1000MGPy8EG_A14NNPDF23LO_X1000hh_bbtautau_hadhad
2HDM LepHad		
342626	441.86* 1.0* 5.4790E-02 * 0.414	Hhhbbtautau260MGPy8EG_A14NNPDF23LO_X260tohh_bbtautau_lephad
342627	634.98* 1.0* 4.5628E-02 * 0.414	Hhhbbtautau300MGPy8EG_A14NNPDF23LO_X300hh_bbtautau_lephad
342628	646.17* 1.0* 5.0754E-02 * 0.414	Hhhbbtautau400MGPy8EG_A14NNPDF23LO_X400hh_bbtautau_lephad
342629	276.9 * 1.0* 5.4790E-02 * 0.414	Hhhbbtautau500MGPy8EG_A14NNPDF23LO_X500hh_bbtautau_lephad
342630	107.99* 1.0* 5.7805E-02 * 0.414	Hhhbbtautau600MGPy8EG_A14NNPDF23LO_X600hh_bbtautau_lephad
342631	44.137* 1.0* 6.0386E-02 * 0.414	Hhhbbtautau700MGPy8EG_A14NNPDF23LO_X700hh_bbtautau_lephad
342632	19.26 * 1.0* 6.2507E-02 * 0.414	Hhhbbtautau800MGPy8EG_A14NNPDF23LO_X800hh_bbtautau_lephad
342633	8.9208* 1.0* 6.3971E-02 * 0.414	Hhhbbtautau900MGPy8EG_A14NNPDF23LO_X900hh_bbtautau_lephad
342634	4.3747* 1.0* 6.5501E-02 * 0.414	Hhhbbtautau1000MGPy8EG_A14NNPDF23LO_X1000hh_bbtautau_lephad

Table A.1: The list of Signal Monte Carlo samples. Each column shows Dataset id, effective cross section from product of cross section, branching ratio, k-factor, filter efficiency and the Dataset name

DSID	Effective xsec [pb] (xsec*BR*FE)	Name
Backgrounds		
DiBoson		
361091	24.885 * 0.91 * 1.0000E+00	WW_improved Sherpa_CT10_WplvWmqq_SHv21_improved
361092	24.857 * 0.91 * 1.0000E+00	WW_improved Sherpa_CT10_WpqqWmlv_SHv21_improved
361093	11.494 * 0.91 * 1.0000E+00	WZ_improved Sherpa_CT10_WlvZqq_SHv21_improved
361094	3.4234 * 0.91 * 1.0000E+00	WZ_improved Sherpa_CT10_WqqZll_SHv21_improved
361095	6.777 * 0.91 * 1.0000E+00	WZ_improved Sherpa_CT10_WqqZvv_SHv21_improved
361096	16.445 * 0.91 * 1.4307E-01	ZZ_improved Sherpa_CT10_ZqqZll_SHv21_improved
Z+jets		
364100	1.9830E+03 * 0.9751 * 8.2210E-01	Sherpa_221_NNPDF30NNLO_Zmumu_MAXHTPTV0_70_CVetoBVeto
364101	1.9784E+03 * 0.9751 * 1.1308E-01	Sherpa_221_NNPDF30NNLO_Zmumu_MAXHTPTV0_70_CFilterBVeto
364102	1.9822E+03 * 0.9751 * 6.4161E-02	Sherpa_221_NNPDF30NNLO_Zmumu_MAXHTPTV0_70_BFilter
364103	1.0892E+02 * 0.9751 * 6.8873E-01	Sherpa_221_NNPDF30NNLO_Zmumu_MAXHTPTV70_140_CVetoBVeto
364104	1.0942E+02 * 0.9751 * 1.8596E-01	Sherpa_221_NNPDF30NNLO_Zmumu_MAXHTPTV70_140_CFilterBVeto
364105	1.0891E+02 * 0.9751 * 1.1375E-01	Sherpa_221_NNPDF30NNLO_Zmumu_MAXHTPTV70_140_BFilter
364106	3.9878E+01 * 0.9751 * 6.0899E-01	Sherpa_221_NNPDF30NNLO_Zmumu_MAXHTPTV140_280_CVetoBVeto
364107	3.9795E+01 * 0.9751 * 2.3308E-01	Sherpa_221_NNPDF30NNLO_Zmumu_MAXHTPTV140_280_CFilterBVeto
364108	3.9890E+01 * 0.9751 * 1.3769E-01	Sherpa_221_NNPDF30NNLO_Zmumu_MAXHTPTV140_280_BFilter
364109	8.5375 * 0.9751 * 5.5906E-01	Sherpa_221_NNPDF30NNLO_Zmumu_MAXHTPTV280_500_CVetoBVeto
364110	8.5403 * 0.9751 * 2.6528E-01	Sherpa_221_NNPDF30NNLO_Zmumu_MAXHTPTV280_500_CFilterBVeto
364111	8.4932 * 0.9751 * 1.7559E-01	Sherpa_221_NNPDF30NNLO_Zmumu_MAXHTPTV280_500_BFilter
364112	1.7881 * 0.9751 * 1.0000E+00	Sherpa_221_NNPDF30NNLO_Zmumu_MAXHTPTV500_1000
364113	1.4769E-01 * 0.9751 * 1.0000E+00	Sherpa_221_NNPDF30NNLO_Zmumu_MAXHTPTV1000_E_CMS
364114	1.9818E+03 * 0.9751 * 8.2106E-01	Sherpa_221_NNPDF30NNLO_Zee_MAXHTPTV0_70_CVetoBVeto
364115	1.9808E+03 * 0.9751 * 1.1295E-01	Sherpa_221_NNPDF30NNLO_Zee_MAXHTPTV0_70_CFilterBVeto
364116	1.9817E+03 * 0.9751 * 6.3809E-02	Sherpa_221_NNPDF30NNLO_Zee_MAXHTPTV0_70_BFilter
364117	1.1050E+02 * 0.9751 * 6.9043E-01	Sherpa_221_NNPDF30NNLO_Zee_MAXHTPTV70_140_CVetoBVeto
364118	1.1063E+02 * 0.9751 * 1.8382E-01	Sherpa_221_NNPDF30NNLO_Zee_MAXHTPTV70_140_CFilterBVeto
364119	1.1031E+02 * 0.9751 * 1.1443E-01	Sherpa_221_NNPDF30NNLO_Zee_MAXHTPTV70_140_BFilter
364120	4.0731E+01 * 0.9751 * 6.1452E-01	Sherpa_221_NNPDF30NNLO_Zee_MAXHTPTV140_280_CVetoBVeto
364121	4.0670E+01 * 0.9751 * 2.3044E-01	Sherpa_221_NNPDF30NNLO_Zee_MAXHTPTV140_280_CFilterBVeto
364122	4.0643E+01 * 0.9751 * 1.4966E-01	Sherpa_221_NNPDF30NNLO_Zee_MAXHTPTV140_280_BFilter
364123	8.6743 * 0.9751 * 5.6134E-01	Sherpa_221_NNPDF30NNLO_Zee_MAXHTPTV280_500_CVetoBVeto
364124	8.6711 * 0.9751 * 2.6294E-01	Sherpa_221_NNPDF30NNLO_Zee_MAXHTPTV280_500_CFilterBVeto
364125	8.6766 * 0.9751 * 1.7223E-01	Sherpa_221_NNPDF30NNLO_Zee_MAXHTPTV280_500_BFilter
364126	1.8081 * 0.9751 * 1.0000E+00	Sherpa_221_NNPDF30NNLO_Zee_MAXHTPTV500_1000
364127	1.4857E-01 * 0.9751 * 1.0000E+00	Sherpa_221_NNPDF30NNLO_Zee_MAXHTPTV1000_E_CMS
364128	1.9816E+03 * 0.9751 * 8.2142E-01	Sherpa_221_NNPDF30NNLO_Ztautau_MAXHTPTV0_70_CVetoBVeto
364129	1.9788E+03 * 0.9751 * 1.1314E-01	Sherpa_221_NNPDF30NNLO_Ztautau_MAXHTPTV0_70_CFilterBVeto
364130	1.9818E+03 * 0.9751 * 6.4453E-02	Sherpa_221_NNPDF30NNLO_Ztautau_MAXHTPTV0_70_BFilter
364131	1.1037E+02 * 0.9751 * 6.8883E-01	Sherpa_221_NNPDF30NNLO_Ztautau_MAXHTPTV70_140_CVetoBVeto
364132	1.1051E+02 * 0.9751 * 1.8290E-01	Sherpa_221_NNPDF30NNLO_Ztautau_MAXHTPTV70_140_CFilterBVeto
364133	1.1087E+02 * 0.9751 * 0.1283	Sherpa_221_NNPDF30NNLO_Ztautau_MAXHTPTV70_140_BFilter
364134	4.0781E+01 * 0.9751 * 6.0821E-01	Sherpa_221_NNPDF30NNLO_Ztautau_MAXHTPTV140_280_CVetoBVeto
364135	4.0740E+01 * 0.9751 * 2.2897E-01	Sherpa_221_NNPDF30NNLO_Ztautau_MAXHTPTV140_280_CFilterBVeto
364136	4.0761E+01 * 0.9751 * 1.3442E-01	Sherpa_221_NNPDF30NNLO_Ztautau_MAXHTPTV140_280_BFilter
W+jets		
364184	1.92E+04 * 0.9702 * 8.2000E-01	Sherpa_221_NNPDF30NNLO_Wtaunu_MAXHTPTV0_70_CVetoBVeto
364185	1.92E+04 * 0.9702 * 1.3000E-01	Sherpa_221_NNPDF30NNLO_Wtaunu_MAXHTPTV0_70_CFilterBVeto
364186	1.92E+04 * 0.9702 * 4.0000E-02	Sherpa_221_NNPDF30NNLO_Wtaunu_MAXHTPTV0_70_BFilter
364187	9.48E+02 * 0.9702 * 6.7000E-01	Sherpa_221_NNPDF30NNLO_Wtaunu_MAXHTPTV70_140_CVetoBVeto
364188	9.47E+02 * 0.9702 * 2.2000E-01	Sherpa_221_NNPDF30NNLO_Wtaunu_MAXHTPTV70_140_CFilterBVeto
364189	9.43E+02 * 0.9702 * 0.1040	Sherpa_221_NNPDF30NNLO_Wtaunu_MAXHTPTV70_140_BFilter
364190	3.39E+02 * 0.9702 * 6.0000E-01	Sherpa_221_NNPDF30NNLO_Wtaunu_MAXHTPTV140_280_CVetoBVeto
364191	3.40E+02 * 0.9702 * 2.9000E-01	Sherpa_221_NNPDF30NNLO_Wtaunu_MAXHTPTV140_280_CFilterBVeto
364192	3.40E+02 * 0.9702 * 1.2000E-01	Sherpa_221_NNPDF30NNLO_Wtaunu_MAXHTPTV140_280_BFilter
364193	7.21E+01 * 0.9702 * 5.5000E-01	Sherpa_221_NNPDF30NNLO_Wtaunu_MAXHTPTV280_500_CVetoBVeto
364194	7.20E+01 * 0.9702 * 3.2000E-01	Sherpa_221_NNPDF30NNLO_Wtaunu_MAXHTPTV280_500_CFilterBVeto
364195	7.20E+01 * 0.9702 * 1.3000E-01	Sherpa_221_NNPDF30NNLO_Wtaunu_MAXHTPTV280_500_BFilter
364196	1.50E+01 * 0.9702 * 1.0000E+00	Sherpa_221_NNPDF30NNLO_Wtaunu_MAXHTPTV500_1000
364197	1.23E+00 * 0.9702 * 1.0000E+00	Sherpa_221_NNPDF30NNLO_Wtaunu_MAXHTPTV1000_E_CMS
tt and single top		
410000	831.76* 1.0* 0.543	PowhegPythiaEvtGen_P2012_ttbar_hdamp172p5_nonallhad
410007	831.76* 1.0* 0.45618	PowhegPythiaEvtGen_P2012_ttbar_hdamp172p5_allhad
410011	43.73 * 1.0* 1.0	stopt PowhegPythiaEvtGen_P2012_singletop_tchan_lept_top
410012	25.778 * 1.0* 1.0	stopt PowhegPythiaEvtGen_P2012_singletop_tchan_lept_antitop
410013	34.009 * 1.0* 1.0	stopWt PowhegPythiaEvtGen_P2012_Wt_inclusive_top
410014	33.989* 1.0* 1.0	stopWt PowhegPythiaEvtGen_P2012_Wt_inclusive_antitop
410025	2.052* 1.0* 1.0	stops PowhegPythiaEvtGen_P2012_SingleTopSchan_noAllHad_top
410026	1.262* 1.0* 1.0	stops PowhegPythiaEvtGen_P2012_SingleTopSchan_noAllHad_antitop
ZH		
341096	0.00414 0.582 1.0	(gg) PowhegPythia8EvtGen_CT10_AZNLO_ggZH125_tautaubb
341102	0.07704 0.582 1.0	(qq) Pythia8EvtGen_A14NNPDF23LO_ZllH125_bb
341934	8.34669e-3 1.0 1.0	(qq) Pythia8EvtGen_A14NNPDF23LO_ZbbH125tautau

Table A.2: The list of Background Monte Carlo samples. Each column shows Dataset id, effective cross section from product of cross section, branching ratio, k-factor, filter efficiency and the Dataset name

BIBLIOGRAPHY

BIBLIOGRAPHY

[1] G. Aad et al. The ATLAS Experiment at the CERN Large Hadron Collider. *JINST*, 3:S08003, 2008.

[2] Lyndon Evans and Philip Bryant. Lhc machine. *Journal of Instrumentation*, 3(08):S08001, 2008.

[3] Kaustubh Agashe, Hooman Davoudiasl, Gilad Perez, and Amarjit Soni. Warped Gravitons at the LHC and Beyond. *Phys. Rev.*, D76:036006, 2007.

[4] A. Liam Fitzpatrick, Jared Kaplan, Lisa Randall, and Lian-Tao Wang. Searching for the Kaluza-Klein Graviton in Bulk RS Models. *JHEP*, 09:013, 2007.

[5] Lisa Randall and Raman Sundrum. A Large mass hierarchy from a small extra dimension. *Phys. Rev. Lett.*, 83:3370–3373, 1999.

[6] G. C. Branco, P. M. Ferreira, L. Lavoura, M. N. Rebelo, Marc Sher, and Joao P. Silva. Theory and phenomenology of two-Higgs-doublet models. *Phys. Rept.*, 516:1–102, 2012.

[7] T. D. Lee. A theory of spontaneous t violation. *Phys. Rev. D*, 8:1226–1239, Aug 1973.

[8] S. Chatrchyan et al. The CMS Experiment at the CERN LHC. *JINST*, 3:S08004, 2008.

[9] Georges Aad et al. Observation of a new particle in the search for the Standard Model Higgs boson with the ATLAS detector at the LHC. *Phys. Lett.*, B716:1–29, 2012.

[10] Serguei Chatrchyan et al. Observation of a new boson at a mass of 125 GeV with the CMS experiment at the LHC. *Phys. Lett.*, B716:30–61, 2012.

[11] F. Englert and R. Brout. Broken symmetry and the mass of gauge vector mesons. *Phys. Rev. Lett.*, 13:321–323, Aug 1964.

[12] Peter W. Higgs. Broken symmetries and the masses of gauge bosons. *Phys. Rev. Lett.*, 13:508–509, Oct 1964.

[13] G. S. Guralnik, C. R. Hagen, and T. W. B. Kibble. Global conservation laws and massless particles. *Phys. Rev. Lett.*, 13:585–587, Nov 1964.

[14] T. W. B. Kibble. Symmetry breaking in non-abelian gauge theories. *Phys. Rev.*, 155:1554–1561, Mar 1967.

[15] P.W. Higgs. Broken symmetries, massless particles and gauge fields. *Physics Letters*, 12(2):132 – 133, 1964.

[16] Georges Aad et al. Combined Measurement of the Higgs Boson Mass in pp Collisions at $\sqrt{s} = 7$ and 8 TeV with the ATLAS and CMS Experiments. *Phys. Rev. Lett.*, 114:191803, 2015.

[17] D. de Florian et al. Handbook of LHC Higgs Cross Sections: 4. Deciphering the Nature of the Higgs Sector. 2016.

[18] S. Borowka, N. Greiner, G. Heinrich, S. P. Jones, M. Kerner, J. Schlenk, U. Schubert, and T. Zirke. Higgs Boson Pair Production in Gluon Fusion at Next-to-Leading Order with Full Top-Quark Mass Dependence. *Phys. Rev. Lett.*, 117(1):012001, 2016. [Erratum: Phys. Rev. Lett.117,no.7,079901(2016)].

[19] David M. Morse. Latest results on di-Higgs boson production with CMS. 2017.

[20] Georges Aad et al. Searches for Higgs boson pair production in the $hh \to bb\tau\tau, \gamma\gamma WW^*, \gamma\gamma bb, bbbb$ channels with the ATLAS detector. *Phys. Rev.*, D92:092004, 2015.

[21] Leo Breiman, Jerome Friedman, Charles J. Stone, and R.A. Olshen. *Classification and Regression Trees (Wadsworth Statistics/Probability)*. Chapman and Hall/CRC, 1984.

[22] Peter W. Higgs. Spontaneous symmetry breakdown without massless bosons. *Phys. Rev.*, 145:1156–1163, May 1966.

[23] W. N. Cottingham. *An introduction to the standard model of particle physics*. Cambridge University Press, Cambridge, 2007.

[24] Jonathan Grigo, Jens Hoff, Kirill Melnikov, and Matthias Steinhauser. On the Higgs boson pair production at the LHC. *Nucl. Phys.*, B875:1–17, 2013.

[25] Nicola Cabibbo. Unitary symmetry and leptonic decays. *Phys. Rev. Lett.*, 10:531–533, Jun 1963.

[26] M. Kobayashi and T. Maskawa. CP-Violation in the Renormalizable Theory of Weak Interaction. *Progress of Theoretical Physics*, 49:652–657, February 1973.

[27] Ziro Maki, Masami Nakagawa, and Shoichi Sakata. Remarks on the unified model of elementary particles. *Progress of Theoretical Physics*, 28(5):870–880, 1962.

[28] Right. Hon. Lord Kelvin G.C.V.O. D.C.L. LL.D. F.R.S. M.R.I. I. nineteenth century clouds over the dynamical theory of heat and light. *The London, Edinburgh, and Dublin Philosophical Magazine and Journal of Science*, 2(7):1–40, 1901.

[29] H.E. Haber and G.L. Kane. The search for supersymmetry: Probing physics beyond the standard model. *Physics Reports*, 117(2):75 – 263, 1985.

[30] S. Dimopoulos, S. Raby, and Frank Wilczek. Supersymmetry and the scale of unification. *Phys. Rev. D*, 24:1681–1683, Sep 1981.

[31] L.E. Ibez and G.G. Ross. Low-energy predictions in supersymmetric grand unified theories. *Physics Letters B*, 105(6):439 – 442, 1981.

[32] Theodor Kaluza. Zum Unittsproblem der Physik. *Sitzungsber. Preuss. Akad. Wiss. Berlin (Math. Phys.)*, 1921:966–972, 1921.

[33] Finn Ravndal. Oskar Klein and the fifth dimension. 2013.

[34] Oliver Sim Brning, Paul Collier, P Lebrun, Stephen Myers, Ranko Ostojic, John Poole, and Paul Proudlock. *LHC Design Report*. CERN Yellow Reports: Monographs. CERN, Geneva, 2004.

[35] Oliver Sim Brning, Paul Collier, P Lebrun, Stephen Myers, Ranko Ostojic, John Poole, and Paul Proudlock. *LHC Design Report*. CERN Yellow Reports: Monographs. CERN, Geneva, 2004.

[36] Michael Benedikt, Paul Collier, V Mertens, John Poole, and Karlheinz Schindl. *LHC Design Report*. CERN Yellow Reports: Monographs. CERN, Geneva, 2004.

[37] K. Aamodt et al. The ALICE experiment at the CERN LHC. *JINST*, 3:S08002, 2008.

[38] A. Augusto Alves, Jr. et al. The LHCb Detector at the LHC. *JINST*, 3:S08005, 2008.

[39] ATLAS magnet system: Technical design report. 1997.

[40] *ATLAS inner detector: Technical Design Report, 1*. Technical Design Report ATLAS. CERN, Geneva, 1997.

[41] J N Jackson. The ATLAS semiconductor tracker (SCT). *Nucl. Instrum. Methods Phys. Res., A*, 541:89–95, 2005.

[42] The ATLAS TRT collaboration, E Abat, T N Addy, T P A kesson, J Alison, F Anghinolfi, E Arik, M Arik, G Atoian, B Auerbach, O K Baker, E Banas, S Baron, C Bault, N Becerici, A Beddall, A J Beddall, J Bendotti, D P

Benjamin, H Bertelsen, A Bingul, H Blampey, A Bocci, M Bochenek, V G Bondarenko, V Bychkov, J Callahan, M Capens Garrido, L Cardiel Sas, A Catinaccio, S A Cetin, T Chandler, R Chritin, P Cwetanski, M Dam, H Danielsson, E Danilevich, E David, J Degenhardt, B Di Girolamo, F Dittus, N Dixon, O B Dogan, B A Dolgoshein, N Dressnandt, C Driouchi, W L Ebenstein, P Eerola, U Egede, K Egorov, H Evans, P Farthouat, O L Fedin, A J Fowler, S Fratina, D Froidevaux, A Fry, P Gagnon, I L Gavrilenko, C Gay, N Ghodbane, J Godlewski, M Goulette, I Gousakov, N Grigalashvili, Y Grishkevich, J Grognuz, Z Hajduk, M Hance, F Hansen, J B Hansen, P H Hansen, G A Hare, A Harvey Jr, C Hauviller, A High, W Hulsbergen, W Huta, V Issakov, S Istin, V Jain, G Jarlskog, L Jeanty, V A Kantserov, B Kaplan, A S Kapliy, S Katounine, F Kayumov, P T Keener, G D Kekelidze, E Khabarova, A Khristachev, B Kisielewski, T H Kittelmann, C Kline, E B Klinkby, N V Klopov, B R Ko, T Koffas, N V Kondratieva, S P Konovalov, S Koperny, H Korsmo, S Kovalenko, T Z Kowalski, K Krger, V Kramarenko, L G Kudin, A-C Le Bihan, B C LeGeyt, K Levterov, P Lichard, A Lindahl, V Lisan, S Lobastov, A Loginov, C W Loh, S Lokwitz, M C Long, S Lucas, A Lucotte, F Luehring, B Lundberg, R Mackeprang, V P Maleev, A Manara, M Mandl, A J Martin, F F Martin, R Mashinistov, G M Mayers, K W McFarlane, V Mialkovski, B M Mills, B Mindur, V A Mitsou, J U Mjrnmark, S V Morozov, E Morris, S V Mouraviev, A M Muir, A Munar, A V Nadtochi, S Y Nesterov, F M Newcomer, N Nikitin, O Novgorodova, E G Novodvorski, H Ogren, S H Oh, S B Oleshko, D Olivito, J Olszowska, W Ostrowicz, M S Passmore, S Patrichev, J Penwell, F Perez-Gomez, V D Peshekhonov, T C Petersen, R Petti, A Placci, A Poblaguev, X Pons, M J Price, O R hne, R D Reece, M B Reilly, C Rembser, A Romaniouk, D Rousseau, D Rust, Y F Ryabov, V Ryjov, M Sderberg, A Savenkov, J Saxon, M Scandurra, V A Schegelsky, M I Scherzer, M P Schmidt, C Schmitt, E Sedykh, D M Seliverstov, T Shin, A Shmeleva, S Sivoklokov, S Yu Smirnov, L Smirnova, O Smirnova, P Smith, V V Sosnovtsev, G Sprachmann, S Subramania, S I Suchkov, V V Sulin, R R Szczygiel, G Tartarelli, E Thomson, V O Tikhomirov, P Tipton, J A Valls Ferrer, R Van Berg, V I Vassilakopoulos, L Vassilieva, P Wagner, R Wall, C Wang, D Whittington, H H Williams, A Zhelezko, and K Zhukov. The atlas transition radiation tracker (trt) proportional drift tube: design and performance. *Journal of Instrumentation*, 3(02):P02013, 2008.

[43] *ATLAS liquid-argon calorimeter: Technical Design Report*. Technical Design Report ATLAS. CERN, Geneva, 1996.

[44] ATLAS tile calorimeter: Technical design report. 1996.

[45] ATLAS liquid argon calorimeter: Technical design report. 1996.

[46] *ATLAS muon spectrometer: Technical Design Report*. Technical Design Report ATLAS. CERN, Geneva, 1997.

[47] *ATLAS level-1 trigger: Technical Design Report*. Technical Design Report ATLAS. CERN, Geneva, 1998.

[48] Peter Jenni, Marzio Nessi, Markus Nordberg, and Kenway Smith. *ATLAS high-level trigger, data-acquisition and controls: Technical Design Report*. Technical Design Report ATLAS. CERN, Geneva, 2003.

[49] ATLAS Collaboration. Technical Design Report for the ATLAS Inner Tracker Pixel Detector. Technical Report CERN-LHCC-2017-021. ATLAS-TDR-030, CERN, Geneva, Sep 2017.

[50] A. Airapetian et al. ATLAS calorimeter performance Technical Design Report. 1996.

[51] F. Bauer et al. Construction and Test of MDT Chambers for the ATLAS Muon Spectrometer. *Nucl. Instrum. Meth.*, A461:17–20, 2001.

[52] Theodoros Argyropoulos et al. Cathode strip chambers in ATLAS: Installation, commissioning and in situ performance. *IEEE Trans. Nucl. Sci.*, 56:1568–1574, 2009.

[53] Giordano Cattani and the RPC group. The resistive plate chambers of the atlas experiment: performance studies. *Journal of Physics: Conference Series*, 280(1):012001, 2011.

[54] Koichi Nagai. Thin gap chambers in atlas. *Nuclear Instruments and Methods in Physics Research Section A: Accelerators, Spectrometers, Detectors and Associated Equipment*, 384(1):219 – 221, 1996. BEAUTY '96.

[55] Stefan Maettig. *Luminosity Measurements with the ATLAS Detector*. PhD thesis, Hamburg U., 2012-06-28.

[56] The ATLAS TDAQ Collaboration. The atlas data acquisition and high level trigger system. *Journal of Instrumentation*, 11(06):P06008, 2016.

[57] A Barriuso Poy, H Boterenbrood, H J Burckhart, J Cook, V Filimonov, S Franz, O Gutzwiller, B Hallgren, V Khomutnikov, S Schlenker, and F Varela. The detector control system of the atlas experiment. *Journal of Instrumentation*, 3(05):P05006, 2008.

[58] Georges Aad et al. Electron reconstruction and identification efficiency measurements with the ATLAS detector using the 2011 LHC proton-proton collision data. *Eur. Phys. J.*, C74(7):2941, 2014.

[59] Georges Aad et al. Muon reconstruction performance of the ATLAS detector in protonproton collision data at $\sqrt{s}$ =13 TeV. *Eur. Phys. J.*, C76(5):292, 2016.

[60] Measurement of the tau lepton reconstruction and identification performance in the ATLAS experiment using pp collisions at $\sqrt{s} = 13$ TeV. Technical Report ATLAS-CONF-2017-029, CERN, Geneva, May 2017.

[61] Reconstruction, Energy Calibration, and Identification of Hadronically Decaying Tau Leptons in the ATLAS Experiment for Run-2 of the LHC. Technical Report ATL-PHYS-PUB-2015-045, CERN, Geneva, Nov 2015.

[62] Georges Aad et al. Identification and energy calibration of hadronically decaying tau leptons with the ATLAS experiment in pp collisions at $\sqrt{s}$=8 TeV. *Eur. Phys. J.*, C75(7):303, 2015.

[63] A. Elagin, P. Murat, A. Pranko, and A. Safonov. A New Mass Reconstruction Technique for Resonances Decaying to di-tau. *Nucl. Instrum. Meth.*, A654:481–489, 2011.

[64] M. Tanabashi, K. Hagiwara, K. Hikasa, K. Nakamura, Y. Sumino, F. Takahashi, J. Tanaka, K. Agashe, G. Aielli, C. Amsler, M. Antonelli, D. M. Asner, H. Baer, Sw. Banerjee, R. M. Barnett, T. Basaglia, C. W. Bauer, J. J. Beatty, V. I. Belousov, J. Beringer, S. Bethke, A. Bettini, H. Bichsel, O. Biebel, K. M. Black, E. Blucher, O. Buchmuller, V. Burkert, M. A. Bychkov, R. N. Cahn, M. Carena, A. Ceccucci, A. Cerri, D. Chakraborty, M.-C. Chen, R. S. Chivukula, G. Cowan, O. Dahl, G. D'Ambrosio, T. Damour, D. de Florian, A. de Gouvêa, T. DeGrand, P. de Jong, G. Dissertori, B. A. Dobrescu, M. D'Onofrio, M. Doser, M. Drees, H. K. Dreiner, D. A. Dwyer, P. Eerola, S. Eidelman, J. Ellis, J. Erler, V. V. Ezhela, W. Fetscher, B. D. Fields, R. Firestone, B. Foster, A. Freitas, H. Gallagher, L. Garren, H.-J. Gerber, G. Gerbier, T. Gershon, Y. Gershtein, T. Gherghetta, A. A. Godizov, M. Goodman, C. Grab, A. V. Gritsan, C. Grojean, D. E. Groom, M. Grünewald, A. Gurtu, T. Gutsche, H. E. Haber, C. Hanhart, S. Hashimoto, Y. Hayato, K. G. Hayes, A. Hebecker, S. Heinemeyer, B. Heltsley, J. J. Hernández-Rey, J. Hisano, A. Höcker, J. Holder, A. Holtkamp, T. Hyodo, K. D. Irwin, K. F. Johnson, M. Kado, M. Karliner, U. F. Katz, S. R. Klein, E. Klempt, R. V. Kowalewski, F. Krauss, M. Kreps, B. Krusche, Yu. V. Kuyanov, Y. Kwon, O. Lahav, J. Laiho, J. Lesgourgues, A. Liddle, Z. Ligeti, C.-J. Lin, C. Lippmann, T. M. Liss, L. Littenberg, K. S. Lugovsky, S. B. Lugovsky, A. Lusiani, Y. Makida, F. Maltoni, T. Mannel, A. V. Manohar, W. J. Marciano, A. D. Martin, A. Masoni, J. Matthews, U.-G. Meißner, D. Milstead, R. E. Mitchell, K. Mönig, P. Molaro, F. Moortgat, M. Moskovic, H. Murayama, M. Narain, P. Nason, S. Navas, M. Neubert, P. Nevski, Y. Nir, K. A. Olive, S. Pagan Griso, J. Parsons, C. Patrignani, J. A. Peacock, M. Pennington, S. T. Petcov, V. A. Petrov, E. Pianori, A. Piepke, A. Pomarol, A. Quadt, J. Rademacker, G. Raffelt, B. N. Ratcliff, P. Richardson, A. Ringwald, S. Roesler, S. Rolli, A. Romaniouk, L. J. Rosenberg, J. L. Rosner, G. Rybka, R. A. Ryutin, C. T. Sachrajda, Y. Sakai, G. P. Salam, S. Sarkar, F. Sauli, O. Schneider, K. Scholberg, A. J. Schwartz, D. Scott, V. Sharma, S. R. Sharpe, T. Shutt, M. Silari, T. Sjöstrand, P. Skands, T. Skwarnicki, J. G. Smith, G. F. Smoot, S. Spanier, H. Spieler, C. Spiering, A. Stahl, S. L. Stone, T. Sumiyoshi, M. J. Syphers, K. Terashi, J. Terning, U. Thoma, R. S. Thorne, L. Tiator, M. Titov, N. P. Tkachenko, N. A. Törnqvist, D. R. Tovey, G. Valencia, R. Van de Water, N. Varelas, G. Venanzoni, L. Verde, M. G. Vincter,

P. Vogel, A. Vogt, S. P. Wakely, W. Walkowiak, C. W. Walter, D. Wands, D. R. Ward, M. O. Wascko, G. Weiglein, D. H. Weinberg, E. J. Weinberg, M. White, L. R. Wiencke, S. Willocq, C. G. Wohl, J. Womersley, C. L. Woody, R. L. Workman, W.-M. Yao, G. P. Zeller, O. V. Zenin, R.-Y. Zhu, S.-L. Zhu, F. Zimmermann, P. A. Zyla, J. Anderson, L. Fuller, V. S. Lugovsky, and P. Schaffner. Review of particle physics. *Phys. Rev. D*, 98:030001, Aug 2018.

[65] Matteo Cacciari, Gavin P. Salam, and Gregory Soyez. The anti-k_t jet clustering algorithm. *JHEP*, 04:063, 2008.

[66] Tagging and suppression of pileup jets with the ATLAS detector. Technical Report ATLAS-CONF-2014-018, CERN, Geneva, May 2014.

[67] Georges Aad et al. Performance of b-Jet Identification in the ATLAS Experiment. *JINST*, 11(04):P04008, 2016.

[68] Optimisation of the ATLAS b-tagging performance for the 2016 LHC Run. Technical Report ATL-PHYS-PUB-2016-012, CERN, Geneva, Jun 2016.

[69] Tatsuya Masubuchi, David Olivier Jamin, and Jeffrey Wayne Hetherly. Object selections for the SM VH and $A \to Zh$ search
with V decaying leptonically and $h \to b\bar{b}$ with Run-2 data collected with the ATLAS detector at $\sqrt{s} = 13$ TeV
- Supporting Document -. Technical Report ATL-COM-PHYS-2015-1467, CERN, Geneva, Dec 2015.

[70] Expected performance of missing transverse momentum reconstruction for the ATLAS detector at $\sqrt{s} = 13$ TeV. Technical Report ATL-PHYS-PUB-2015-023, CERN, Geneva, Jul 2015.

[71] Yoav Freund and Robert E. Schapire. A short introduction to boosting. In *In Proceedings of the Sixteenth International Joint Conference on Artificial Intelligence*, pages 1401–1406. Morgan Kaufmann, 1999.

[72] N. Smirnov. Table for estimating the goodness of fit of empirical distributions. *Ann. Math. Statist.*, 19(2):279–281, 06 1948.

[73] P. J. Laycock, M. A. Chelstowska, T. C. Donszelmann, J. Guenther, A. Nairz, R. Nikolaidou, E. Shabalina, J. Strandberg, A. Taffard, and S. Wang. ATLAS data preparation in run 2. *J. Phys. Conf. Ser.*, 898(4):042050, 2017.

[74] G. Aad et al. The ATLAS Simulation Infrastructure. *Eur. Phys. J.*, C70:823–874, 2010.

[75] S. Agostinelli, J. Allison, K. Amako, J. Apostolakis, H. Araujo, P. Arce, M. Asai, D. Axen, S. Banerjee, G. Barrand, F. Behner, L. Bellagamba, J. Boudreau, L. Broglia, A. Brunengo, H. Burkhardt, S. Chauvie, J. Chuma, R. Chytracek,

G. Cooperman, G. Cosmo, P. Degtyarenko, A. Dell'Acqua, G. Depaola, D. Dietrich, R. Enami, A. Feliciello, C. Ferguson, H. Fesefeldt, G. Folger, F. Foppiano, A. Forti, S. Garelli, S. Giani, R. Giannitrapani, D. Gibin, J.J. Gmez Cadenas, I. Gonzlez, G. Gracia Abril, G. Greeniaus, W. Greiner, V. Grichine, A. Grossheim, S. Guatelli, P. Gumplinger, R. Hamatsu, K. Hashimoto, H. Hasui, A. Heikkinen, A. Howard, V. Ivanchenko, A. Johnson, F.W. Jones, J. Kallenbach, N. Kanaya, M. Kawabata, Y. Kawabata, M. Kawaguti, S. Kelner, P. Kent, A. Kimura, T. Kodama, R. Kokoulin, M. Kossov, H. Kurashige, E. Lamanna, T. Lampn, V. Lara, V. Lefebure, F. Lei, M. Liendl, W. Lockman, F. Longo, S. Magni, M. Maire, E. Medernach, K. Minamimoto, P. Mora de Freitas, Y. Morita, K. Murakami, M. Nagamatu, R. Nartallo, P. Nieminen, T. Nishimura, K. Ohtsubo, M. Okamura, S. O'Neale, Y. Oohata, K. Paech, J. Perl, A. Pfeiffer, M.G. Pia, F. Ranjard, A. Rybin, S. Sadilov, E. Di Salvo, G. Santin, T. Sasaki, N. Savvas, Y. Sawada, S. Scherer, S. Sei, V. Sirotenko, D. Smith, N. Starkov, H. Stoecker, J. Sulkimo, M. Takahata, S. Tanaka, E. Tcherniaev, E. Safai Tehrani, M. Tropeano, P. Truscott, H. Uno, L. Urban, P. Urban, M. Verderi, A. Walkden, W. Wander, H. Weber, J.P. Wellisch, T. Wenaus, D.C. Williams, D. Wright, T. Yamada, H. Yoshida, and D. Zschiesche. Geant4a simulation toolkit. *Nuclear Instruments and Methods in Physics Research Section A: Accelerators, Spectrometers, Detectors and Associated Equipment*, 506(3):250 – 303, 2003.

[76] Johan Alwall, Michel Herquet, Fabio Maltoni, Olivier Mattelaer, and Tim Stelzer. MadGraph 5 : Going Beyond. *JHEP*, 06:128, 2011.

[77] Torbjorn Sjostrand, Stephen Mrenna, and Peter Z. Skands. A Brief Introduction to PYTHIA 8.1. *Comput. Phys. Commun.*, 178:852–867, 2008.

[78] ATLAS Run 1 Pythia8 tunes. Technical Report ATL-PHYS-PUB-2014-021, CERN, Geneva, Nov 2014.

[79] R.D. Ball et al. Parton distributions with LHC data. *Nucl. Phys.*, B867:244–289, 2013.

[80] J. Alwall, R. Frederix, S. Frixione, V. Hirschi, F. Maltoni, O. Mattelaer, H. S. Shao, T. Stelzer, P. Torrielli, and M. Zaro. The automated computation of tree-level and next-to-leading order differential cross sections, and their matching to parton shower simulations. *JHEP*, 07:079, 2014.

[81] M. Bahr et al. Herwig++ Physics and Manual. *Eur. Phys. J.*, C58:639–707, 2008.

[82] S. Borowka, N. Greiner, G. Heinrich, S. P. Jones, M. Kerner, J. Schlenk, and T. Zirke. Full top quark mass dependence in Higgs boson pair production at NLO. *JHEP*, 10:107, 2016.

[83] Simone Alioli, Paolo Nason, Carlo Oleari, and Emanuele Re. A general framework for implementing NLO calculations in shower Monte Carlo programs: the POWHEG BOX. *JHEP*, 06:043, 2010.

[84] Torbjorn Sjostrand, Stephen Mrenna, and Peter Z. Skands. PYTHIA 6.4 Physics and Manual. *JHEP*, 05:026, 2006.

[85] Peter Zeiler Skands. Tuning Monte Carlo Generators: The Perugia Tunes. *Phys. Rev.*, D82:074018, 2010.

[86] David J. Lange. The evtgen particle decay simulation package. *Nuclear Instruments and Methods in Physics Research Section A: Accelerators, Spectrometers, Detectors and Associated Equipment*, 462(1):152 – 155, 2001. BEAUTY2000, Proceedings of the 7th Int. Conf. on B-Physics at Hadron Machines.

[87] Michal Czakon, Michelangelo L. Mangano, Alexander Mitov, and Juan Rojo. Constraints on the gluon PDF from top quark pair production at hadron colliders. *JHEP*, 07:167, 2013.

[88] T. Gleisberg, Stefan. Hoeche, F. Krauss, M. Schonherr, S. Schumann, F. Siegert, and J. Winter. Event generation with SHERPA 1.1. *JHEP*, 02:007, 2009.

[89] Tanju Gleisberg and Stefan Hoeche. Comix, a new matrix element generator. *JHEP*, 12:039, 2008.

[90] Fabio Cascioli, Philipp Maierhofer, and Stefano Pozzorini. Scattering Amplitudes with Open Loops. *Phys. Rev. Lett.*, 108:111601, 2012.

[91] Steffen Schumann and Frank Krauss. A Parton shower algorithm based on Catani-Seymour dipole factorisation. *JHEP*, 03:038, 2008.

[92] Stefan Hoeche, Frank Krauss, Marek Schonherr, and Frank Siegert. QCD matrix elements + parton showers: The NLO case. *JHEP*, 04:027, 2013.

[93] Simone Alioli, Paolo Nason, Carlo Oleari, and Emanuele Re. NLO Higgs boson production via gluon fusion matched with shower in POWHEG. *JHEP*, 04:002, 2009.

[94] Georges Aad et al. Measurement of the Z/γ^* boson transverse momentum distribution in pp collisions at $\sqrt{s} = 7$ TeV with the ATLAS detector. *JHEP*, 09:145, 2014.

[95] Damian Alvarez Piqueras, Matthew Beckingham, Will Davey, Eric Drechsler, Dirk Duschinger, Luca Fiorini, Anna Goussiou, Carl Gwilliam, Guillermo Nicolas Hamity, Lorenz Hauswald, Rachel Hyneman, Samina Jabbar, and K. Technical report.

[96] Morad Aaboud et al. Luminosity determination in pp collisions at $\sqrt{s} = 8$ TeV using the ATLAS detector at the LHC. *Eur. Phys. J.*, C76(12):653, 2016.

[97] J. Alwall et al. The automated computation of tree-level and next-to-leading order differential cross sections, and their matching to parton shower simulations. *JHEP*, 07:079, 2014.

[98] T Sjostrand et al. An introduction to pythia 8.2. *Comput.Phys.Commun.*, 191:159–177, 2015.

[99] D. J. Lange. The EvtGen particle decay simulation package. *Nucl. Instrum. Meth.*, A462:152, 2001.

[100] Spyridon Argyropoulos, Hannah Arnold, Andrew Stuart Bell, Jose Benitez, Adrian Buzatu, Valerio Dao, David Delgove, Yuji Enari, Wade Cameron Fisher, Kristian Gregersen, Jean-Francois Grivaz, Jun Guo, Garabed Halladjian, Gavin Grant Hesketh, Jeffrey Wayne Hetherly, Andreas Honle, Ruth Magdalena Jacobs, Benjamin Paul Jaeger, Stephen Jiggins, Chikuma Kato, Nataliia Kondrashova, Sandra Kortner, Tatjana Lenz, Usha Mallik, Tatsuya Masubuchi, Josh Mcfayden, Andrew Mehta, Alyssa Montalbano, Nicolas Morange, Felix Mueller, Forrest Hays Phillips, Christopher Samuel Pollard, Arturo Sanchez, Tim Scanlon, Stephen Sekula, Paul Thompson, Dmitri Tsybychev, Christian Weiser, and Haijun Yang. Search for resonances decaying to a W or Z boson and a Higgs boson in the $\nu\nu bb$, $\ell\nu bb$ and $\ell\ell bb$ final states with $\sqrt{s} = 13$ TeV ATLAS data in the context of models with 2 Higgs doublets or additional heavy vector triplets. Technical Report ATL-COM-PHYS-2016-479, CERN, Geneva, May 2016.

[101] S. Borowka, N. Greiner, G. Heinrich, S.P. Jones, M. Kerner, J. Schlenk, U. Schubert, and T. Zirke. Higgs Boson Pair Production in Gluon Fusion at Next-to-Leading Order with Full Top-Quark Mass Dependence. *Phys. Rev. Lett.*, 117(1):012001, 2016. [Erratum: Phys. Rev. Lett.117,no.7,079901(2016)].

[102] D de Florian et al. Handbook of LHC Higgs Cross Sections: 4. Deciphering the Nature of the Higgs Sector. 2016.

[103] Kyle Cranmer. Practical Statistics for the LHC. In *Proceedings, 2011 European School of High-Energy Physics (ESHEP 2011): Cheile Gradistei, Romania, September 7-20, 2011*, pages 267–308, 2015. [,247(2015)].

[104] Glen Cowan, Kyle Cranmer, Eilam Gross, and Ofer Vitells. Asymptotic formulae for likelihood-based tests of new physics. *Eur. Phys. J.*, C71:1554, 2011. [Erratum: Eur. Phys. J.C73,2501(2013)].

[105] J. S. Conway. Incorporating Nuisance Parameters in Likelihoods for Multisource Spectra. In *Proceedings, PHYSTAT 2011 Workshop on Statistical Issues Related to Discovery Claims in Search Experiments and Unfolding, CERN,Geneva, Switzerland 17-20 January 2011*, pages 115–120, 2011.

[106] A L Read. Presentation of search results: the cl s technique. *Journal of Physics G: Nuclear and Particle Physics*, 28(10):2693, 2002.

[107] A. Djouadi, L. Maiani, G. Moreau, A. Polosa, J. Quevillon, and V. Riquer. The post-Higgs MSSM scenario: Habemus MSSM? *Eur. Phys. J.*, C73:2650, 2013.

[108] T. V. Obikhod and E. A. Petrenko. The study of the properties of the extended Higgs boson sector within hMSSM model. 2017.

[109] Jihn E. Kim. Light pseudoscalars, particle physics and cosmology. *Physics Reports*, 150(1):1 – 177, 1987.

[110] G. Duckeck, D. Barberis, R. Hawkings, R. Jones, N. McCubbin, G. Poulard, D. Quarrie, T. Wenaus, and E. Obreshkov. ATLAS computing: Technical design report. 2005.

[111] Savas Dimopoulos and Howard Georgi. Softly broken supersymmetry and su(5). *Nuclear Physics B*, 193(1):150 – 162, 1981.